POLITECNICO DI TORINO

Collegio di Ingegneria Chimica e dei Materiali

Master of Science Course in Ingegneria Chimica e dei Processi Sostenibili

Master of Science Thesis

Photo-thermal catalytic CO_2 conversion to CO

Tutors
prof.ssa Stefania Specchia
doc. dr. Petar Djinovic

Candidate
Giovanni Cardolini Rizzo

Marzo 2024

Sommario

L'attuale sistema socio-economico globale è strettamente legato all'utilizzo dei combustibili fossili. Essi hanno negli anni svolto sia la funzione di fonti energetiche primarie che di materie prime per una vasta gamma di prodotti chimici lavorati quali benzina, diesel, sostanze petrolchimiche e chimiche, materiali sintetici, plastiche e prodotti farmaceutici. Nel corso dei secoli sono stati diversi i combustibili fossili che si sono susseguiti e hanno contribuito all'avanzamento industriale. A partire dalla fine del XIX secolo tale ruolo è stato svolto da petrolio e gas naturale. Nonostante le riserve mondiali non siano diminuite significativamente negli ultimi 50 anni, soprattutto grazie ai continui progressi nelle tecnologie di esplorazione e produzione, attualmente si stima che le riserve di petrolio durerebbero circa 40 anni al tasso di consumo attuale. Infatti, l'espansione continua della popolazione globale e i notevoli miglioramenti negli standard di vita umani hanno portato a un notevole aumento del consumo energetico negli ultimi decenni. A tale effetto si vanno ad aggiungere gli ingenti danni ambientali dovuti alla costante introduzione nell'ambiente di inquinanti quali ossidi di azoto, ozono, metano e anidride carbonica. L'impatto di tali emissioni rappresenta una minaccia significativa per l'equilibrio ecologico del pianeta e un'ulteriore motivazione alla ricerca di alternative energetiche sostenibili. In questo senso assumono importanza l'energia idroelettrica e geotermica, ma data la limitata possibilità di impiego, fondamentalmente legata alla collocazione geografica e ambientale, risulta improbabile che vadano a sostituire i combustibili fossili. L'energia nucleare trova costantemente contro l'opposizione pubblica e le preoccupazioni per la sicurezza, nonostante rimanga una via percorribile nel lungo termine. Negli ultimi anni l'idrogeno è stato proposto come una promettente fonte di energia pulita, ma manca di un efficiente sistema di raccolta e distribuzione, rendendo la sua adozione su larga scala proibitiva dal punto di vista economico. L'impiego di risorse energetiche alternative risulta essenziale ma non basta a sostituire completamente le risorse energetiche tradizionali, che continuano ad essere imprescindibili nei settori del trasporto e dell'energia. In questo senso un controllo delle emissioni di CO_2 appare necessario. La strategia più promettente nell'ambito della CCU (Carbon Capture and Utilization) riguarda l'utilizzo della CO_2 come fonte di carbonio per la successiva sintesi di chemicals e combustibili. Data però la grande stabilità della CO_2, caratterizzata dal doppio legame C=O ad alta energia (750 kJ/mol), la sua idrogenazione richiede un input energetico considerevole. La sintesi di combustibili a partire da CO_2, denominata "reduction route", porta alla diminuzione del numero di ossidazione dell'atomo di carbonio, portando alla produzione di metano, monossido di carbonio, metanolo, etanolo, acido formico e altri idrocarburi, che rientrano nella definizione di "solar fuels". Essi possono poi essere impiegati come carburanti o all'interno delle fuel cell, portando al rilascio di CO_2. Tutto ciò rientra nel concetto della "methanol economy", un'economia circolare per l'utilizzo dei solar fuels, dove idrogeno e carbonio sono impiegati in maniera ciclica, eliminando la necessità di un inlet di atomi di C ad opera dei combustibili fossili. Un grande vantaggio sta nella possibilità di usare le stesse infrastrutture per la produzione e il trasporto di energia impiegati attualmente. Inoltre, rispetto alle fonti rinnovabili, che offrono energia in maniera intermittente, non costante, la grande densità energetica accumulata nei legami C-H costituisce un ulteriore vantaggio. Inoltre gli stessi composti possono essere impiegati come building blocks per la sintesi chimica di composti più complessi. Tale prospettiva porta alla trasformazione della CO_2 da rifiuto indesiderato, dannoso per il pianeta, ad una fonte di carbonio capace di rimpiazzare i combustibili fossili in varie applicazioni. Ciò porta ad un duplice vantaggio, la riduzione dell'impatto ambientale associato alle emissioni di CO_2 e una via per mitigare il progressivo esaurimento delle risorse naturali. La trattazione che segue è organizzata nel modo seguente, una prima parte è dedicata allo stato dell'arte della "Photo-thermal catalysis", seguono i capitoli dedicati alla reazione di RWGS studiata, compresa di meccanismo di reazione, e al catalizzatore CZA che si è scelto di impiegare. I capitoli successivi trattano la parte puramente sperimentale, a sua volta divisa in tre macro-capitoli: (1) la caratterizzazione chimico-fisica del catalizzatore, con le tecniche XRD, SEM e il fisisorbimento di azoto, (2) la pianificazione e l'attuazione dei test di attività e degli esperimenti relativi all'investigazione del meccanismo di reazione, (3) l'analisi spettroscopica, con le tecniche UV-vis e IR. Ognuno di essi comprende delle parti introduttive teoriche relative alla tecnica sperimentale, la descrizione della procedura impiegata e dei risultati ottenuti con annessa discussione e commento. L'ultimo capitolo tratta le conclusioni.

Tra le tecnologie più promettenti e innovative per tale utilizzo della CO_2 si colloca la "photo-termal catalytic reduction" della CO_2, la quale sfrutta la parziale sostituzione di energia termica con energia luminosa per far avvenire la reazione di Reverse Water Gas Shift (RWGS) in ambiente catalitico a basse

pressione e temperatura, fino alla produzione di monossido di carbonio. Le reazioni catalitiche che prevedono l'accoppiamento di energia solare e termica posso essere divise in tre categorie: "photo-thermochemical cycle", in cui la fotocatalisi e la catalisi termica avvengono separatamente e indipendentemente; "photo-driven thermal catalysis" in cui il catalizzatore assorbe l'energia solare che viene convertita in energia termica, senza andare a modificare il meccanismo della reazione termocatalitica; "photo-thermo catalysis" in cui l'energia solare e termica contribuiscono sinergicamente all'avanzamento della reazione, portando ad un incremento dell'attività e/o della selettività. Tale meccanismo è quello che porta al più efficiente ed integrato utilizzo della luce nel sistema, permettendo un aumento della velocità di reazione a basse temperature, con l'ulteriore vantaggio di limitare effetti indesiderati quali la perdita di selettività o la degradazione chimica e catalitica.

I semiconduttori rappresentano materiali di grande interesse per le applicazioni che prevedono lo sfruttamento della luce grazie ai valori di band gap, che si allinea con il range di energia della luce visibile. Nei semiconduttori, la banda di valenza (VB) contiene stati occupati da elettroni nello stato fondamentale, mentre la banda di conduzione (CB) è costituita da stati non occupati a T = 0 K. A temperature più elevate, alcuni elettroni vengono eccitati termicamente nella CB e la distribuzione della densità elettronica risultante è caratterizzata dal livello di Fermi del semiconduttore. L'assorbimento di un fotone di energia maggiore o uguale al band gap, porta un elettrone ad essere eccitato dalla VB alla CB, creando una lacuna (h) nella VB. L'illuminazione di un semiconduttore porta ad una quantità maggiore di tali complessi elettrone-buca rispetto all'equilibrio. I carrier così generati possono migrare verso la superficie del fotocatalizzatore e trasferirsi alle molecole accettori adsorbite, avviando processi di riduzione o ossidazione. I siti di reazione effettivi possono trovarsi sulla superficie del semiconduttore oppure all'interfaccia con la superficie di un altro semiconduttore o nanoparticella metallica, spesso indicata come co-catalizzatore. Nella fotocatalisi, il ruolo primario del semiconduttore è quello di assorbire i fotoni incidenti, generare i complessi elettrone-buca e facilitare la loro separazione e trasporto. La catalisi della reazione è tipicamente eseguita da un materiale diverso.

Quando le nanoparticelle metalliche sono supportate sul semiconduttore, gli elettroni fotogenerati vengono trasferiti sulla superficie del metallo, dato che il suo livello di Fermi giace energeticamente al di sotto della CB del semiconduttore. In questo modo che gli elettroni possono essere trasferiti all'adsorbato più facilmente rispetto al solo semiconduttore, ossia il catalizzatore risulta più riducente. Ciò porta alla formazione di una barriera di Schottky all'interfaccia dei due materiali e ad un incremento della separazione dei fotoelettroni, che si accumulano nel metallo, dalle fotovacanze, che invece restano nella banda di valenza del semiconduttore. Come risultato si ha un miglioramento della separazione delle cariche, velocità di ricombinazione più basse e un incremento dell'efficienza del processo.

Le nanoparticelle metalliche, dato l'elevato rapporto superficie/volume, sono molto efficaci nel ridurre le velocità di ricombinazione dei carrier, vista anche la breve distanza che gli elettroni devono percorrere nel raggiungere la superficie. L'ampia superficie reattiva invece aumenta l'interazione con le molecole adsorbite e quindi l'efficacia della fotocatalisi.

L'effetto LSPR (Localized Surface Plasmon Resonance) osservato nelle nanoparticelle metalliche, è stato negli anni spiegato tramite il modello di Drude-Maxwell e le teorie formulate da Gustav Mie nel 1908. All'interno delle nanoparticelle metalliche, gli elettroni di conduzione sono liberi di muoversi quando influenzati da una radiazione incidente esterna. In condizioni di risonanza, la radiazione elettromagnetica incidente è in fase con la frequenza di risonanza degli elettroni di conduzione. In questo modo si va a massimizzare il campo elettrico causando la formazione di "hot-spot" sulla superficie delle nanoparticelle. All'aumento del campo elettrico si accompagno altre proprietà dei materiali plasmonici, prevalentemente dovute a fenomeni di ri-emissione delle radiazioni. L'energia accumulata può infatti decadere in forma radiativo, riemettendo fotoni ad energia inferiore per via delle erdite, oppure in forma non radiativa. A quest'ultima categoria appartengono il cosiddetto "Landau damping", responsabile della creazione di un complesso elettrone-buca, e le collisioni tra elettroni. Queste causano un effetto termico, trasferendo energia cinetica al reticolo cristallino del metallo (plasmon-induced heating effect). Nell'ambito della foto-termo catalisi, l'aumento delle prestazioni catalitiche in materiali plasmonici, e quindi della velocità di reazione, è dovuto al contributo contemporaneo dei due effetti: la creazione del complesso elettrone-buca (effetto fotochimico)e il riscaldamento localizzato (effetto termico). L'interazione tra nanopartielle plasmoniche allo stato eccitato e le specie chimiche adsorbite sulla superficie, può portare al trasferimento di uno o più elettroni negli orbitali di antilegame, formando specie ridotte. L'attivazione chimica dei composti adsorbiti è quindi causata da transizioni elettroniche o vibrazion-

ali, promuove il trasferimento di elettroni e può potenzialmente portare alla rottura di legami chimici e alla successiva trasformazione chimica.

Il trasferimento di elettroni alla molecola adsorbita applicato alla riduzione fotocatalitica del'anidride carbonica, causa una serie di reazioni chimiche in cascata. Tale processo multi-step coinvolge l'impiego di un massimo di otto elettroni e protoni, la rottura del legame C=O e la formazione di legami C-H, fino alla potenziale produzione di una serie di prodotti. La molecola di CO2 è fortemente stabile stabile e chimicamente inerte, ciò ha causa della geometria lineare, della configurazione elettronica a guscio chiuso e della simmetria D_{∞}h. Il trasferimento di un elettrone induce un bending nella struttura molecolare a causa della repulsione tra l'elettrone appena trasferito all'atomo di carbonio elettrofilo e i doppietti elettronici liberi sugli atomi di ossigeno. La riduzione della CO_2 ad opera di un singolo elettrone per andare a formare il radicale $CO^{\bullet -}$ è caratterizzata da un potenziale elettrochimico fortemente negativo (-1.9V). Nessun semiconduttore sarebbe capace di fornire abbastanza potenziale da trasferire un singolo fotoelettrone ad una molecola di CO_2. La fattibilità della riduzione fotocatalitica prevede un processo di trasferimento multi-elettronico (da 2 a 8) assistito dal trasferimento di altrettanti protoni:

$$CO_2 + 2\,H^+ + 2\,e^- \rightleftharpoons HCOOH \qquad E^0_{\text{redox}} = -0.61\text{V}$$

$$CO_2 + 2\,H^+ + 2\,e^- \rightleftharpoons CO + H_2O \qquad E^0_{\text{redox}} = -0.53\text{V}$$

$$CO_2 + 4\,H^+ + 4\,e^- \rightleftharpoons HCHO + H_2O \qquad E^0_{\text{redox}} = -0.48\text{V}$$

$$CO_2 + 6\,H^+ + 6\,e^- \rightleftharpoons CH_3OH + H_2O \qquad E^0_{\text{redox}} = -0.38\text{V}$$

$$CO_2 + 8\,H^+ + 8\,e^- \rightleftharpoons CH_4 + H_2O \qquad E^0_{\text{redox}} = -0.24\text{V}$$

In questo modo i potenziali di riduzione risultano a potenziale maggiore della banda di conduzione della maggior parte dei semiconduttori: Comunque il trasferimento del primo elettrone rimane l'ostacolo maggiore alla fotoriduzione della CO_2. La CO_2 adsorbita con formazione della specie a carica parziale ${CO_2}^{\delta\bullet -}$, presenta una simmetria minore e il LUMO a trovarsi a energie inferiori. Successivamente il processo di riduzione segue una serie di step elementari, ognuno dei quali coinvolge il trasferimento di un elettrone, un protone, insieme alla rottura di uno o più legami C-O e alla formazione di nuovi legami C-H. Numerosi intermedi di reazione si fanno a generare nel corso di questi step come specie radicaliche. Le nanoparticelle metalliche impiegate come co-catalizzatori, risultano fondamentali nel miglioramento della separazione delle cariche e nel catalizzare gli step successivi.

L'equazione di Reverse Water Gas Shift (RWGS) rappresenta l'idrogenazione reversibile di CO_2 con formazione di CO e H_2O:

$$CO_2 + H_2 \rightleftharpoons CO + H_2O \qquad \Delta H_{298K} = +42.1\,\text{kJ mol}^{-1}$$

La reazione risulta endotermica data la grande stabilità della molecola di CO_2. Per questo motivo, in accordo col principio di Le Chatelier, essa risulta favorita alle alte temperature. A pressione atmosferica la reazione è completamente spostata verso i prodotti a temperature superiori a 700°C. L'abbassamento della temperatura di reazione è una prerogativa fondamentale per andare a minimizzare le perdite energetiche e i costi capitali, data anche la necessità che ne deriverebbe di utilizzare apparecchiature compatibili con tali condizioni di reazione spinte. Ciò vale a maggior ragione se si considera la reazione di RWGS come il passaggio preliminare per la sintesi di combustibili sintetici a partire da CO tramite la reazione di Fisher-Tropsch (FT), operante nel range di temperature 200–375 °C. Il miglioramento delle performance catalitiche per la reazione di RWGS risulta quindi cruciale per soddisfare i requisiti del processo FT.

L'accoppiamento di semiconduttore e nanoparticelle metalliche porta ad un netto miglioramento dell'efficienza del sistema fotocatalitico: migliora la separazione del complesso elettrone-buca, facilita l'attivazione della CO_2

e presenta siti attivi per la reazione di riduzione. Il catalizzatore $Cu/ZnO/Al_2O_3$ è ampiamente impiegato in ambito industriale per la produzione di metanolo. La presenza tra i suoi componenti di materiali semiconduttori quali ZnO, Cu_2O, CuO e del metallo plasmonico Cu, suggerisce che le performance catalitiche possano essere incrementate dall'attivazione sinergica di calore e luce. Nel corso di questo lavoro, tale catalizzatore è stato impiegato per la produzione di CO con composizione: Cu 50%, ZnO 30%, and Al_2O_3 20%. L'ossido di zinco presenta un band gap diretto e pari a 3.37 eV e un raggio di Bohr di circa 2.34 nm. Questo può promuovere il chemisorbimento della CO_2 e migliorare l'interazione elettronica con il rame. L'allumina aumenta l'area superficiale delle nanoparticelle di Cu/ZnO, agendo da substrato per la loro crescita e dispersione nel catalizzatore. I benefici del catalizzatore CZA derivano dalla stabilizzazione degli intermedi di reazione promossa dal ZnO sul sistema Cu/ZnO, dalla "strong metal support interaction" (SMSI) tra Cu e ZnO che incrementa la formazione di siti attivi sulla superficie del catalizzatore. L'ossido di zinco agisce direttamente da modificatore strutturale, riserva di atomi di idrogeno e promotore dell'attivazione della CO_2. L'efficacia di tale composto risiede nell'effetto sinergico dovuto alla foto-attivazione diversificata dei due componenti principali. La banda di assorbimento della luce dell'ossido di zinco, situata a circa 390 nm, e l'effetto LSPR del rame, a circa 590 nm, alterano la quantità di elettroni eccitati sulla superficie del catalizzatore, regolando gli intermedi di reazione e i prodotti. L'effetto del band gap di Cu_2O e Cu è trascurabile data la loro presenza limitata dopo la riduzione. Inoltre la foto-eccitazione simultanea di Cu e ZnO può portare l'energia associata all'assorbimento dei fotoni a essere intrappolata nelle nanoparticelle di rame, portando ad un riscaldamento localizzato che va a contribuire alla reazione di idrogenazione. Uno degli svantaggi di tale catalizzatore è la disattivazione che può subire a causa della produzione di acqua. Essa causa l'agglomerazione del ZnO, causando una diminuzione della superficie all'interfaccia tra Cu e ZnO.

Il meccanismo di reazione e l'interazione tra i siti attivi del catalizzatore e i gas sono tuttora argomento di dibattito e di ricerca. Anche l'effetto della cosiddetta "Cu-ZnO sinergy" non è stato pienamente chiarito, e viene considerato sia solo un promotore strutturale, che un sito attivo essenziale. Sono due i meccanismi di reazione che sono stati proposti per tale reazione catalizzata: un meccanismo redox e un meccanismo di decomposizione del formato.

Il primo prevede l'adsorbimento di ossigeno sulla superficie del catalizzatore (è anche detto meccanismo dell'ossigeno adsorbito) e considera la reazione di RWGS come una serie di reazioni di cui il primo step è la decomposizione di CO_2 sulla superficie delle nanoparticelle di rame:

$$CO_2 \rightleftharpoons CO^* + O^*$$

$$CO^* \rightleftharpoons CO$$

$$H_2 \rightleftharpoons 2\,H^*$$

$$H^* + O^* \rightleftharpoons OH^*$$

$$H^* + OH^* \longrightarrow H_2O^*$$

$$H_2O^* \rightleftharpoons H_2O$$

L'interazione con l'idrogeno in fase gas porta successivamente al desorbimento del monossido di carbonio e degli atomi di ossigeno adsorbiti. La produzione di CO sulla superficie del catalizzatore è quindi dovuta solo all'esposizione del rame al flusso di CO_2. Lo stato di ossidazione del Cu è influenzato dalla popolazione superficiale delle specie O* e H*, che risultano rispettivamente dalla rottura del legame C-O della CO_2 adsorbita e del legame H-H. La riduzione degli atomi di ossigeno adsorbiti O* avviene molto più velocemente dell'ossidazione del catalizzatore ad opera della CO_2 (RDS), e l'idrogeno è il responsabile della riduzione del catalizzatore, ma senza la formazione di intermedi di reazione.

Il meccanismo di reazione appena descritto non è però in grado di descrivere pienamente l'andamento della reazione di RWGS. Infatti la dissociazione della molecola di CO_2 sulla superficie delle nanoparticelle di rame porta alla produzione diretta di CO, ma non è l'unico modo per ottenere monossido di carbonio. La formazione di CO è direttamente dipendente dalla presenza di idrogeno, il cui ruolo è legato all'adsorbimento di CO_2 per la formazione degli intermedi di reazione. Recenti risultati hanno mostrato come la superficie dell'ossido di zinco mostri la presenza di vacanze di ossigeno, e rappresenta un sito attivo per il chemisorbimento della CO_2

e la formazione di carbonato (CO_3*), bicarbonato (HCO_3*) e formato (HCOO*). Il rame contribuisce a ciò attraverso la scissione del legame H-H, aumentando la presenza di H* superficiali, e attraverso la promozione strutturale data dall'effetto sinergico dell'interfaccia Cu-ZnO. La produzione di CO può avvenire sia sulla superficie di Cu che sulla superficie di ZnO. Gli intermedi di reazione vengono poi decomposti con formazione di CO* e OH*, che vengono successivamente desorbiti portando alla produzione di CO e H_2O. Il formato è l'intermedio di reazione comunemente ritenuto dominante nel meccanismo di decomposizione.

Quando la superficie del catalizzatore viene irradiata da luce visibile, l'alterazione dello stato di ossidazione del rame, la mobilità dell'ossigeno nell'ossido di zinco, l'attivazione e la successiva idrogenazione della CO_2 sono in gran parte dovute alla promozione e al trasferimento di elettroni. L'eccitazione dell'ossido di zinco promuove il trasferimento di elettroni verso le nanoparticelle di rame, aumentando la presenza di specie Cu(I)-O superficiali, e quindi la produzione di CO. Gli elettroni generati dall'effetto LSPR del rame si ritiene siano invece la causa dell'attivazione e della scissione delle molecole H_2, portando alla riduzione dei siti Cu(I)-O e alla formazione di vacanze di ossigeno nell'ossido di zinco. L'eccitazione simultanea di entrambi i componenti porta al contemporaneo trasferimento di elettroni dal rame alla banda di conduzione del ZnO ("plasmon mediated electron transfer") e da ZnO a Cu ("photocatalyst-cocatalyst scheme"). Tali processi aumentano l'efficienza del processo fotocatalitico, aumentando di conseguenza la produzione di CO.

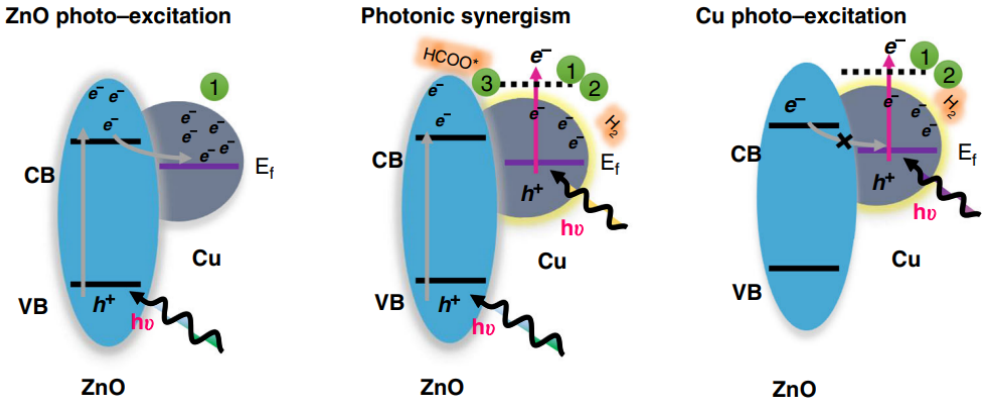

Figura I: Trasferimento di elettroni tra ZnO e Cu [1].

La prima fase della parte sperimentale ha riguardato la caratterizzazione chimico-fisica del catalizzatore impiegato, attraverso le tecniche SEM, XRD e il fisisorbimento di azoto. Tramite la microscopia SEM sono state ottenute delle immagini raffiguranti la morfologia generale del catalizzatore. La diffrattometria a raggi X è stata impiegata per confermare l'esatta struttura cristallina del catalizzatore durante la reazione. I composti $CuSiO_2$ e $CuZnOAl_2O_3$ sono stati analizzati prima e dopo essere sottoposti ad un processo di riduzione. Esso è stato effettuato inserendo 30 mg di composto all'interno di un reattore PFR e sottoponendoli ad un flusso di H_2/N_2 al 5% per 30 minuti con una velocità di riscaldamento pari a 10°C/min. I diffrattogrammi risultanti hanno rilevato la presenza di CuO, ZnO e Cu metallico. Al contrario Al_2O_3, data la sua natura amorfa, non presenta picchi di diffrazione. La presenza di Cu_2O è difficile da determinare data la sovrapposizione con i picchi di ZnO. Prima della fase di riduzione, entrambi i campioni hanno mostrato i picchi relativi a CuO a 35.6° e 38.7°. In più il CZA ha presentato i picchi relativi al ZnO a 31.9° e 36.9°, e un picco più intenso a 26.5°, corrispondente alla grafite, usata come legante nel catalizzatore. Dopo la fase di riduzione, è stata chiaramente visibile la scomparsa dei picchi relativi al CuO e la presenza a 43.2°, 50.3° e 73.9°, dei picchi relativi al rame metallico. Per tale motivo è stato possibile appurare che le condizioni di pre-riduzione erano sufficienti a ridurre completamente gli ossidi di rame a rame metallico. Inoltre i diffrattogrammi sono stati impiegati per andare a stimare la dimensione dei cristalliti dei vari componenti del catalizzatore tramite l'equazione di Scherrer.

Il fisisorbimento di azoto è stato impiegato per l'analisi porosimetrica del catalizzatore CZA, tramite l'apparecchiatura Micrometric TriStar II 3020. Due trattamenti preliminari sono stati effettuati precedentemente all'analisi per rimuovere le impurità. Il primo a 90°C per 60 minuti con una velocità di riscaldamento

Sample	BET surface area (m^2g^{-1})	BJH pore size (nm)	BJH pore volume (cm^3g^{-1})
CZA	67	15.2	0.26

Tabella I: Risulati delle analisi BET e BJH relative al catalizzatore CZA.

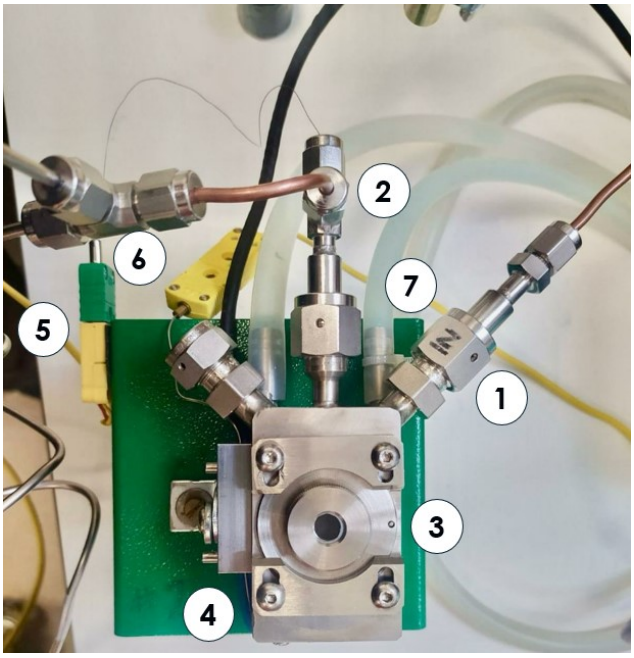

Figura II: Reattore Harrick Scientific reactor impiegato per i test catalitici: (1) gas inlet; (2) gas outlet; (3) calotta Raman dome in silice fusa sintetica (HVC-MRA); (4) elemento riscaldante a cartuccia; (5) termocoppia; (6) termocoppia nel campione lungo l'uscita del gas; (7) sistema di raffreddamento.

pari a 5°C/min, il secondo a 300°C per 24 minuti con una velocità di riscaldamento pari a 10°C/min. L'isoterma di adsorbimento/desorbimento risultante corrisponde all'isoterma di classe IV(a) secondo la categorizzazione IUPAC, caratteristica dei materiali mesoporosi. In questo caso particolare il plateau corrispondente al raggiungimento delle condizioni di saturazione risulta collassato ad un punto di inflessione. Risulta chiaramente osservabile il ciclo di isteresi associato alla condensazione capillare, corrispondente alla tipologia H1, con il caratteristico ciclo stretto e ripido nell'intervallo di pressioni relative 0.5-1. Esso è solitamente associato a materiali costituiti da mesopori stretti e uniformi. I metodi BET e BJH sono stati impiegati per determinare l'area superficiale e dimensione e volume dei pori, rispettivamente. I risultati sono riportati nella tabella sottostante:

Nell'ambito del lavoro di tesi, l'attività del catalizzatore CZA riguardo la reazione di RWGS è stata testata impiegando un reattore "Harrick Scientific" (HVC-MRA-5), un reattore a letto fisso a cui venivano mandate le correnti dei reagenti CO_2, H_2 ed N2, come rappresentato nelle figure sottostanti: I controllori di portata Brooks 5850 E regolano l'ingresso delle correnti dei reagenti. Il catalizzatore viene inserito nell'apposito contenitore all'interno del reattore. SiC, un composto che non presenta alcuna attività catalitica, è posizionato sul fondo del reattore, lasciando 1-2 mm in cima per l'inserimento del catalizzatore, in modo tale da assicurare un'illuminazione uniforme. La vetrina in silice permette l'illuminazione del letto catalitico, è esposta alla temperatura ambientale e ha un raggio di 0.64 cm. Un controllore di temperatura Harrick ATK/low voltage regola la temperatura del catalizzatore. Il circuito di acqua di raffreddamento è controllato da un Masterflex Console Drive. L'illuminazione è effettuata utilizzando la luce visibile tramite un Schott KL 2500 LED. Il gas cromatografo Agilent Technologies 490 Micro GC è impiegato per identificare e quantificare i gas prodotti. Prima di ogni test il catalizzare viene sottoposto al processo preliminare di riduzione, effettuata a 320°C per 30 minuti ad opera di una corrente di H_2/N_2 al 5% in volume. Il reattore è stato impiegato mantenendo

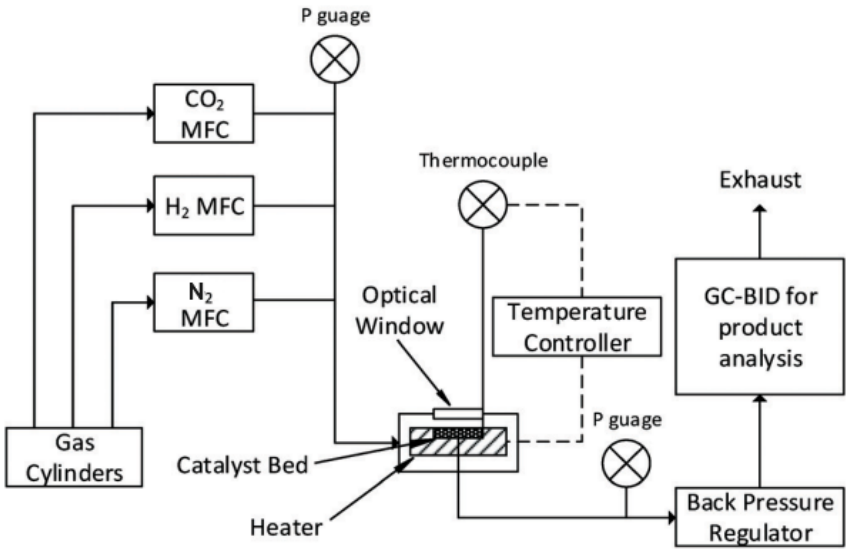

Figura III: Impianto sperimentale per test di attività catalitica in condizioni "dark" e "light" (catalizzatore esposto a radiazione luminosa) [2].

bassi i valori di conversione di CO_2, tipicamente inferiori al 15%. Ciò è stato fatto per far si che il reattore operasse in condizioni di limite cinetico, senza essere soggetto a limitazioni di massa, calore o trasporto della luce. In ogni esperimento la pressione dei gas in ingresso è mantenuta costante e pari a 1 bar. Il catalizzatore è stato testato variando la composizione dei reagenti in ingresso a temperatura costante e pari a 300°C. I valori testati sono stati, $CO_2/H_2 = 25/60$, 1, 1.5, in condizioni "dark" e "light". Per determinare l'incremento della produzione di CO dovuto all'irradiazione luminosa sono stati misurati la differenza tra le velocità di reazione come incremento assoluto (Light-Dark) e relativo (Light/Dark). I risultati in condizioni equimolari e di surplus di CO_2 hanno dato risultati simili e superiori alla condizione di surplus di idrogeno. Per tale motivo tutti gli esperimenti successivi sono stati eseguiti imponendo una frazione nel feed in ingresso CO_2/H_2=1 (Absolute gain = 0.4 mmol/gcat/min; Relative gain = 1.3). Per studiare la dipendenza della velocità di reazione dalla temperatura, essa è stata variata nel range 230-320°C, sia in condizioni "dark" che "light". L'illuminazione tramite luce visibile ha portato ad un miglioramento della produzione di CO lungo tutto il range di temperature analizzato. La Figura IV mostra come l'incremento della velocità di reazione diminuisce quando la temperatura aumenta da 230 a 320°C. Ciò suggerisce che l'effetto plasmonico sia meno dominante ad alte temperature. Inoltre l'impiego della luce visibile permette di impiegare temperature di processo più basse per ottenere performance catalitiche paragonabili a quelle in assenza di luce. Dato che a 230°C è stato misurato il maggior incremento causato dall'irradiazione luminosa, tale temperatura è stata mantenuta per tutti gli esperimenti successivi. Tali dati sono stati anche impiegati per disegnare il plot di Arrhenius e quindi calcolare le energie di attivazioni apparenti per la reazione di RWGS, rappresentato in Figura V. La diminuzione dell'energia di attivazione da 83 a 50 kJ/mol in condizioni di irradiazione luminosa, è indicativa di un "hot carrier-driven mechanism", vale a dire di un meccanismo di reazione in cui fotoelettroni generati dall'effetto LSPR del rame (o potenzialmente trasferiti dal ZnO eccitato) vengono trasferiti agli orbitali di antilegame della CO_2 adsorbita, formando una specie a carica parziale negativa tale da ridurre l'energia di attivazione per la reazione.

La differenza tra un meccanismo di reazione mediato dal trasferimento elettronico e uno in cui il meccanismo di catalisi termica è semplicemente incrementato dall'aumento di temperatura dovuto all'irradiazione luminosa è anche rilevabile dall'analisi della dipendenza della velocità di reazione dalla potenza della luce incidente. Sono stati quindi condotti dei test di attività al variare della potenza della luce visibile irradiata, nel range 0-0.77 W. IL risultato mostra un andamento lineare, dove quindi la velocità di reazione è direttamente proporzionale alla velocità dei fotoni incidenti e di conseguenza alla potenza della luce. Ciò va a confermare la presenza di un meccanismo di reazione foto-catalitico in cui gli elettroni eccitati vanno ad interagire in maniera efficace con i reagenti adsorbiti sulla superficie del catalizzatore, aumentando le

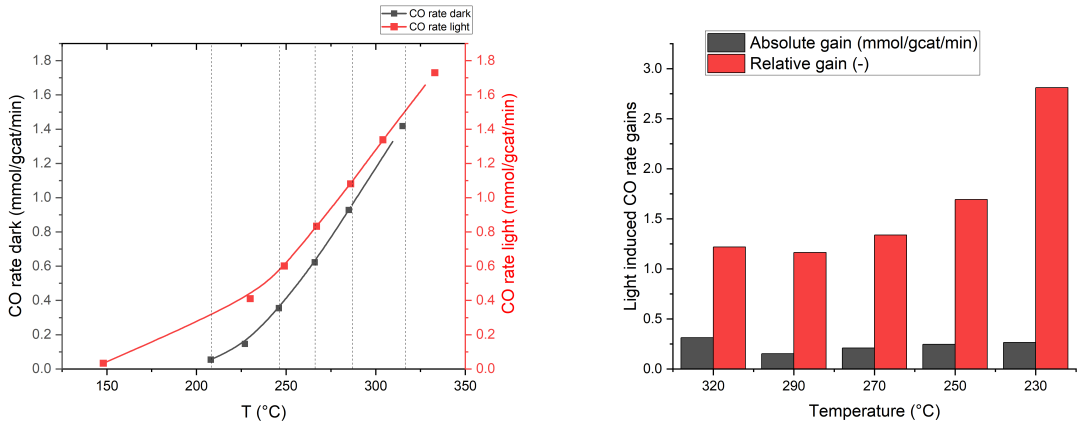

Figura IV: Dipendenza della velocità di produzione di CO dalla temperatura: (a) velocità di produzione in condizioni ”dark” e ”light” (b) incremento assoluto e relativo calcolato nel range di temperature 230-320°C. Condizioni sperimentali: p=1 bar, CO_2/H_2=1, portata totale = 30 mL/min, quantità di catalizzatore = 22 mg.

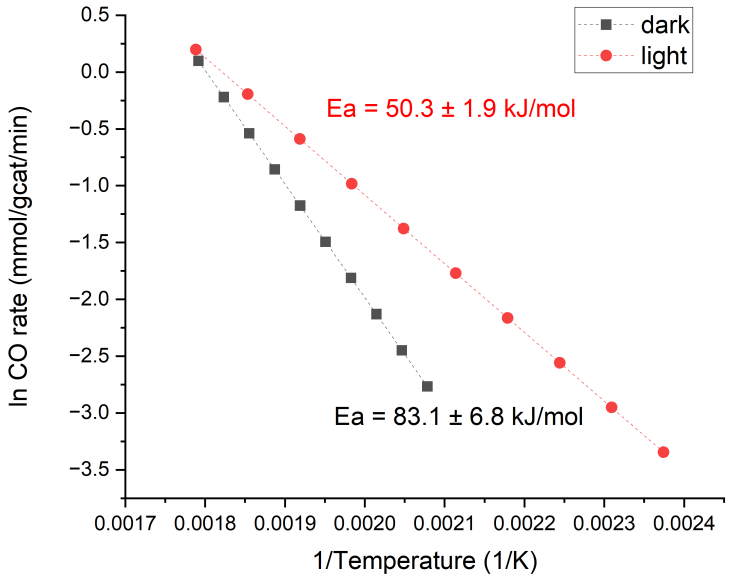

Figura V: Energie di attivazione calcolate per la reazione di RWGS in condizioni ”dark” e ”light” (plot di Arrhenius).

performance catalitiche.

Tramite l'impiego di filtri ottici sono state testate tre diverse bande della luce visibile: 400–450 nm, 500–600 nm, e 600–700 nm. L'intervallo 400-450 nm corrisponde al band gap del ZnO (3.2 eV), mentre l'intervallo 500-600 nm va a coprire l'effetto LSPR del rame. Le velocità di produzione del CO misurate mostrano tutte un incremento rispetto alla condizione di assenza di irradiazione luminosa, ma in maniera differente tra loro. Tutti i test sono stati effettuati alla temperatura di 230°C e con una potenza della luce incidente pari a 228 mW, in modo tale che l'effetto del riscaldamento esterno fosse lo stesso durante tutti gli esperimenti. L'aumento nelle prestazioni foto-catalitiche non può così essere spiegato solo tramite un riscaldamento ottico, ma è una ulteriore prova di un meccanismo di reazione dovuto al trasferimento elettronico e dell'importanza dell'energia dei fotoni luminosi. Infatti, al diminuire dell'energia dei fotoni, e quindi all'aumentare della lunghezza d'onda della luce impiegata, la velocità di reazione misurata diminuisce. I dati sperimentali raccolti sono stati impiegati per calcolare l'Apparent Quantum Yield per i tre intervalli di lunghezza d'onda testati:

$$AQY = \frac{\text{numero di elettroni nella reazione}}{\text{numero di fotoni incidenti}} \times 100$$

Tale valore rappresenta la frazione di energia luminosa che è effettivamente usata dal catalizzatore per la reazione chimica. Il numero di elettroni è calcolato dalla differenza tra la velocità di reazione in condizione "light" e "dark", in modo tale da considerare solo l'influenza dell'irradiazione luminosa. I dati così ottenuti sono riportati nella figura sottostante: Tali risultati mostrano come i fotoni blu, vale a dire quelli a lunghezza

Wavelength range (nm)	AQY (%)
400-450	10.6
500-600	6.5
600-700	4.7

Tabella II: AQY calcolato al variare della lunghezza d'onda della luce incidente.

d'onda inferiore, siano più efficaci nell'incrementare la velocità di produzione di CO. Essa infatti appare determinata non solo dallo spettro di assorbimento del foto-catalizzatore, ma anche del livello energetico degli orbitali delle molecole reagenti, in questo caso la CO_2, suggerendo la presenza di una soglia energetica che gli elettroni devono oltrepassare per trasferirsi nell'orbitale di antilegame della CO_2 e portare alla rottura del legame C-O. Tale soglia è determinata dall'allineamento tra i livelli energetici degli elettroni eccitati (e quindi dei fotoni incidenti) e degli orbitali molecolari dei reagenti. Le lunghezze d'onda inferiori sono quindi necessarie per andare a generare una quantità consistente di elettroni eccitati che abbiano energia tale da essere trasferiti al LUMO della CO_2. L'eccitazione elettronica data dell'effetto LSPR è la promozione collettiva degli elettroni di conduzione delle nanoparticelle metalliche dovuta alla risonanza della luce incidente. In particolare, la quantità di elettroni eccitati differisce in gran numero della promozione dovuta all'assorbimento di un singolo fotone. Di contro, l'energia degli elettroni generati dall'effetto LSPR è inferiore, e ciò limita la possibilità di indurre reazioni dotate di una soglia energetica elevata. Tale effetto spiega i valori di AQY calcolati, e come siano superiori a lunghezze d'onda inferiori.

L'analisi della dipendenza della velocità di reazione rispetto alle concentrazione di CO_2 e H_2 è stata condotta con l'obiettivo di andare a investigare come l'irradiazione luminosa va a modificare il meccanismo di reazione. Nonostante gli ordini di reazione non siano gli unici valori determinanti il meccanismo di reazione, essi possono dare indicazioni circa la sua origine a livello atomico. I risultati sono riportati in Figura VI: L'ordine di reazione relativo alla concentrazione di CO_2 è rimasto relativamente costante, passando da 0.89 a 0.81. Tali valori, vicini all'unità, suggeriscono come la reazione di RWGS possa essere limitata dalla reazione di dissociazione della CO_2 sia in condizioni "dark" che "light". Il più grande cambiamento dovuto all'irradiazione luminosa è stato ritrovato nell'ordine di reazione rispetto alla concentrazione di idrogeno, da 0.7 a -2.6. Un ordine di reazione inferiore all'unità è caratteristico di una specie reagente adsorbita in superficie che va a inibire la velocità di reazione. Per tale motivo, il decremento misurato in presenza di irradiazione luminosa indica che le specie adsorbite H* sono presenti in quantità sufficiente da avvelenare i

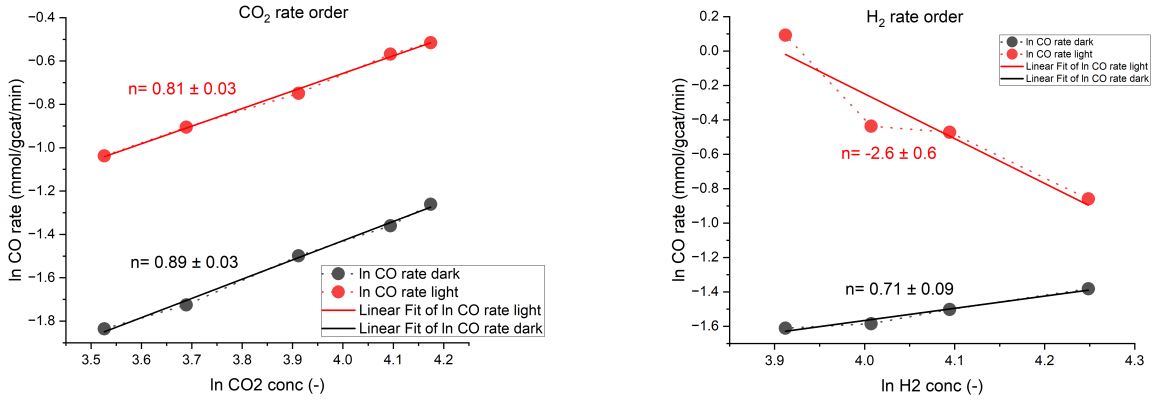

Figura VI: Dipendenza della velocità di produzione della CO dalla concentrazione di (a) CO_2 e (b) H_2, in condizioni "dark" e "light" per la reazione di RWGS su catalizzatore CZA. Condizioni sperimentali: T=230°C, p=1 bar, portata totale = 40 mL/min, quantità di catalizzatore = 22 mg, portata del secondo reagente mantenuta costante e pari a 11.4 mL/min per H_2 e 12 mL/min per CO_2 usando N_2 come gas inerte.

siti catalitici. Ciò può essere spiegato dall'effetto LSPR del rame che va a indurre un miglioramento della performance catalitica della rottura del legame H-H, aumentando la concentrazione superficiale di specie H*.

Il desorbimento separato di CO_2 e H_2 dalla superficie del catalizzatore è stato studiato sfruttando uno spettrometro di massa (MS) per monitorare in modo continuo i gas effluenti. Inizialmente, in condizioni di assenza di luce, una corrente di H_2/He è stata inviata al reattore per ridurre preliminarmente il catalizzatore. A tale step sono susseguiti uno step di spurgo condotto con He e il feeding di CO_2 al reattore. Dopo 30 minuti tale flusso è stato interrotto e al suo posto il reattore è stato alimentato con H_2. Inoltre tale punto decreta la fine della fase "dark", con l'irradiazione del reattore con luce visibile. Gli stessi passaggi sono stati ripetuti nella fase "light". In Figura 8.12 sono riportati i risultati ottenuti, e un ingrandimento della parte di grafico riquadrata in rosso, in modo da distinguere correttamente il comportamento dei segnali relativi a CO_2 e CO nelle fasi di adsorbimento della CO_2 e di ingresso di idrogeno in condizione di irradiazione luminosa. A seguito dell'introduzione di CO_2, le curve relative al CO hanno seguito l'andamento di quelle relative alla CO_2. Tuttavia, non è visibile nessun picco relativo alla formazione di CO, indicando che il meccanismo redox non è il percorso principale per la reazione di RWGS, non vi è alcuna produzione di monossido di carbonio sulla superficie di catalizzatore dovuta solo all'interazione dell'anidride carbonica. Al contrario, l'alimentazione successiva di H_2 porta alla formazione di un picco per CO, il cui segnale passa da 1.9×10^{-10} a 4.9×10^{-10}. Ciò implica che la presenza di idrogeno è necessaria alla formazione di CO. Tale risultato vale allo stesso modo i condizioni "light". Il segnale relativo a H_2O è anche rilevato, nonostante di magnitudine di molto inferiore agli altri, e anch'esso subisce un incremento successivamente all'introduzione di H_2.

La spettroscopia ultravioletta-visibile (DRS) è una tecnica spettroscopica utilizzata per l'analisi di polveri e superfici. I campioni $CuSiO_2$ e CZA, post riduzione preliminare, sono stati analizzati in situ, sia a temperatura ambiente che alla temperatura di reazione pari a 230°C. Dalle analisi è stata determinata la percentuale di luce incidente riflessa dal campione nell'intervallo di lunghezze d'onda 200-800 nm. Per migliorare l'interpretazione dei dati la funzione di Kubelka-Munk è stata calcolata lungo tutto lo spettro UV-vis tramite l'espressione:

$$F(R) = \frac{k}{s} = \frac{(1 - R_\infty)^2}{2R_\infty}$$

I risultati sono illustrati in Figura VII: Come mostrato in figura, il picco di assorbimento del CuO a circa 750 nm non è visibile in nessuno dei campioni, ulteriore prova dell'efficacia dell'idrogenazione preliminare effettuata nel ridurre i cristalliti di CuO a Cu metallico, che quindi non presenta alcun band gap. Per tale motivo esso presenta un assorbimento intenso lungo tutto lo spettro UV-vis. Per il composto $CuSiO_2$ alla

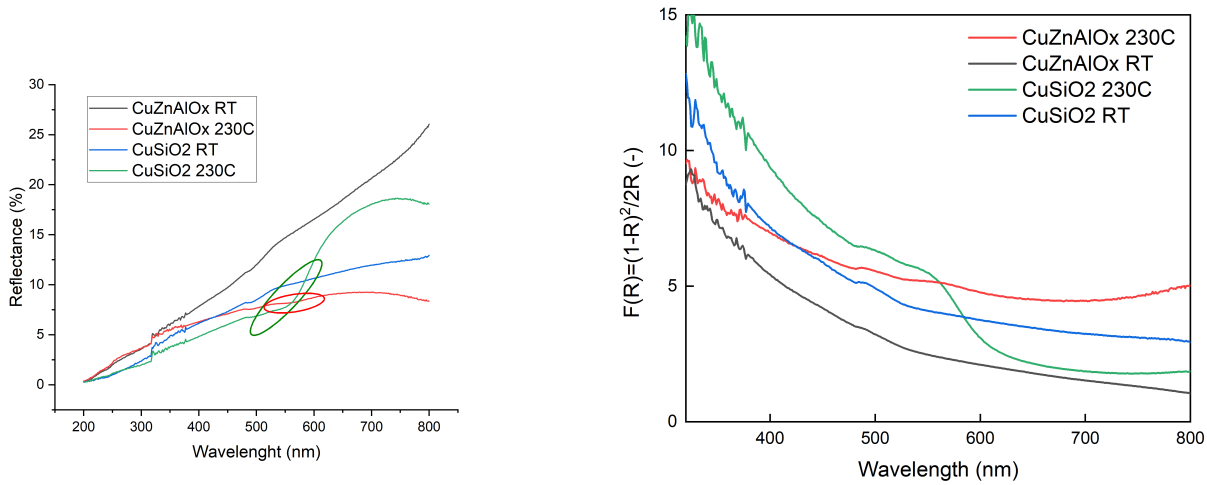

(a) **(b)**

Figura VII: Spettro ultravioletto-visibile

temperatura di reazione è chiaramente riconoscibile il picco di assorbimento a circa 570 nm, corrispondente alla risonanza del rame metallico (effetto LSPR). Tale picco è molto meno marcato nel catalizzatore CZA, probabilmente a causa della dimensione ridotta dei cristalliti di rame, come confermato dai dati stimati dall'equazione di Scherrer. Il picco di assorbimento di ZnO a circa 390 nm non è visibile dai grafici, probabilmente perchè nascosto dalla sovrapposizione con il più intenso assorbimento del Cu metallico. Inoltre i dati relativi all'assorbimento di ZnO sono stati impiegati per calcolare l'energia di band gap del semiconduttore, vale a dire l'energia necessaria per eccitare un elettrone dala banda di valenza alla banda di conduzione. Ciò è stato fatto calcolando il Tauc plot per il catalizzatore CZA a 230°C, considerando un band gap diretto per il ZnO. A tal proposito è stata impiegata l'equazione di Tauc:

$$(\alpha h\nu)^{\gamma} = A(h\nu - E_g)$$

Il plot del termine a sinistra in funzione dell'energia dei fotoni $h\nu$ e il successivo fit lineare della regione ad alte energie ha permesso di determinare un'approssimazione dell'energia di band gap di ZnO dall'intersezione del fit con l'asse delle ascisse. Il risultato ottenuto, pari a 5.76 eV, differisce dal valore sperimentale, pari a circa 3.37 eV. Ciò può essere dovuto alla dipendenza del l'energia di band gap dalla dimensione dei cristalliti di ZnO. Infatti, quando essa risulta inferiore al raggio di Bohr, si verifica un fenomeno chiamato confinamento quantico, tale da modificare le proprietà ottiche dell'eccitone, vale a dire lo stato legato di elettrone e lacuna. Di conseguenza le nanoparticelle di ZnO possono presentare un'energia di band gap superiore a 4.5 eV, ma la loro dimensione deve essere inferiore o comparabile al raggio di Bohr dell'eccitone, pari a 2.3 nm.

La spettroscopia DRIFT è stata effettuata in situ per investigare l'adsorbimento di CO_2 sul catalizzatore CZA alle condizioni di reazione, sia in condizioni "dark" che "light". L'obiettivo di tali test era l'identificazione di possibili intermedi di reazione in modo tale da studiare la reattività ed eventualmente ottenere informazioni circa il meccanismo di reazione. Essi sono stati effettuati impiegando uno spettrometro Perkin Elmer e un reattore con geometria "praying mantis" (VCDRM-5, Harrick). Per l'illuminazione del catalizzatore è stato impiegato il LED Schott KL2500. Dopo il processo di riduzione preliminare del catalizzatore a 320°C, da parte di una corrente di H_2/Ar con rapporto 2:1 per 30 min, il campione è stato raffreddato a 230°C ed esposto a 20 mL/min di una corrente di CO_2/He con rapporto 1:1 e 10 mL/min di idrogeno per 60 minuti, in modo da far avvenire la reazione di RWGS. Successivamente il flusso di CO_2/He è stato interrotto e sono stati mandati al reattore 20 mL/min di Ar. Ciò ha causato l'evacuazione di CO_2 e il desorbimento degli intermedi di reazione formatisi. La stessa procedura è stata impiegata in condizioni di irradiazione luminosa. I dati sono stati raccolti subito prima e immediatamente dopo la chiusura del flusso di CO_2, nel range 800-2200 cm^{-1}. Gli spettri di assorbimento dell'infrarosso risultanti hanno mostrato, nel primo caso, la crescita delle bande e la formazione dei picchi a causa dell'adsorbimento della CO_2 sulla superficie del catalizzatore. Il

secondo caso, di maggior interesse per gli studi meccanicistici, rappresenta la decrescita dei picchi a seguito dell'evacuazione della CO_2. Il range 1990-2200 cm^{-1} rappresenta la regione caratteristica dello stretching del legame C-O, e quindi del CO adsorbito sul catalizzatore, lineare e in fase gas. Dai diagrammi sono stati chiaramente visibili due picchi a circa 2174 e 2115 cm^{-1}. Il range 1300-1650 cm^{-1} è invece caratteristico delle vibrazioni del legame C-O nelle specie carbonato (unidentato e bidentato) e formato. In tale regione sono stati ritrovati i picchi più intensi, per la precisione approssimativamente a 1594 e 1372 cm^{-1} (HCOO*). In condizioni di irradiazione luminosa è stato rilevato anche un altro picco a circa 1507 cm^{-1}, che può essere associato a CO_3* bidentato. Un altro picco relativo all'intermedio carbonato è stato trovato a circa 815 cm^{-1}. Sono inoltre rilevabili dei gruppi metossidici, con un picco caratteristico a 1075 cm^{-1}. Le più grandi differenze tra le condizioni "dark" e "light" riguardano l'intensità dei picchi di adsorbimento e la scomparsa di alcuni picchi successivamente al cut-off della CO_2. Infatti, in condizioni "dark", è stata osservabile la scomparsa di tutti i picchi eccetto i due relativi al formato a 1594 e 1372 cm^{-1}, a riprova del fatto che il formato è un intermedio di reazione stabile. Al contrario, quando la luce visibile è stata irradiata, anche il picco a circa 1372 cm^{-1} è scomparso, suggerendo che una quantità maggiore di formato viene convertita a CO. Inoltre, in condizioni "light", si rileva una diminuzione della concentrazione di formato. Ciò è stato accompagnato ad un aumento del CO prodotto, rilevabile da un incremento dell'altezza dei picchi, confermando i risultati ottenuti dai test di attività.

Nel corso di tale lavoro di tesi è stata studiata l'idrogenazione di CO_2 a CO utilizzando il catalizzatore commerciale Cu-ZnO-Al_2O_3, e come l'irradiazione di luce visibile, e quindi la tecnologia innovativa della foto-termo catalisi, va ad influire sulla reazione. Gli esperimenti preliminari sono stati progettati e svolti in modo tale da variare le condizioni di reazione, quali temperatura, portata e concentrazione dei reagenti, ma anche lunghezza d'onda e potenza della luce visibile irradiata, e quindi determinare le condizioni di lavoro ottimali. Tutti i test di attività hanno mostrato un incremento della velocità di produzione di CO a seguito dell'irradiazione luminosa, fino ad un massimo di 2.8 volte nelle condizioni T=230°C, H_2/CO_2=1. La spettroscopia DRIFT, effettuata in situ, ha confermato come la luce visibile porti ad un incremento della reattività delle specie adsorbite sulla superficie del catalizzatore, con una maggiore formazione di specie gassose CO. I test successivi hanno avuto come obiettivo l'ottenimento di informazioni sul meccanismo della reazione di RWGS su CZA, e se e come esso è modificato dall'introduzione di luce visibile. I risultati ottenuti circa l'aumento della velocità di reazione, il decremento dell'energia di attivazione, la dipendenza lineare della velocità di reazione dalla temperatura e il variare delle velocità misurate al variare della lunghezza d'onda della luce irradiata, hanno suggerito il verificarsi di un meccanismo dovuto al trasferimento di elettroni, generati a seguito dell'effetto LSPR di Cu, o potenzialmente trasferiti dall'eccitazione di ZnO. Tali elettroni vanno ad occupare gli orbitali di antilegame delle molecole di CO_2, promuovendo la sua attivazione, la scissione del legame C-O e le reazioni successive. Inoltre i risultati circa la variazione delle lunghezza d'onda hanno mostrato come i fotoni blu, vale a dire a inferiori lunghezze d'onda, sono i più efficaci nell'incremento della produzione di CO, portando a più alti AQY. L'analisi cinetica ha permesso il calcolo degli ordini di reazione rispetto ai reagenti, suggerendo un incremento della concentrazione di specie superficiali H*, probabilmente dovute a all'effetto LSPR del rame che induce una maggiore attività catalitica nella scissione del legame H-H. Il meccanismo di reazione è quindi effettivamente alterato dall'interazione della luce con la superficie del catalizzatore. In conclusione, la riduzione foto-termo catalitica di CO_2 su catalizzatore CZA, si è dimostrata una tecnologia interessante e promettente, sia dal punto di vista della sostenibilità che dell'efficienza.

Contents

List of Tables

List of Figures

1 Introduction

The current global socio-economic system is intrinsically tied to the utilization of fossil fuels, which serve both as primary energy sources and raw materials for a vast array of man-made products. These products range from gasoline, diesel oil, petrochemicals, and chemical substances to synthetic materials, plastics, and pharmaceuticals. Unfortunately, these valuable resources, which nature has formed over countless eons, are depleting at a rapid rate. Fossil fuels are not only dwindling but also becoming more expensive over time. Thus, it is imperative to seek new sources and solutions. All fossil fuels are composed of hydrocarbons with varying carbon-to-hydrogen ratios. When burned, they are irreversibly consumed, with carbon turning into carbon dioxide and hydrogen into water. This process significantly contributes to the increase in atmospheric carbon dioxide content, which is a major human-made factor in global warming. During the 16th and 17th centuries, coal became the dominant source of fuel at the beginning of the Industrial Revolution, replacing the increasingly scarce wood. The invention of the steam engine in the 18th century led to an even wider use of coal, driving the Industrial Revolution forward. Coal continued to meet growing energy needs throughout the 19th and 20th centuries, mainly used to generate electricity. Coal reserves may last for another two or three centuries. However, socio-economic, safety and environmental factors are increasingly challenging coal mining, particularly in areas unsuitable for surface strip mining. Since the latter part of the 19th century, petroleum oil and natural gas have become increasingly essential energy sources and raw materials for various industries. Estimated world oil and gas reserves appear substantial, they have not significantly decreased in the last 50 years, thanks to continuous advancements in exploration and production technologies. Despite this, we must consider the growing world population, increasing living standards, and rising demand in countries like China and India. Based on current estimates, proven oil reserves would last for about 40 years at the present consumption rate [23].

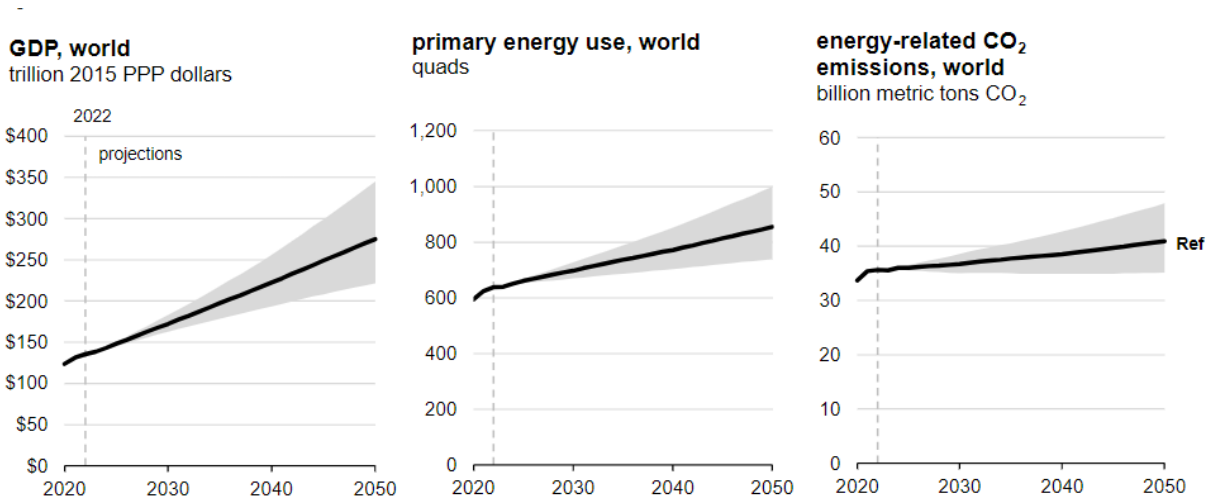

Figure 1.1. Energy market with history data up to 2023 and projected data from 2023 to 2050 [3] Note: For each projection year, the shaded areas represent the maximum and minimum values. Quads = quadrillion Btu.

In fact the ongoing expansion of the global population and substantial enhancements in human living standards have led to a considerable upswing in energy consumption in recent decades. Simultaneously, the extensive dependence on fossil fuels contributes significantly to environmental degradation, introducing pollutants into the natural surroundings. This phenomenon has given rise to serious environmental issues. Notably, a key environmental concern is the escalating global warming attributed to the release of greenhouse gases, including carbon dioxide (CO_2), methane (CH_4), nitrous oxide, and ozone. The cumulative impact of these emissions poses a significant threat to the planet's ecological balance and underscores the imperative for sustainable and environmentally friendly energy alternatives [6]. To address the ever-growing energy needs, it's crucial to explore alternative energy sources. Hydro- and geothermal energy are harnessed where feasible,

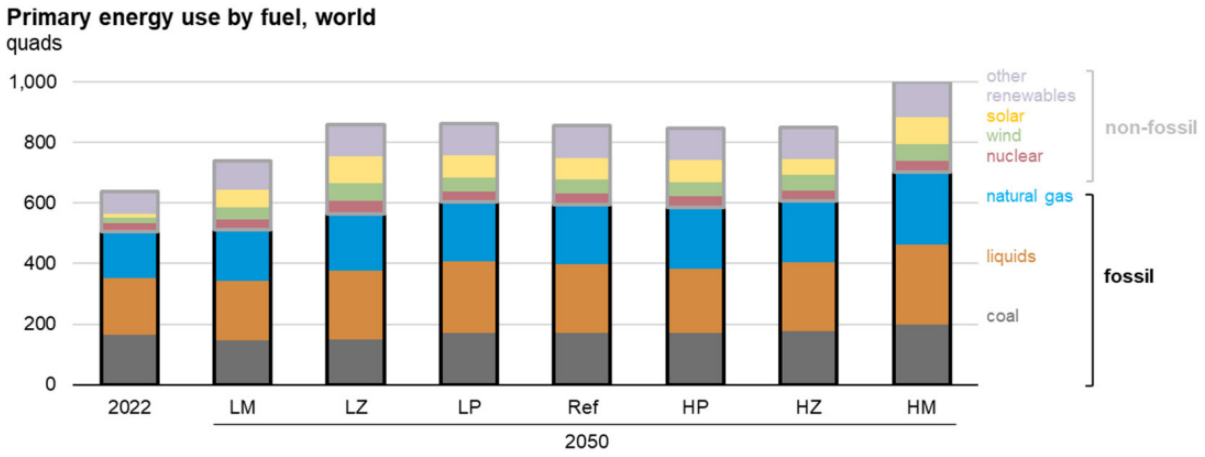

Figure 1.2. Primary energy use by fuel [3] Note: Quads = quadrillion Btu; HM=High Economic Growth; LM=Low Economic Growth; HP=High Oil Price; LP=Low Oil Price; HZ=High Zero-Carbon Technology Cost; LZ=Low Zero-Carbon Technology Cost.

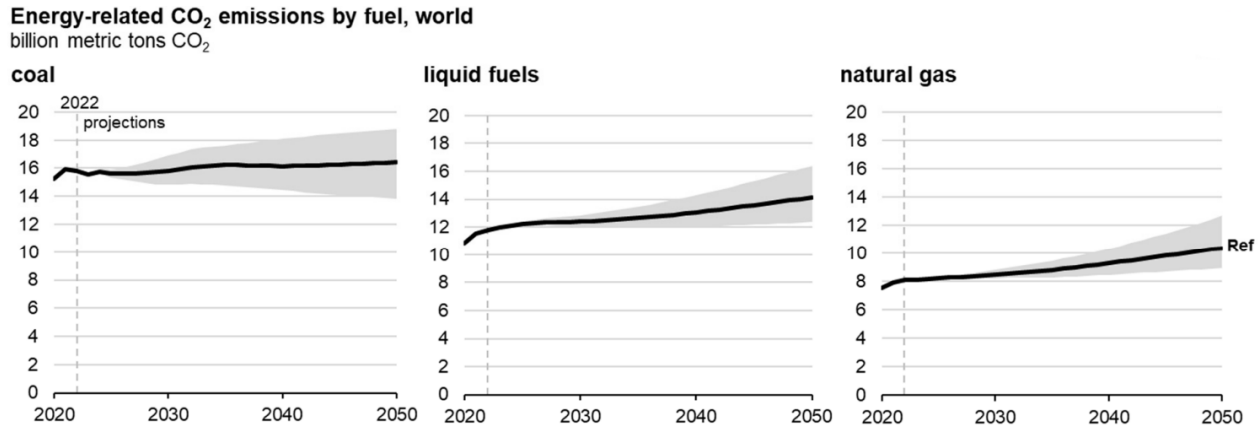

Figure 1.3. Energy-related CO_2 emissions by fuel [3] Note: For each projection year, the shaded areas represent the maximum and minimum values.

but they are unlikely to replace fossil fuels on a large scale in the near future. Nuclear energy, despite its initial promise, faces public opposition and safety concerns. The decline of the atomic energy industry is unfortunate. However, atomic energy remains a viable long-term energy source. Saving energy and using alternative energy sources are essential, but they alone cannot fully substitute for traditional energy sources to cover humanity's massive energy needs. Fossil fuels, especially oil and gas, remain the most convenient sources of transportation fuels and energy due to their well-established infrastructure for transport and distribution. Most fossil fuels are used to generate electricity. There are still unresolved challenges in efficient energy storage and distribution. Hydrogen, leading to the concept of a 'hydrogen economy', has been identified as a clean fuel source. However, there are significant challenges in handling, storing and distributing hydrogen, which make its large-scale deployment economically prohibitive [23].

Several strategies have been proposed for the control of CO_2 emissions. The primary approach involves the reduction of CO_2 emissions at the source through the use of renewable energy carriers or by enhancing the efficiency of existing fossil fuel-based energy systems. Another strategy entails the reduction of emitted CO_2 through the application of CO_2 capture and sequestration (CCS) technologies, but the process demands a significant energy input and meticulous measures to prevent the leakage of CO_2 back into the atmosphere [7]. In this context a more promising avenue is the utilization of CO_2 as a C1 building block for the synthesis of value-added chemicals and fuels. CO_2 is known for its stability, characterized by a high bond energy of

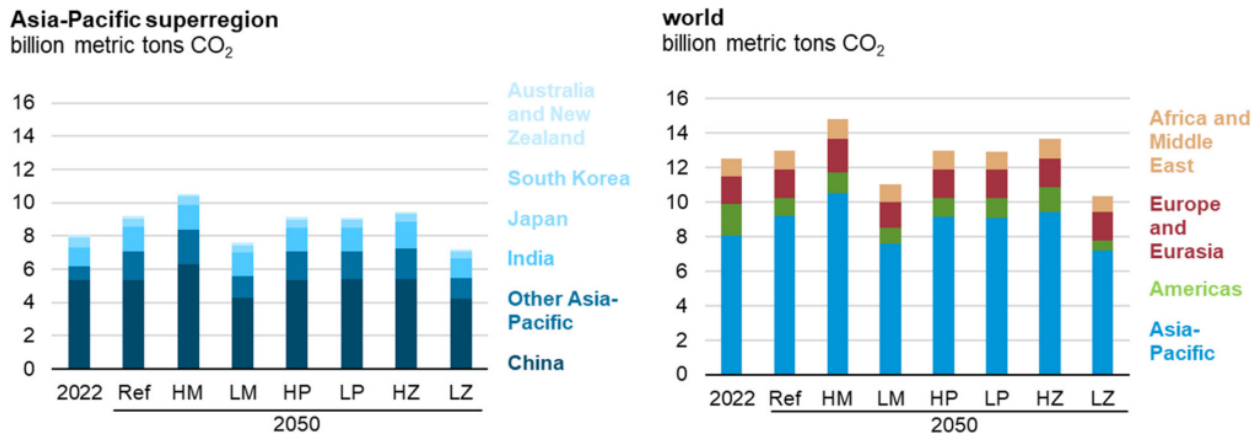

Figure 1.4. CO_2 emissions from electricity generation [3] Note: HM=High Economic Growth; LM=Low Economic Growth; HP=High Oil Price; LP=Low Oil Price; HZ=High Zero-Carbon Technology Cost; LZ=Low Zero-Carbon Technology Cost.

C=O (750 kJ mol-1). The reduction of CO_2 requires considerable energy inputs and is generally divided into thermo-, electro-, and photocatalytic reactions. In chemical synthesis, often termed the non-reductive route, the chemical state of carbon remains at +4 in the products, which include substances like urea, organic carbonates, carboxylic acids, polymers, and more. Conversely, in the fuel synthesis process, known as the reduction route, the chemical state of carbon is reduced to lower values in the products (Figure 1.5). These products encompass CH_4, carbon monoxide (CO), methanol, ethanol, formic acid, and various other hydrocarbons [6].

Solar fuels, often denoted by this term, can be combusted or utilized in fuel cells, leading to the release of CO_2. This process effectively closes the carbon cycle, establishing a paradigm for the cyclic utilization of fossil fuels in a hydrogen-carbon cycling manner and so eliminating the need for external additions of CO_2 from fossil fuels [24]. The concept of a "methanol economy" has been proposed for such a cycle, particularly when methanol is derived from CO_2. A notable advantage of this approach lies in the minimal adjustments required for the existing energy production and transport infrastructure. The conversion of CO_2 into liquid or gaseous fuels holds an additional significance in high-density storage of solar energy, stored within chemical bonds, predominantly C-H bonds. While renewable sources typically offer intermittent and unreliable energy supplies, the storage capacity of solar fuels becomes an attractive solution. Beyond serving as fuel, some products resulting from CO_2 conversion can be conveniently utilized in chemical synthesis. This perspective transforms CO_2 from an undesired waste, potentially harmful to the planet, into a valuable and cost-effective carbon feedstock, capable of replacing fossil fuels in various applications [7]. This technology offers a dual benefit by providing a means to mitigate both the scarcity of energy resources and the environmental impact associated with CO_2 emissions [6].

Among the considerable efforts that have been made to capture, store and use carbon dioxide in the search for sustainable energy solutions and environmental protection, the photocatalytic reduction of CO_2 for the synthesis of CO stands out as a particularly promising approach. Although photo-thermal catalysis has promising applications, its wide implementation still needs to compete with traditional thermal processes. One of the main advantages of the photo-thermal approach is the possibility of increasing selectivity to target products by choosing adequate excitation wavelengths or light intensities. Hot-carrier chemistry has been shown to be highly effective in triggering specific reaction mechanisms by selectively activating molecular bonds of adsorbed species. This results in better selectivity than the thermochemical pathway. Photo-thermal catalysis also offers direct local heating at the nanoscale, concentrating heat at the surface of the active sites and avoiding unnecessary heating of the entire reactor system [8].

In the following chapters, the historical background and the state of the art of photo-thermal CO_2 conversion will be presented, as well as insights into the reaction studied and its reaction mechanism. The work will then focus on the catalyst, the reaction plant and reactor specifically used in this work. The following

description of the experimental path chosen is divided into three main chapters: a first one on the physical and chemical characterisation of the catalyst; a second one on the performance tests and the experiments carried out to study the reaction mechanism; a third and final one on the in situ spectroscopy tests. Each chapter will include an introduction to the experimental techniques used and their physical functionality, followed by the experimental procedures and results. The conclusions will be presented along with a discussion of the limitations of the work and suggestions for future improvements.

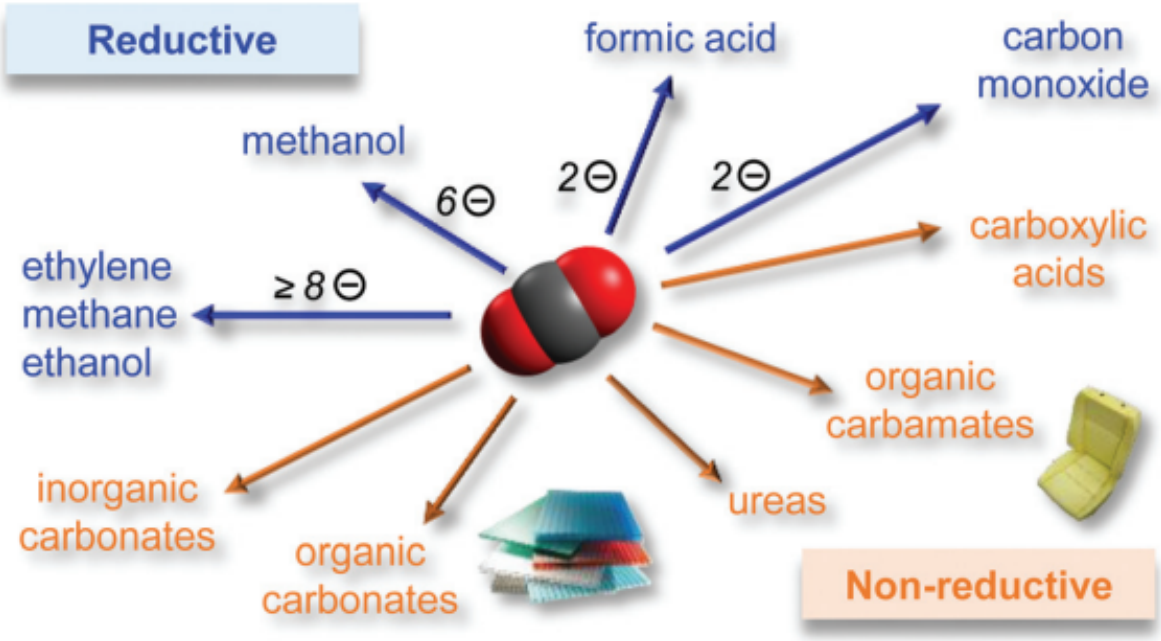

Figure 1.5. The technological utilization of CO_2 can be categorized into two main types of processes. The first involves low-energy exchanges, where carbon maintains its +4 oxidation state, leading to the production of chemicals (non-reductive). The second type involves high-energy exchanges, where carbon undergoes reduction (represented by electrons as minus signs in white circles), resulting in the production of fuels (reductive). Certain compounds from the second group, like CO, H_2CO, or HCOOH, are commonly used as chemicals but have the potential for conversion into fuels [4].

2 Photothermal catalysis

2.1 Reactions at surfaces

The secretary of the Royal Swedish Academy of Sciences, the renowned chemist Jöns Jacob Berzelius, has been publishing annual review articles on the most significant developments in the field of chemistry since 1820. Dating back to the early 19th century, various laboratories made observations indicating that certain substances could influence the progress of a chemical reaction without being consumed, seemingly unaffected by the reaction itself. For instance, in July 1823, Johann Wolfgang Döbereiner, a professor of chemistry at the University of Jena, communicated to his minister, Johann Wolfgang von Goethe, that *"finely divided platinum powder causes hydrogen gas to react with oxygen gas by mere contact to water, whereby the platinum itself is not altered"*. In a report published in 1835, Berzelius termed this phenomenon "catalysis". The term catalysis continued to be a subject of intense debate throughout the remainder of the century. It wasn't until around 1900 that Wilhelm Ostwald proposed a definitive definition based on the principles of chemical kinetics: *"A catalyst is a substance which affects the rate of a chemical reaction without being part of its end products"*. Ostwald's significant contributions to catalysis were recognized in 1909 when he was awarded the Nobel Prize in Chemistry. In 1909, Ostwald was awarded the Nobel Prize in Chemistry for his exceptional contributions to catalysis. Chemical reactions involve breaking and forming bonds between atoms, which is associated with energy transformation. Figure 2.1 illustrates the energy diagram that shows the progress of a reaction.

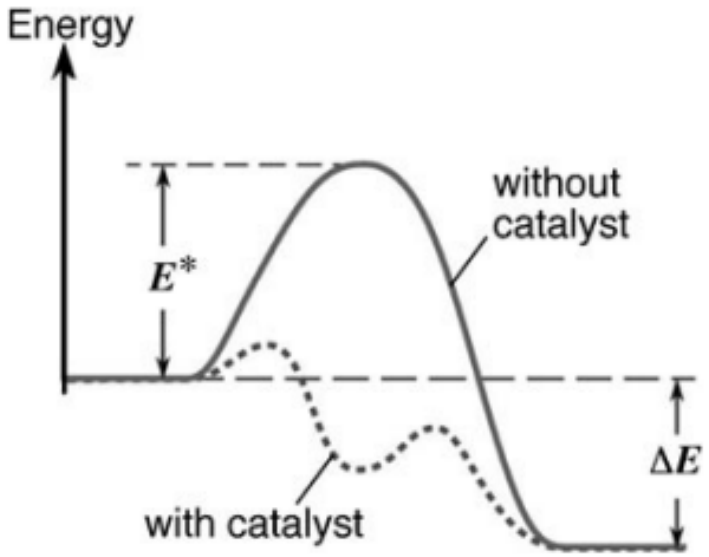

Figure 2.1. Energy diagram depicting the proceeding of a chemical reaction with and without a catalyst [5].

The activation energy, denoted as E^*, required to overcome the barrier is typically supplied by thermal energy kT, where k is Boltzmann's constant and T represents the temperature. Consequently, not all molecular encounters lead to successful reactions; only a fraction, $e^{-E^*/kT}$, is expected to overcome the activation energy barrier. Enhancing the reaction probability (or its rate) can be achieved by either elevating the temperature or reducing the activation energy. Catalysts contribute to the latter by forming intermediate compounds with the participating molecules. This process creates an alternative reaction path, as illustrated by the dashed line in Figure 2.1, associated with lower activation barriers and consequently a heightened overall reaction rate. In the final stage, the product molecules are released from the catalyst, which is then available for the subsequent reaction cycle. When the reacting molecules and the catalyst exist in the same phase (gaseous or liquid), the phenomenon is termed homogeneous catalysis. In biological systems, enzymes

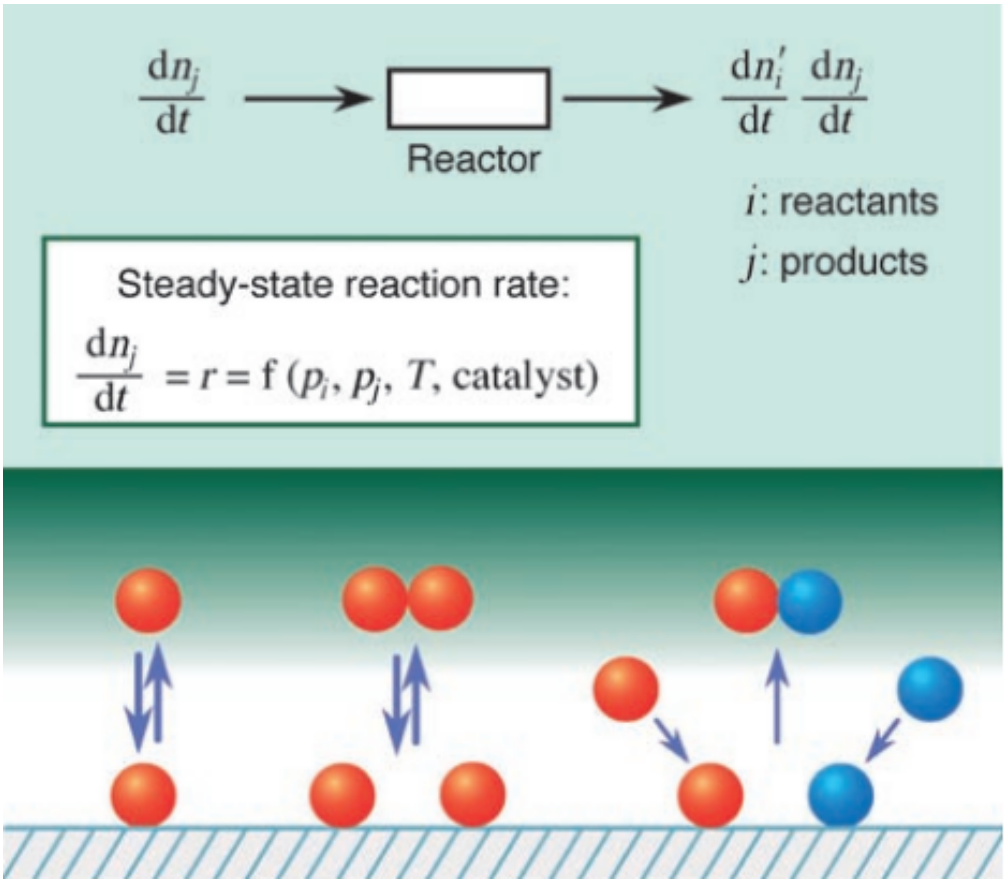

Figure 2.2. The principle of heterogeneous catalysis [5].

act as catalysts, while in technical reactions, the surface of a solid often plays a crucial role. Atoms in a solid's surface layer have fewer neighbors than those in the bulk, resulting in chemical unsaturation 2.2. These atoms can form new bonds (chemisorption) with suitable molecules from the adjacent gas or liquid phase, modifying or even breaking existing bonds (dissociative chemisorption). The surface species formed have the capability to move from one site to neighboring ones, potentially reacting with other species. The resulting molecules eventually depart from the surface (desorption). When used in a flow reactor, the catalyst can continuously function without being consumed [5].

Additionally, there arises the question of how the two-dimensional chemistry occurring in the chemisorbed overlayer can be investigated on an atomic scale. Irving Langmuir (Nobel Prize 1932) proposed a potential strategy many years ago: *"Most finely divided catalysts must have structures of great complexity. In order to simplify our theoretical consideration of reactions at surfaces, let us confine our attention to reactions on plane surfaces. If the principles in this case are well understood, it should then be possible to extend the theory to the case of porous bodies. In general, we should look upon the surface as consisting of a checkerboard…"*

Although the "surface science" approach envisioned by Langmuir was not experimentally accessible in his time, it began to become available in the 1960s with the introduction of ultrahigh vacuum (UHV) and surface-sensitive physical methods. Nowadays, a comprehensive array of such techniques is at our disposal to investigate the structural, electronic, or dynamic properties of well-defined single-crystal surfaces. The role of bond breaking during chemisorption is considered pivotal for a catalyst. Figure 2.3 shows in a schematic way the energetic transformations that occur when a diatomic molecule interacts with a perfect surface. As the molecule approaches the surface, it may form new bonds with surface atoms, weakening the bond between its own atoms. A corresponding one-dimensional energy diagram, as proposed by Lennard-Jones, is illustrated in Figure 2.3b: if the molecule A_2 forms a bond with the surface, it reaches a shallow minimum ($A_{2,ad}$).

Conversely, if the free A_2 molecule dissociates, the dissociation energy (E_{diss}) is required. Chemisorption of two A atoms is associated with strong bond formation ($2A_{ad}$), and the crossing point between the two curves signifies the activation energy for dissociative chemisorption, representing the reaction $A_2 \rightarrow 2A_{ad}$.

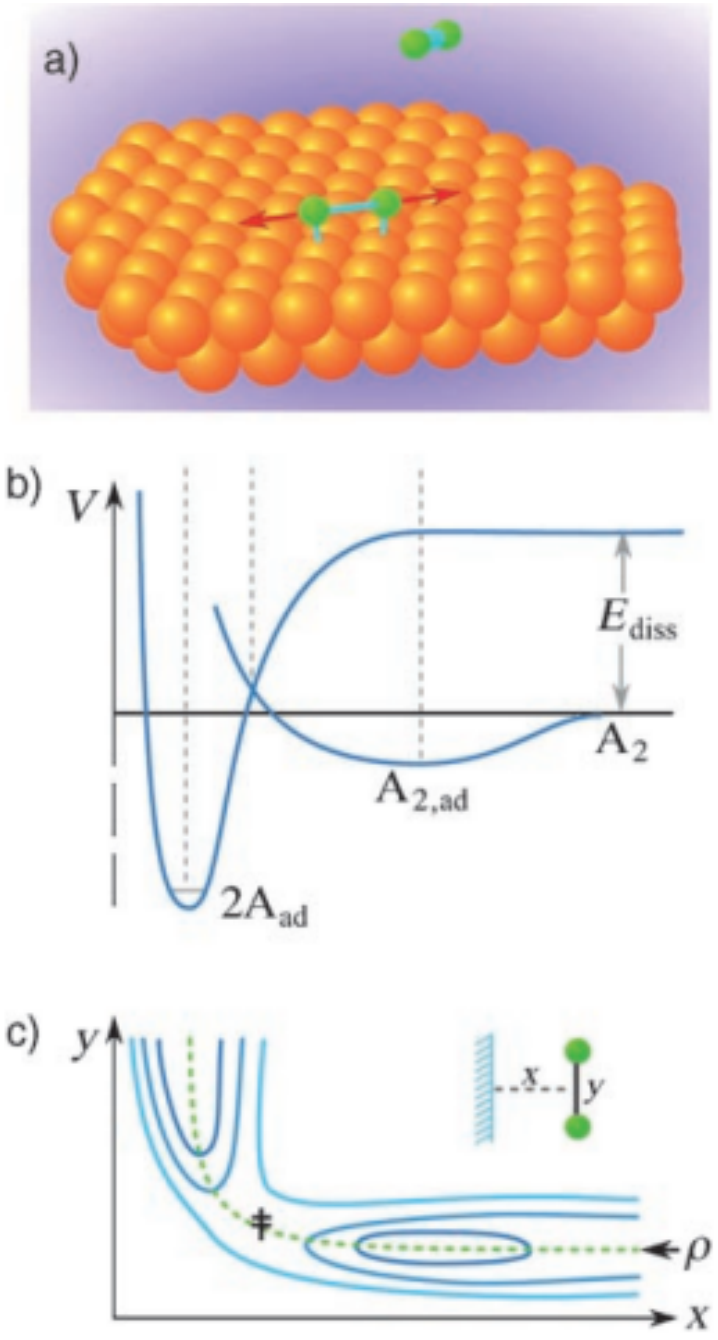

Figure 2.3. Lennard-Jones diagrams for the process of dissociative chemisorption of a diatomic molecule [5].

A more elucidating perspective is offered by a two-dimensional diagram (Figure 2.3(c)), where lines of equal energy are plotted as functions of the distance (x) between the molecule and the surface and the separation (y) between the two atoms [5].

2.2 History of CO_2 photocatalysis

The inception of research into the photocatalytic reduction of CO_2 can be traced back to 1972, marked by the pioneering work of Akira Fujishima and Kenichi Honda. Their discovery of the photoelectrochemical water splitting phenomenon on a titanium dioxide electrode, known as the Honda-Fujishima effect, laid the groundwork for subsequent investigations into photocatalysis, including the reduction of carbon dioxide.[25] In 1978, Halmann et al. achieved a pioneering breakthrough by reducing CO_2 in an aqueous solution, generating formic acid, methanol, and formaldehyde. This was accomplished through the use of a p-type semiconductor GaP photocathode [26]. Subsequently, in 1979, Inoue et al. introduced a suspension system incorporating various semiconductor photocatalysts such as WO_3, TiO_2, ZnO, CdS, GaP, and SiC. In this system, under light irradiation, CO_2 underwent conversion into formaldehyde, formic acid, and methanol. The researchers also delved into discussing the potential reaction mechanisms involved [27]. Building on these advancements, in 1987, Soichiro et al. employed SiC and ZnSe as photocatalytic materials, successfully reducing CO_2 to produce ethanol. Notably, this work marked the first synthesis of dicarbonic acids. The significance of this contribution significantly propelled the research and development of the field. Subsequently, numerous semiconductors have been identified as potential photocatalytic materials for CO_2 reduction under ultraviolet or visible-light irradiation. Some noteworthy examples include $SrTiO_3$ [28], Bi_2S_3 [29], ZnS [30], ZrO_2 [31], Cu_2O [32], other than SnO_2, Fe_2O_3 [24].

2.3 Definition of coupling of solar energy and thermal energy

Catalytic reactions involving the integration of solar energy and thermal energy can be broadly categorized into three main scenarios:

1. Photo-thermochemical cycle: the integration of photocatalysis and thermocatalysis occurs independently, as illustrated in Figure 2.4. During the initial half-reaction, ultraviolet-visible (UV-vis) light induces the creation of oxygen vacancies through photocatalysis. Subsequently, in the second half-reaction, carbon dioxide (CO_2) undergoes reduction into carbon monoxide (CO) through the action of oxygen vacancies in a thermocatalytic process.

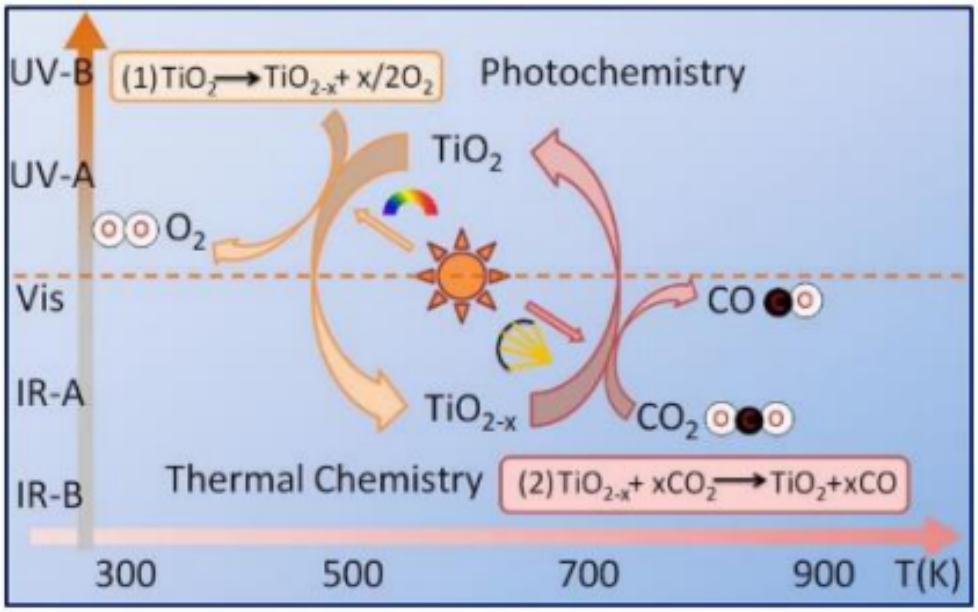

Figure 2.4. Photocatalysis-thermocatalysis cycle [6].

2. Photo-driven thermal catalysis: solar energy functions solely as the heating source, as depicted in Figure

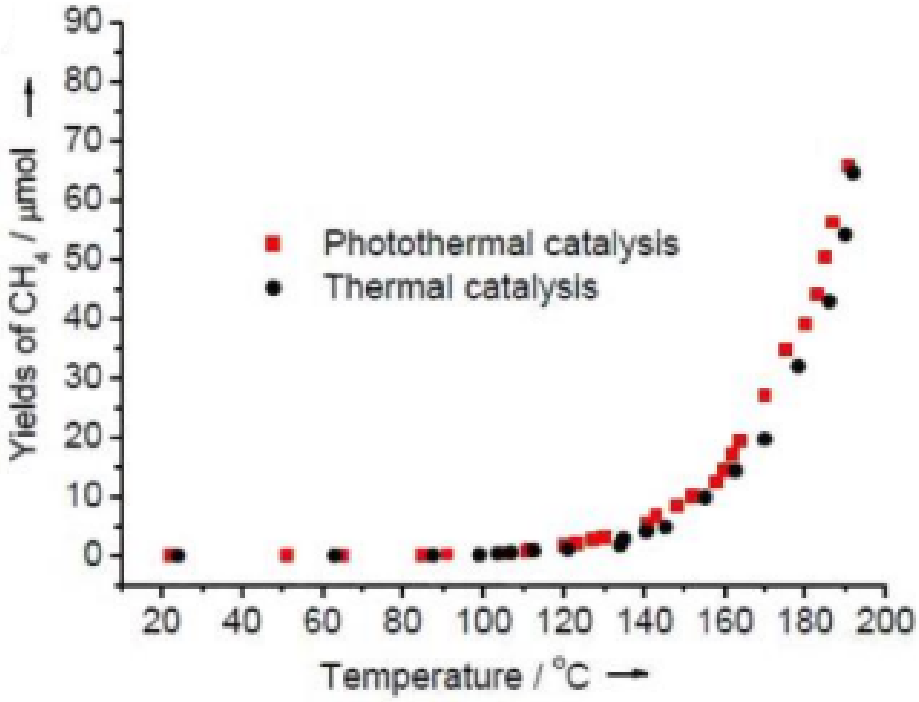

Figure 2.5. Photothermal catalysis [6].

2.5. The catalyst absorbs solar energy and undergoes photo-to-thermal conversion upon exposure to light. However, the subsequent reaction at elevated temperatures follows a similar pathway to traditional thermocatalytic reactions. In these conditions, photocatalysis plays a minimal role.

3. Photo-thermo catalysis: the third scenario involves the synergistic coupling of solar energy and thermal energy, where both photocatalysis and thermocatalysis actively participate in catalytic reactions, as depicted in Figure 2.6. This integrated approach, known as the photo-thermo effect, can lead to enhanced activity and/or selective control in the catalytic processes.

In comparison to the first two scenarios, the third one is considerably more appealing. This is due to the simultaneous utilization of both solar energy and thermal energy, making it a more integrated and efficient approach [6]. In fact, non-thermal activation mechanisms hold particular appeal for two key reasons:

1. can enhance the selectivity or specificity of a plasmonic catalyst by enabling reaction pathways that are typically inaccessible through thermal means
2. have the potential to increase catalyst activity and accelerate chemical reactions at milder temperatures, mitigating undesired effects like catalyst or chemical degradation and loss of selectivity [33].

Plasmonic nanoparticles, semiconductor oxides, chalcogenides, metal-organic frameworks, and other carbon-based materials like graphene or carbon nanotubes (CNTs) can exhibit photo-thermal performance [8].

2.4 Semiconductors as photocatalysts

Semiconductors are appealing materials for light-harvesting applications due to their energy band gap, an energy range devoid of normally available electronic states, which aligns with the energy range of visible light. In semiconductors, the valence band (VB) contains states occupied by electrons in the ground state, while the conduction band (CB) consists of unoccupied states at $T = 0\,K$. At higher temperatures, some electrons

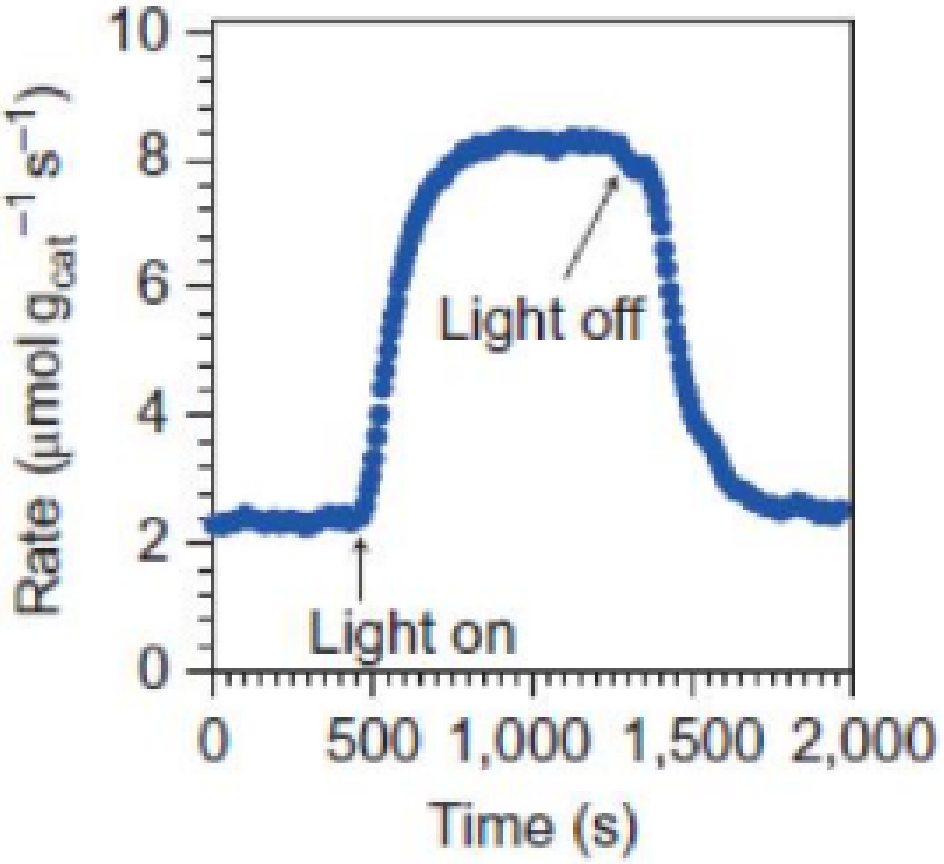

Figure 2.6. Photo-thermo catalysis [6].

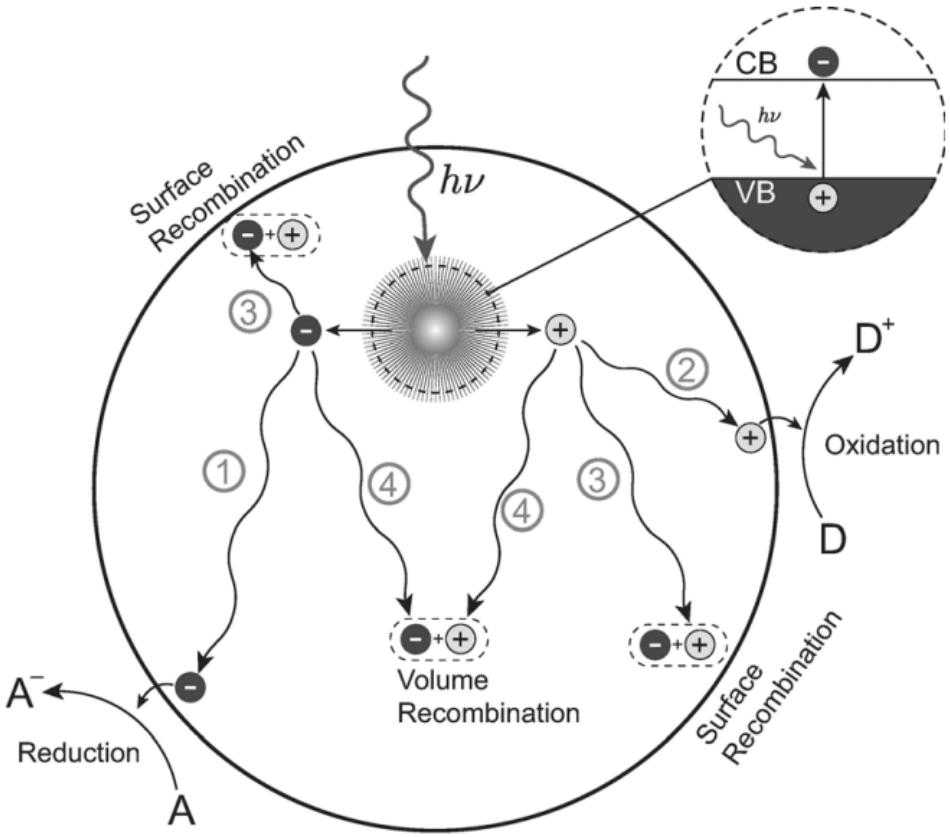

Figure 2.7. Photoinduced formation of an electron–hole pair in a semiconductor with possible decay paths [7]. Note: A=electron acceptor, D=electron donor.

are thermally excited to the CB, and the resulting electron-density distribution is characterized by the Fermi level of the semiconductor. Upon absorbing a photon with energy equal to or greater than the band gap, an electron is excited from the VB to the CB, creating a quasiparticle called a hole in the process. Illumination of a semiconductor leads to larger populations of both charge carriers (electrons and holes) compared to equilibrium, with the new steady state described by quasi-Fermi levels. When spatially separated, these carriers can migrate to the photocatalyst's surface and transfer to adsorbed acceptor molecules, initiating reduction or oxidation processes. The actual reaction sites may be on the semiconductor's surface or indirectly across the interface at the surface of another semiconductor or metal nanoparticle, often referred to as the co-catalyst. In photocatalysis, the semiconductor's primary role is to absorb incident photons, generate electron–hole pairs, and facilitate their separation and transport. Catalysis of the reaction is typically performed by a different material. The process involves band-gap excitation and the formation of free charge carriers , followed by several pathways of de-excitation (Figure 2.7). The efficiency of these processes significantly influences the overall performance of semiconductor-based photocatalysis.

The successful donation of the carrier to the acceptor molecules at the surface, which leads to the desired redox reactions (pathways 1 and 2), faces competition from various recombination processes. Carriers can recombine with their counterparts of opposite charge trapped on the surface (pathway 3), or the recombination of two carriers can occur in the bulk of the semiconductor (pathway 4), known as volume recombination. Recombination processes are detrimental to the photocatalytic reaction efficiency, and their rates are influenced by factors such as mobility and trapping of charge carriers, defect density in the semiconductor lattice, or the presence of an interface with a secondary material acting as electron or hole sinks. When metal nanoparticles are supported on the semiconductor, the photogenerated electrons are accepted by the metal because its available states lie energetically below the CB states of the semiconductor. This upward

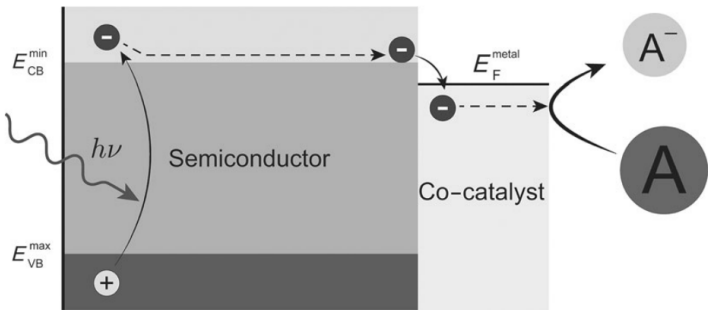

Figure 2.8. Transfer of a photogenerated electron from a semiconductor to the acceptor molecule via the metal co-catalyst [7].

shift in the Fermi level of the semiconductor–metal composite makes its potential more negative, so that the electrons can be shuttled to the adsorbate and be discharged more easily than by the semiconductor itself, that is, the composite is more reductive (Figure 2.8).

A Schottky barrier is formed at the interface, with electrons transferring into the metal while holes remain in the semiconductor. This phenomenon leads to three main advantages: enhanced charge separation, reduced recombination rates, and improved process efficiency. The back-transfer of charge carriers from the adsorbed molecules to the semiconductor is another process that is able to further decrease the photocatalytic efficiency. Before the recombination a carrier can migrate an average distance equal to the diffusion length, which is a material-dependent parameter. Nanostructured materials, particularly nanoparticles, are highly effective in reducing recombination rates due to their high surface-to-volume ratios. The short distances to the surface increase the probability of photogenerated charges reaching the interface without recombination. Additionally, these materials provide large reactive surfaces for interactions with adsorbate molecules, further enhancing their effectiveness in photocatalysis. The reduction potential of an acceptor molecule and the oxidation potential of an oxidized molecule govern the thermodynamic feasibility of charge transfer. The ability of a semiconductor to transfer photogenerated charge carriers to adsorbed molecules hinges on aligning the quasi-Fermi levels of electrons and holes with the redox potential of the adsorbed species. Practically, quasi-Fermi levels are approximated near the band edges, especially for n-type semiconductors such as ZnO, dictating reaction conditions (Figure 2.9). To achieve reduction, the conduction band edge of the semiconductor must be positioned above the LUMO of the acceptor molecule. In terms of redox potentials, this means that the conduction band's potential level must be more negative than the acceptor's reduction potential (the redox potential scale goes from positive to negative with increasing energy). Conversely, in the case of oxidation, a photogenerated hole is transferred from the semiconductor to an adsorbed molecule, which is equivalent to the transfer of an electron in the opposite direction. For this transfer to occur, the donor molecule's HOMO must lie above the valence band edge of the semiconductor. In terms of redox potentials, this means that the potential of the donor must be more negative than the potential level of the valence band.

It has to be pointed out that even electrons excited by highly energetic photons (hot electrons) relax on a femtosecond time scale to lower states in the conduction band or intraband trap states before they reach the surface, without providing a higher reduction potential. Because of these thermodynamic considerations the choice of a suitable photocatalyst involves balancing between:

- efficient light absorption (visible range, small band gap)
- the ability to drive redox reactions (alignment of band edges with redox potentials)

Kinetics-wise, providing substantial overpotentials on each side of the relevant redox potentials and so the precise position of the band gap edges is crucial to ensure the feasibility of charge transfer processes, that is, the range of potentials should not only be spanned, but there should be substantial margins on each side

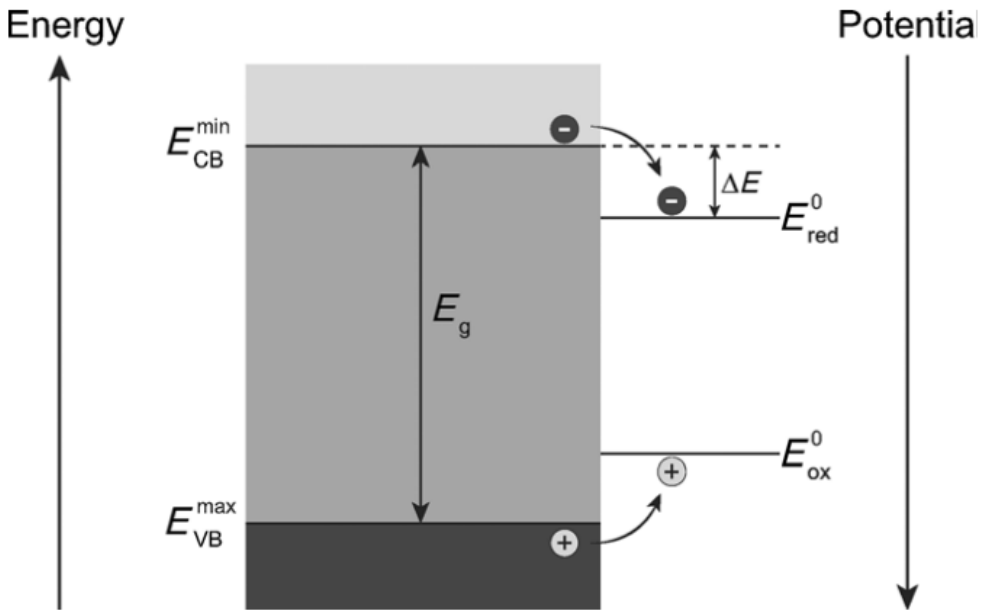

Figure 2.9. Thermodynamic constraints on the transfer of charge carriers to the adsorbed molecules [7]. Note: ΔE=kinetic overpotential of the reduction process.

(Figure 2.9). Without an overpotential, even a proficient catalyst may not yield a high reaction rate [7]. The quest for new semiconductor materials focuses on four main points [7]:

1. raising the valence band energy to decrease the band gap;
2. moving the conduction band to more reductive potentials;
3. improving the quantum efficiency of exciton formation and reducing charge recombination;
4. provide a large surface area with multiple photocatalytic active sites using novel nanoscale morphologies.

2.5 Localized surface plasmon resonance

The localized surface plasmon resonance (LSPR) band observed in metallic nanoparticles (NPs) represents a strong and broad absorption band spanning the UV-visible-NIR region of the electromagnetic spectrum. The underlying physics of this phenomenon has conventionally been elucidated through two main theories:

1. the Drude–Maxwell model
2. the theory formulated by Gustav Mie in 1908.

According to these theories, within metal nanoparticles, conducting free electrons are capable of movement when influenced by external incident irradiation. However, this motion is dampened by electron inelastic collisions, and a restoring force acts on the electron cloud due to the accumulation of surface charges 2.10.

Under resonant conditions, both the incident electromagnetic wave and the resonant frequency of conduction electrons are in phase, maximizing the electric field in so-called ”hot spots” on the surface of plasmonic nanoparticles. Besides the enhanced electric field, additional pertinent properties of LSPR arise from various relaxation processes within plasmonic structures. After excitation, the energy stored in surface plasmons can decay through different pathways:

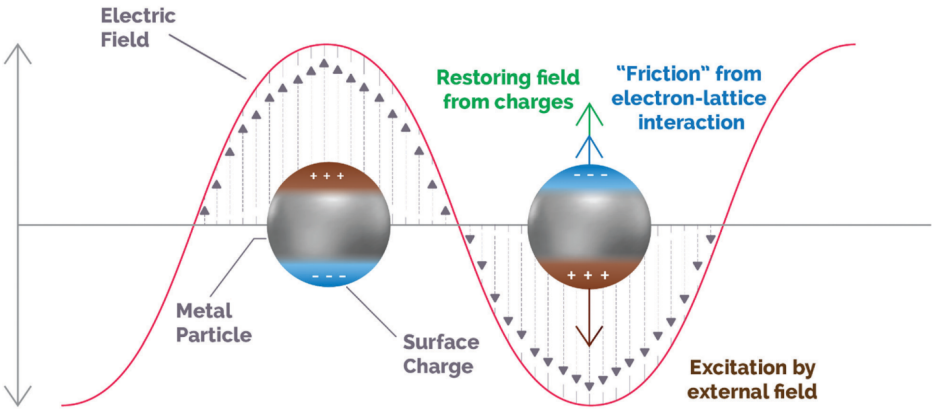

Figure 2.10. Schematic illustration depicting the dynamics of an excited plasmonic nanoparticle. The movement of carriers mirrors the alterations induced by the incoming electromagnetic field (brown), with a restoring force originating from out-of-equilibrium surface charges (green). Additionally, damping occurs due to electronic collisions within the ionic network (blue) [8].

- Non-radiative decay (electron–hole pair excitations and electron–electron collisions)
- Radiative decay (re-emitted photons)

While non-radiative losses may be considered a drawback for specific applications, they hold potential scientific and technological significance. For example, non-radiative decay can lead to local heating (what is called plasmon-induced heating effect), as electronic kinetic energy is transferred to metal lattice phonons. Although photo-thermal cancer therapy has traditionally harnessed this phenomenon, recent years have seen the application of the plasmon-induced heating effect in various research fields, including environmental remediation, solar steam generation and catalytic processes. Moreover, plasmon energy can be non-radiatively dissipated through absorption within the metal nanoparticles, eventually generating energetic hot charge carriers in the plasmonic structure. This contribution to plasmon dephasing stems from electronic collisions with the surface of the plasmonic structure, known as 'Landau damping,' representing a pure quantum mechanical process. In this process, the energy from a plasmon quantum is transferred, on the timescale of femtoseconds (1–100 fs), into a single electron–hole pair excitation. This phenomenon results from the non-conservation of linear momentum of electrons near the surface and in hot spots, enabling an electron to absorb a photon quantum with energy $\hbar w$. Hot carriers have the ability to escape from the plasmonic NPs and initiate further chemical reactions. The concept of plasmon-enhanced catalysis results from the synergistic combination of three properties arising from LSPR:

1. hot carrier generation (photochemical effect)
2. local heating effect (thermal effect)
3. optical near-field enhancement.

In the context of photo-thermal catalysis, from previous researches it was determined that hot carriers and the thermal effect work synergistically to enhance the overall reaction rate. Both mechanisms contribute to varying degrees depending on the operating system. So for plasmonic materials the photo-thermal effect stems from the combined thermal and photochemical contributions of non-radiative plasmon decay [8].

2.6 Photochemical enhancement in plasmonic structures

The excitation of plasmonic nanoparticles can generate hot carriers, comprising electrons and holes, through electronic intraband and/or interband transitions via non-radiative Landau damping. This process involves

the absorption of a photon with energy $h\nu$, leading to the promotion of hot electrons with energies above the Fermi level ($E_F + h\nu$). Upon interaction with other species possessing electron-accepting orbitals, these hot electrons may be injected from the metal nanoparticle to these species. The kinetic energy of hot electrons, excited during plasmon decay, is transferred to adsorbates, chemically activating them via vibrational or electronic transitions. This activation promotes high-energy electrons to antibonding orbitals of adsorbed molecules, potentially leading to the cleavage of molecular bonds and subsequent chemical transformations. The hot electrons generated can be harnessed for catalytic applications through four main pathways, depending on whether a single-component or a heterostructured plasmonic photocatalyst is involved. The first two pathways involve the interaction of hot electrons from single plasmonic nanoparticles with adsorbates via indirect or direct electron transfer. The last two pathways are associated with interactions between supported plasmonic metal nanostructures and semiconductors, either through an indirect injection mechanism to an acceptor or through the direct promotion of the carrier into the conduction band (CB) [8].

2.6.1 Indirect hot electron transfer into the adsorbate

Hot electrons are initially generated within the metal nanoparticle following plasmon excitation. These hot electrons are subsequently transferred to the lowest unoccupied molecular orbital (LUMO) of the adsorbed species on a metal surface. This process is constrained by energy losses due to electron–electron scattering, as the electron transfer into the adsorbate occurs after the generation of hot carriers. The efficiency of this indirect hot electron transfer exhibits a positive correlation with incident photon energy. Higher energy photons generate more electrons with sufficient potential to be injected into the LUMO of adsorbates. The indirect mechanism for electron transfer has been observed in plasmon-mediated activation of small molecules, such as molecular hydrogen (H_2) and oxygen (O_2). Halas *et al.* [34] demonstrated that hot electrons generated on Au nanoparticles could transfer indirectly to the antibonding orbital of molecular H_2, creating a negatively charged $H_2^{\delta-}$ species. Eventually, electrons transferred back to Au, and H_2 returned to its electronic ground state with accumulated vibrational energy, leading to the ultimate dissociation of H_2. In a similar vein, Linic and co-workers [35] reported plasmon-induced partial oxidation of ethylene using Ag nanocubes. In this study, hot electrons generated on the surface of Ag nanocubes were transferred indirectly to antibonding states of O_2, resulting in the generation of O_2^-. Similar to the H_2 activation case, the accumulated vibrational energy overcame the activation energy barrier, leading to O_2 dissociation [8].

2.6.2 Direct hot electron transfer into the adsorbate

The excitation of LSPR can also result in the direct injection of hot electrons from metal nanoparticles to adsorbates. This plasmon dephasing pathway is attributed to chemical interface damping (CID), originating from the coupling between unoccupied adsorbate states and excited surface plasmons. In the direct transfer mechanism, hot electrons are directly transferred into the hybridized states between the metal nanoparticle and adsorbed molecules. Unlike the indirect mechanism, which occurs after the generation of hot electrons, direct electron transfer takes place simultaneously during the dephasing of the plasmon excitation. Due to this concurrent process, the direct electron transfer mechanism is anticipated to exhibit higher efficiency and fewer energy losses, as it avoids electron–electron scattering. Nevertheless, this alternative pathway for direct electron promotion has a lower probability of occurrence, requiring intense adsorbate/metal interaction for surface orbital hybridization, which is not common in plasmonic photocatalysts. Notably, Linic *et al.* [36],[37] observed that the photodegradation of methylene blue by Ag nanocubes was driven via direct electron transfer. Despite Ag nanocubes exhibiting two plasmon absorption bands centered at 532 and 785 nm, the authors reported a higher degradation yield of methylene blue under irradiation at 785 nm. These results suggested that the longest wavelength, and consequently the lowest in energy, could transfer hot electrons more efficiently, implying a one-step process (direct electron transfer) rather than a two-step pathway (indirect mechanism). According to their hypothesis, a strong hybridization between methylene blue and the Ag interface generated electron-acceptor orbitals (LUMO) centered on methylene blue and electron-donor orbitals (HOMO) centered on Ag. However, for the LSPR decay of Ag to directly generate hot electrons in the electron-acceptor states, the energy gap of the HOMO–LUMO transition had to be resonant with the Ag plasmon band at 785 nm. Under this condition, the Ag LSPR decay facilitated the direct electron

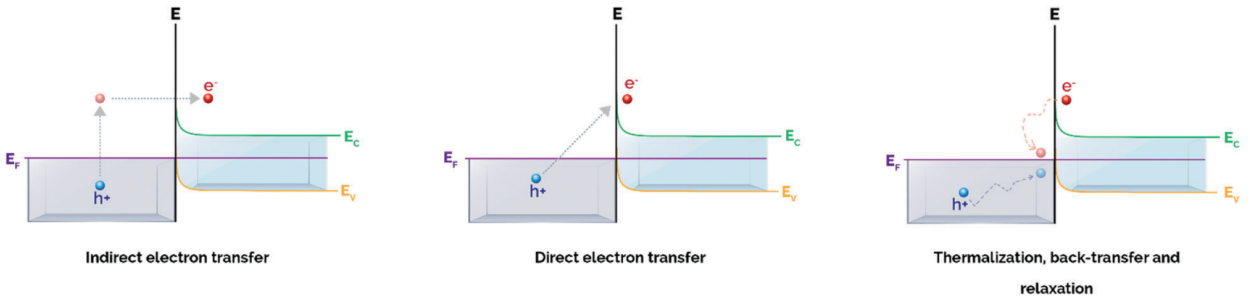

Figure 2.11. Plasmon-induced hot carrier generation and hot electron transfer/back-transfer processes in metal/semiconductor heterostructures [8].

promotion to the excited hybridized states. The outcomes of these studies highlight that the direct electron transfer pathway can serve as a potent strategy for selectively activating reactants, and can be achieved by strategically selecting the wavelength that resonates with the transition between the hybridized states [8].

2.6.3 Indirect hot electron transfer into the semiconductor

The utilization of supported plasmonic nanoparticles as light absorbers has been extensively discussed in photocatalysis. This methodology offers superior solar spectrum harvesting compared to traditional wide bandgap semiconductors. Metallic NPs exhibiting LSPR bands across the visible and infrared regions enable efficient utilization of solar radiation, especially from low-energy wavelengths that may not excite electron-hole pairs in UV-active semiconductor photocatalysts. Additionally, hybrid plasmonic metal-semiconductor structures facilitate spatial separation of photoinduced electron-hole pairs upon electron promotion to the semiconductor, thereby preventing charge carrier recombination within the metal and extending their lifetime. In supported plasmonic NPs, similar to the mechanism observed in non-supported NPs, the prevalent pathway for hot electron transfer in heterostructures involves a two-step process. Initially, hot carriers are generated within the plasmonic nanoparticle on a femtosecond timescale. Subsequently, these hot electrons transfer through the metal-semiconductor interface (Figure 2.11). In the formation of a junction between a semiconductor and a metal nanoparticle, the alignment of Fermi values of both components promotes charge redistribution, establishing equilibrium in the system. This results in the formation of a Schottky barrier at the semiconductor/metal interface, with its energy corresponding to the difference between the Fermi level of the metal and the interfacial conduction band (CB) edge (Figure 2.12). The Schottky barrier plays a crucial role in determining the efficiency of hot electron injection from the metal nanoparticle to the CB of the semiconductor. For catalytic applications, only hot electrons with energies surpassing the energy threshold set by the Schottky barrier inject into the CB and participate in subsequent electron-induced reactions at the semiconductor surface. A low Schottky barrier allows the promotion of a larger number of carriers with energies high enough to traverse the barrier. Simultaneously, a high conduction band bending at the interface prevents back-transfer of electrons to the metal NP (Fig.2.11), ensuring spatial separation of electron-hole pairs and increasing the average lifetime of charge carriers. Striking the right balance between these effects is crucial when designing metal/semiconductor heterojunctions. Typically, the magnitude of the Schottky barrier falls within the range of 0.5 to 1.5 eV, significantly influencing the efficiency of hot electron injection. Importantly, the height of the Schottky barrier is often smaller than the bandgap of many semiconductors, offering a key advantage as excited electrons do not require greater energy than the semiconductor bandgap for extraction. Numerous studies have explored this indirect electron transfer mechanism in metal-semiconductor heterostructures, showcasing its application in various photocatalytic reactions such as water splitting, pollutant degradation and CO_2 reduction [8].

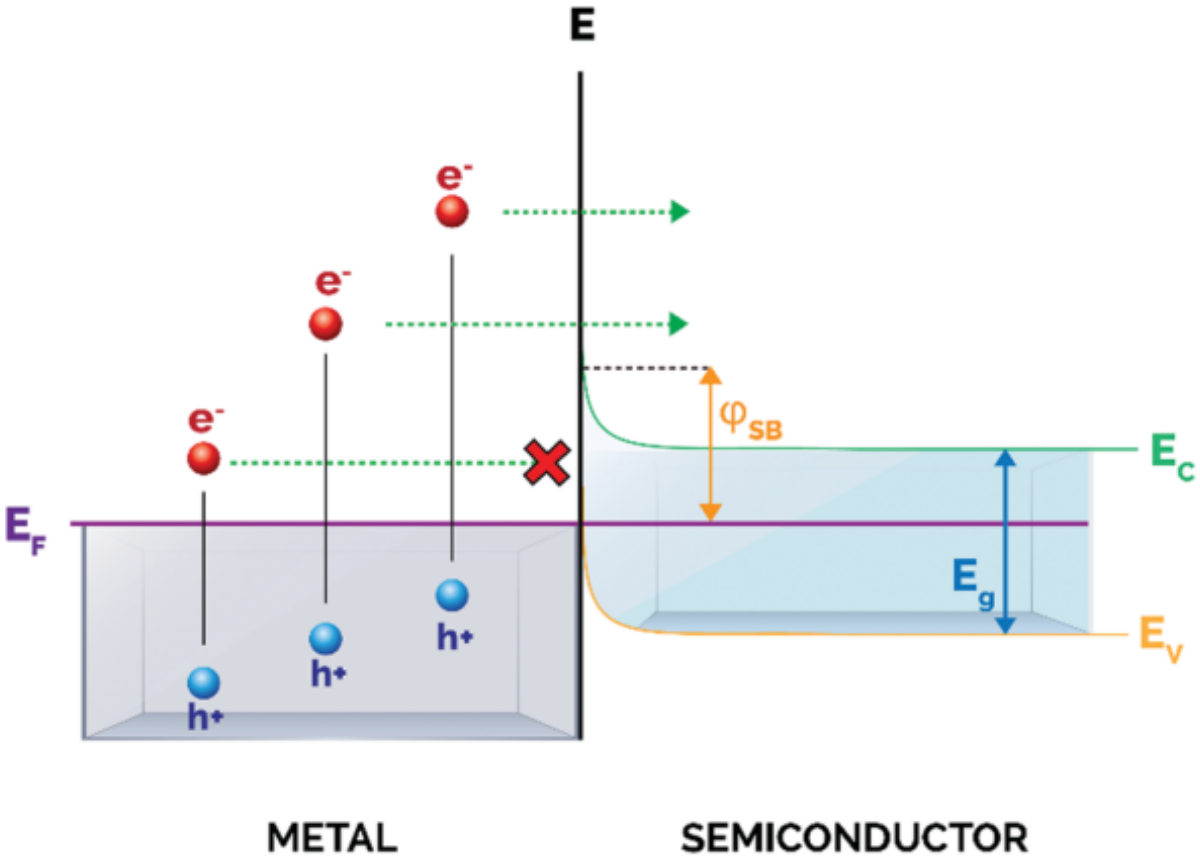

Figure 2.12. Schematic illustration of the metal/semiconductor Schottky barrier: upon excitation, only hot electrons possessing sufficient energy can overcome the Schottky barrier ϕ_{SB} and transition into the conduction band of the semiconductor [8].

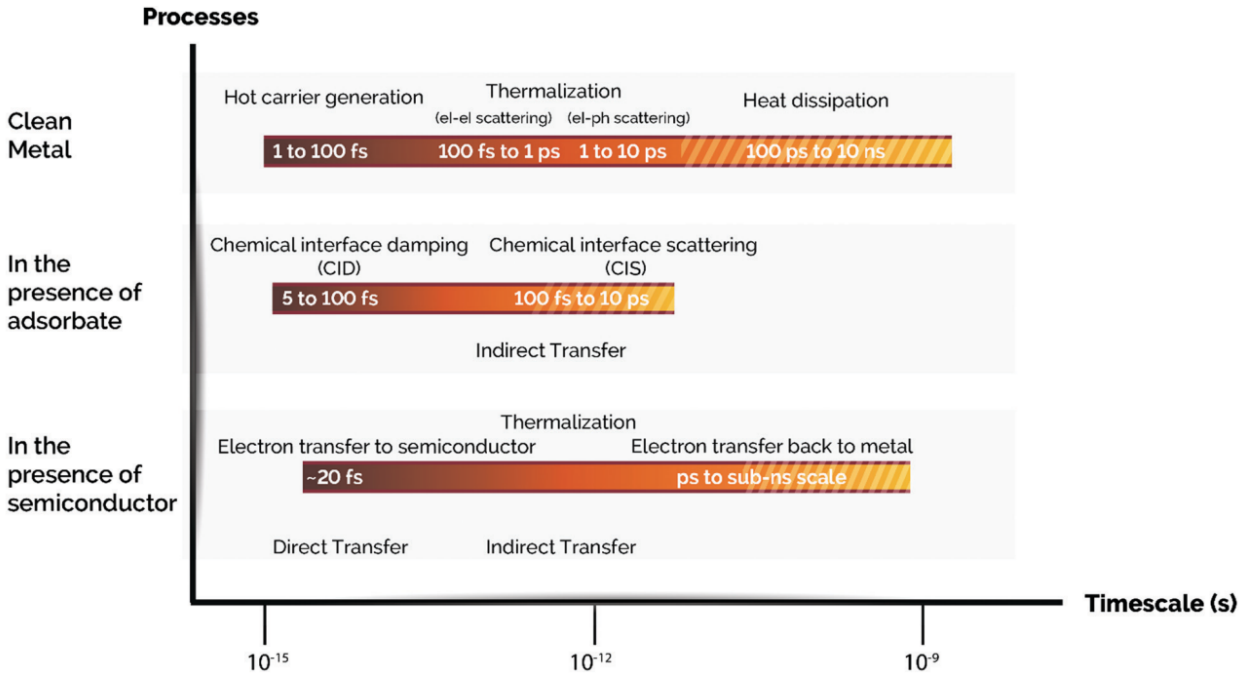

Figure 2.13. Time scales of plasmon-induced hot carrier generation, hot electron transfer, and thermalization processes with/without an adsorbate or a semiconductor [8].

2.6.4 Direct hot electron transfer into the semiconductor

In addition to the previously described indirect electron transfer pathway in metal/semiconductor heterostructures, some studies have proposed the existence of a direct electron transfer mechanism within these hybrid materials (Figure 2.11). While the indirect pathway was initially thought to have a picosecond timescale for electron transfer, experiments in Au/TiO_2 nanostructures revealed a much faster transfer in the order of hundreds of femtoseconds [38]. Moreover, the overall quantum yield (QY) for this direct electron transfer was notably high, reaching up to 40%, compared to the theoretical maximum of below 8% for the indirect pathway [39]. Several investigations have reported ultrafast hot electron injection in plasmonic metal–semiconductor hybrid materials, showing unexpectedly high QYs. This suggests the possibility of a single-step electron transfer involving the direct injection of hot electrons into acceptor orbitals in the semiconductor during plasmon dephasing in metal/semiconductor heterojunctions. This direct pathway is considered more efficient as it avoids energy losses associated with electron–electron and electron–phonon scattering within the metal nanoparticle. Recent studies have observed broadened absorption peaks and fast electron transfer timescales in metal/semiconductor nanocomposites, challenging the traditional understanding of the dominant indirect electron transfer mechanism. Assessing the dominating electron transfer mechanism in these hybrid materials can be challenging, but the study of QY proves to be a valuable tool for distinguishing between different reaction pathways. However, the distinction between direct and indirect electron transfer mechanisms in most current studies of metal/semiconductor heterojunctions is not well-established [8].

2.6.5 Apparent Quantum Yield

The rate of a photoreaction is given by the product of the absorbed photon flux I_a (the number of photons at a given wavelength absorbed per time and volume) and the quantum yield (QY). Since I_a is a function of the intensity of the light source, only the quantum yield, i.e. the rate divided by Ia, is independent of

intensity and can therefore be used to compare the efficiencies of different photoreactions:

$$QY = \frac{\text{rate}}{I_a(\lambda)} \tag{2.1}$$

With the exception of photoinduced chain reactions, the maximum value of the product quantum yield is one, which means that for every quantum of light absorbed by the reacting system, one molecule of product is produced. While it is relatively easy to measure the amount of light absorbed by homogeneous solutions, it is extremely difficult to measure the amount of light absorbed by powder suspensions, such as those commonly used in photocatalysis. This is because the suspended particles of the catalyst not only absorb but also scatter and reflect light. Up to 13 - 76% of the light reaching the powder surface is reported to be lost. To overcome the challenge of quantitatively comparing heterogeneous photoreactions, it has been proposed to replace I_a with a more easily measurable value: the number of photons of a given wavelength per time and volume reaching the inside of a flat front window of the photoreactor (the incident photon flux I_0). The apparent quantum yield (AQY), also known as photonic efficiency, was obtained from this approach:

$$AQY = \zeta_p(\lambda) = \frac{rate}{I_0(\lambda)} \tag{2.2}$$

However, only if the amount of light absorbed is the same in each experiment is it meaningful to compare the resulting values. This is unlikely to be the case, as the amount of scattered and reflected light can vary considerably between experiments. Nevertheless, a comparison seems to be useful when a series of reactions carried out in the same photoreactor are related to a standard system, thus giving "relative photon efficiencies" [40].

2.7 Thermal enhancement in plasmonic structures

The previous paragraphs have delineated the physical mechanisms involved in the photo-thermal catalysis of ultrafast processes, occurring in timescales below 100 femtoseconds (fs) during plasmon decay. In this phase, electron-hole pair excitations take place through Landau damping. As time progresses into longer relaxation periods, hot carriers undergo decay, converting their energy into heat through inelastic coulombic electron-electron scattering over a period from 100 fs to 1 picosecond (ps). Concurrently, low-energy electrons engage with phonon modes through electron-lattice collisions, elevating the temperature of the metal lattice over timescales ranging from several to a few hundred picoseconds. Subsequently, this generated heat is transferred from the metal lattice to the surroundings, occurring between 100 ps and 10 nanoseconds through phonon-phonon scattering (Fig. 2.13). In this context, plasmon-induced heat can facilitate energy transfer from the metal nanoparticle to surface adsorbates, initiating further chemical transformations. This process adheres to an Arrhenius dependence of the reaction rate. It is essential to note that leveraging plasmon heating for chemical reactions is akin to externally heating the system, offering a pathway for controlling product selectivity but not a singular method. Starting from the equation for the local temperature increase (ΔT) caused by the photo-thermal effect in the particular case of a single spherical metal nanoparticle:

$$\Delta T(r) = \frac{V_{NP} Q}{4\pi k_0 r} \tag{2.3}$$

where r is the distance between the center of the NP and the boundary, V_{NP} the volume of the nanoparticle, Q the heat generation and k_0 the thermal conductivity of the medium, is possible to establish the dependence of temperature on the nanoparticle size:

$$\Delta T \propto R_{NP}^2 \tag{2.4}$$

The equation provided establishes a relationship between temperature increase (ΔT) and the square of the nanoparticle radius (R_{NP}^2). This implies that the temperature increase is directly proportional to the square of the nanoparticle radius. In practical terms, it means that as the nanoparticle size increases, the

thermal contribution to the photocatalytic rate is enhanced. However, despite this relationship, it's noted that several experimental and theoretical studies suggest that the thermal contribution to photo-thermal catalysis constitutes only a minority weight in the overall catalytic rate, especially under typical solar irradiance conditions(light intensities similar to continuous-wave solar irradiance, around 100 mW cm^{-2}). This implies that factors beyond the size-dependent thermal effects of nanoparticles play a significant role in determining the overall catalytic efficiency [8].

2.7.1 Collective photothermal effect in plasmonic

However Govorov *et al.*[41] propose the possibility of significant enhancement of the light-induced heating effect when a large number of nanoparticles are present, attributing this enhancement to collective effects. This observation opens up the potential for achieving additional temperature increases through material engineering strategies tailored to exploit these collective effects. In summary, while the conventional view may downplay the importance of light-induced heating, the presence of numerous NPs and specific material design could offer opportunities for substantial temperature boosts [8].

In fact a common misconception in plasmon-driven chemistry found in the literature is that highly localized thermal hotspots will occur at the locations of metal nanoparticles when macroscopic samples are widely illuminated. However illuminating a macroscopic distribution of nanoparticles, especially in 2D or 3D samples, does not lead to the generation of thermal hotspots around each nanoparticle. In fact the utilization of Equation (2.3) provides huge limitations in the calculations of the magnitude of photothermal effects under wide-field illumination because of severe underestimations of the actual sample temperature increase, as it considers only the negligible local temperature increase while neglecting the dominant collective heating. When illuminating an ensemble of nanoparticles in either a 2D layer or a 3D sample (liquid or solid), the absorbance of the sample becomes the most important parameter, rather than the absorption cross section of individual nanoparticles. If the nanoparticle density is sufficiently high, a continuous temperature increase is observed across the entire sample, without nanoscale features. This phenomenon is referred to as the photothermal collective heating or homogenization effect in plasmonics. Despite the optical decoupling of nanoparticles in randomly dispersed plasmonic samples, their thermodynamic behavior is influenced by the number of nanoparticles (N) under illumination. The temperature increase experienced by a nanoparticle is determined by its own heat generation and the heat generated by the other $N-1$ nanoparticles in the sample. For a 2D distribution of nanoparticles, the balance between the local and collective temperature increases can be estimated using the dimensionless number:

$$\zeta_{2D} = \frac{\delta T_{\mathrm{NP}}}{\delta T_{\mathrm{all}}} \tag{2.5}$$

It indicates the ratio between the local and collective temperature increases:

$$\zeta_{2D} \sim \frac{p}{3R\sqrt{N}} = \frac{p^2}{3RL} = (3ARL)^{-1} \tag{2.6}$$

where equation (2.6) has been derived assuming uniform and infinite media above and below the layer through which heat escapes and involves the average nearest-neighbor distance (p), the particle size (R), the number of nanoparticles (N) under illumination, the heated area ($L^2 = p^2N$) and the nanoparticle areal density (A). For a practical calculation of ζ_{2D}, can be considered an example taken from literature [42]. The parameter ζ_{2D} is calculated based on the formula (2.6) with $R = 7nm$, $p = 150nm$ and $L = 1cm$, obtaining as a result: $\zeta_{2D} = \frac{p^2}{3RL} \sim 10^{-4} << 1$. This small value suggests that collective effects dominate the temperature increase in the sample, meaning that the temperature rise of a particular nanoparticle is significantly influenced by the heating contributions from the surrounding nanoparticles, even if they appear optically decoupled. This highlights the importance of considering the collective heating effect when evaluating the temperature increase in plasmonic samples. In fact in scenarios involving the illumination of an

area with only a small number of distributed nanoparticles, localized temperature increases can be observed, but their amplitudes are extremely small. On the contrary, when considering the illumination of a large area, the temperature distribution changes. In this case, two notable features emerge: a uniform temperature without hotspots, signifing that the thermal effects are spread evenly across the entire illuminated area, and a much higher temperature increase, that for the example above (the extimation of ζ_{2D}) was approximately four orders of magnitude higher than the localized scenario. In scenarios where nanoparticles are distributed in three dimensions, the collective thermal effects become even more pronounced. These results underscore the importance of recognizing that thermodynamic laws, particularly the photothermal collective effects in randomly distributed nanoparticle ensembles, differ significantly from the physical laws commonly addressed in plasmonics [33].

2.7.2 Thermocouple measurements

In systems where collective thermal effects result in a smooth temperature profile on the macroscopic scale, employing a simple thermocouple is the most straightforward and reliable method for accurately monitoring the solution's temperature. In fact they are well-suited for measuring temperature in macroscopic three-dimensional samples. However, this approach requires caution to avoid potential issues that might lead to an incorrect estimation of photothermal effects. Firstly, it's crucial to ensure that light does not directly illuminate the thermocouple to prevent direct heating. Secondly, physical contact between the substrate and a thermocouple may influence local heat dissipation, affecting the reliability of temperature measurements. Finally, the thermocouple should be placed as close as possible to the reactive medium and in good thermal contact with it; otherwise, the temperature increase may be significantly underestimated. Some reported works on heterogeneous catalysis use commercial devices, like the Harrick HVC-MRA-5. In such cases, where the built-in thermocouple is positioned away from the reactive area, the non-uniform temperature increase generated by light-driven plasmonic heating may lead to underestimation of the temperature, especially if the thermocouple is not placed in close proximity to the illuminated region. This issue has been highlighted by the authors themselves [43]. So, in systems where large temperature gradients occur due to the uneven distribution of absorbed optical power, a combination of multiple thermocouple readings and suitable modeling of light propagation and heat dissipation becomes necessary to effectively account for photothermal plasmonic effects [33].

2.8 Photocatalysts

In conclusion, the use of solar-powered catalysis to facilitate bond breaking and formation on the surface of catalysts offers an exciting and sustainable way forward for future chemical synthesis. There is still ample room for improving catalytic efficiency in the field of photo-thermal catalysis [8],[44]. Considering that the photo-thermal effect arises from the combined action of both photochemical and thermochemical pathways, different strategies can be adopted depending on the dominant mechanism. Photocatalysts with strong light absorption, high carrier population, long carrier lifetime and low radiative emission are recommended for enhancement of the photochemical process. In addition to the efficiency of hot electron generation, charge transfer efficiency is a crucial parameter that determines the photochemical contribution to the overall photothermal process. In metal/semiconductor junctions, only high-energy electrons can overcome the Schottky barrier at the metal/semiconductor interface. Therefore, the efficiency of charge transfer depends not only on the energy of hot carriers but also on the height of the Schottky barrier. To enhance charge transfer efficiency in these systems, one possible strategy is to adjust the energy levels of the semiconductor through doping or the formation of vacancies/defects in the structure. The efficiency of hot carrier transfer through the interface is also determined by the spatial organization of the heterostructure or metal loading. Therefore, when designing photo-thermal nanostructures, it is important to consider the synergistic combination of all these parameters. Additionally, research has shown that small NPs can shorten the pathway of hot electrons, thus facilitating their injection to adsorbates. Enhancing the adsorption of intermediate species is a reasonable approach to increase their residence time on the surface of the active site, ultimately increasing the efficiency of hot electron transfer to these species. In addition, to enhance the thermochemical process, materials with high optical absorption, low radiative emission and low thermal transport are recommended, which tend to

increase the temperature of the active sites and hence the catalytic performance. With appropriate materials engineering, both the photochemical and the thermochemical mechanisms can be improved, resulting in an outstanding synergy for the enhancement of the photo-thermal performance in a wide range of chemical processes [8].

3 Chemical pathways

The electron transfer to the adsorbed molecule initiates a complex cascade of chemical reactions in the photocatalytic reduction of carbon dioxide. This multistep process involves up to eight electrons and protons, C-O bond cleavage, and C-H bond formation, leading to various potential products. Enhancing the photocatalytic reduction of CO_2 requires a comprehensive understanding of the chemical mechanism, offering opportunities to increase the overall conversion rate by minimizing thermodynamic or kinetic barriers. Additionally, control over selectivity is crucial for directing the process towards desired products. Despite these challenges, the exact mechanism of CO_2 photoreduction remains to be fully elucidated. Carbon dioxide molecules exhibit stability and chemical inertness with a closed-shell electronic configuration, linear geometry, and $D_{\infty h}$ symmetry. The addition of a single electron induces a bending of the molecular structure due to repulsion between the new electron on the electrophilic carbon atom and the free electron pairs on the oxygen atoms. This increased repulsion, along with the loss of symmetry, contributes to the high energy of the lowest unoccupied molecular orbital (LUMO) of CO_2, resulting in a very low electron affinity for the molecule. The single-electron reduction of CO_2 to an anion radical, $CO^{\bullet -}$ (Equation (3.1)), is characterized by a strongly negative electrochemical potential of -1.90 V versus the normal hydrogen electrode (NHE).

$$CO_2 + e^- \rightleftharpoons CO_2^{\bullet -} \qquad E^0_{\text{redox}} = -1.9V \tag{3.1}$$

Consequently, there is virtually no semiconductor capable of providing sufficient potential to transfer a single photogenerated electron to a free CO_2 molecule (Figure 3.1).

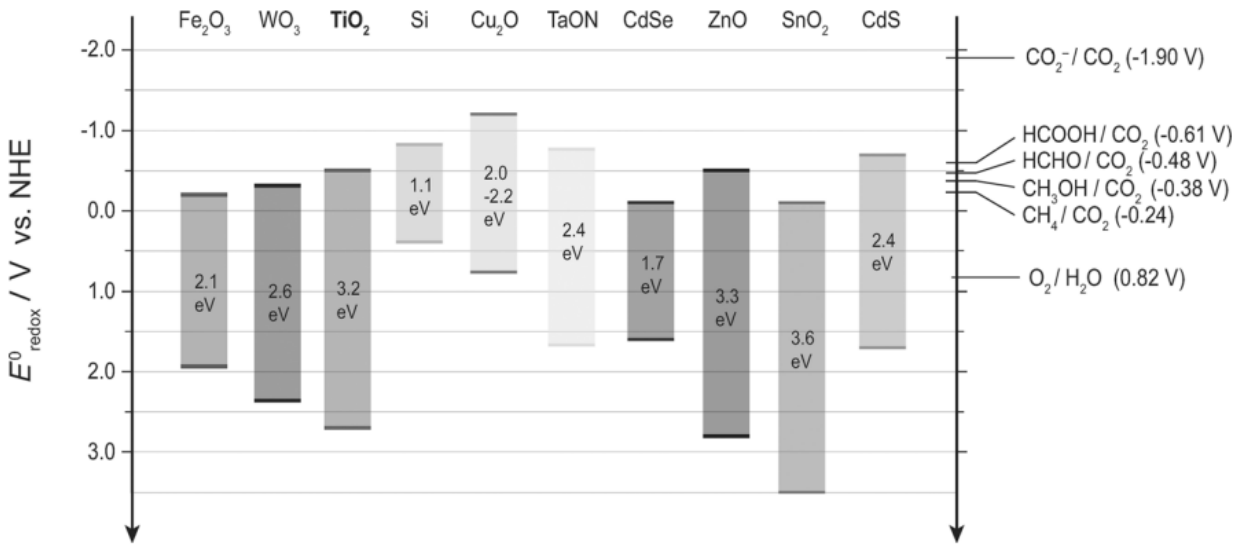

Figure 3.1. Conduction band, valence band potentials, and band gap energies of various semiconductor photocatalysts relative to the redox potentials of compounds involved in CO_2 reduction [7].

This makes the initial step of transferring a single electron to CO_2 highly improbable due to its unfavorable energy requirements. The feasibility of the photocatalytic reduction of carbon dioxide involves a proton-assisted multi-electron transfer processes. The electrochemical potentials for CO_2 reduction to various products are listed below, considering the transfer of two to eight electrons and an equivalent number of protons.

$$CO_2 + 2\,H^+ + 2\,e^- \rightleftharpoons HCOOH \qquad E^0_{\text{redox}} = -0.61\text{V} \tag{3.2}$$

$$CO_2 + 2\,H^+ + 2\,e^- \rightleftharpoons CO + H_2O \qquad E^0_{redox} = -0.53V \tag{3.3}$$

$$CO_2 + 4\,H^+ + 4\,e^- \rightleftharpoons HCHO + H_2O \qquad E^0_{redox} = -0.48V \tag{3.4}$$

$$CO_2 + 6\,H^+ + 6\,e^- \rightleftharpoons CH_3OH + H_2O \qquad E^0_{redox} = -0.38V \tag{3.5}$$

$$CO_2 + 8\,H^+ + 8\,e^- \rightleftharpoons CH_4 + H_2O \qquad E^0_{redox} = -0.24V \tag{3.6}$$

The values are comparable to proton reduction itself (Equation (3.7)), although the latter is a one-electron process.

$$2\,H^+ + 2\,e^- \rightleftharpoons H_2 \qquad E^0_{redox} = -0.41V \tag{3.7}$$

While multi-electron transfer processes are theoretically possible, the potentials are less negative than the conduction band of many semiconductors (Figure 3.1, there is limited evidence in the literature, indicating that the reaction may proceed through a series of one-electron steps. The initial electron transfer step remains a significant obstacle to the photoreduction of CO_2 and is likely a limiting step. The activation of CO_2 on semiconductor surfaces involves adsorption, leading to the formation of the partially charged species ${CO_2}^{\delta\bullet-}$. This adsorbate, exhibiting lower symmetry than free CO_2, has a reduced barrier for accepting an electron (the LUMO level decreases as the molecule bends). Then the reduction process follows a sequence of elementary steps, each of them including the transfer of an electron, a proton, or a hydrogen radical ($H^\bullet$), along with the breaking of C-O bonds and the formation of new C-H bonds. Numerous intermediates in the form of radical species are generated throughout these steps, and their recombination at various stages contributes to the diversity of possible pathways and final products. The precise order and mechanistic details of each subsequent step in the reduction process are not yet fully elucidated. Metal nanoparticles, often used as co-catalysts, play a crucial role in enhancing charge separation and catalyzing subsequent steps of CO_2 reduction [7]. The formation of the bent anion radical $CO^{\bullet-}$ was initially observed in a Rh/TiO_2 composite, where the transfer of an electron from the metal d orbital to the (C-O) p* orbital was proposed as the mechanism [45]. However, the role of metal NPs in the chemical mechanism of CO_2 reduction extends beyond its activation, they also function as catalysts in the subsequent steps of the reduction, significantly influencing the overall selectivity of the process [7].

4 Reverse water-gas shift reaction

The RWGS reaction (Equation (4.1)) involves the reversible hydrogenation of CO_2 to generate CO and H_2O. Due to the chemical stability of CO_2, it is a relatively unreactive molecule, making the conversion to the more reactive CO an energy-intensive process.

$$CO_2 + H_2 \rightleftharpoons CO + H_2O \qquad \Delta H_{298K} = +42.1\,\mathrm{kJ\,mol^{-1}} \tag{4.1}$$

Due to the considerable stability of CO_2 as a molecule, a substantial amount of energy is required for its conversion [9]. Thermodynamic assessments conducted at atmospheric pressure reveal that the conversion is heightened when there is an excess flow of H_2 [46] and, in accordance with Le Châtelier's principle, the reaction's endothermic nature causes its thermodynamic favorability at higher temperatures. Consequently, at lower temperatures, the equilibrium tends to increasingly favor the Water-Gas Shift (WGS) reaction (the reverse of Equation (4.1)), methanation (Equation (4.2)) and Sabatier Reaction (4.3) as they are exothermic and prominent side reactions under these conditions. Moreover products separation can shift the equilibrium towards the products [46].

$$CO + 3\,H_2 \rightleftharpoons CH_4 + H_2O \qquad \Delta H_{298K} = -206.5\,\mathrm{kJ\,mol^{-1}} \tag{4.2}$$

$$CO_2 + 4\,H_2 \rightleftharpoons CH_4 + 2\,H_2O \qquad \Delta H_{298K} = -165.0\,\mathrm{kJ\,mol^{-1}} \tag{4.3}$$

The equilibrium composition, illustrated in Figure 4.1 for a molar H_2/CO_2 inlet ratio of three across a temperature range of 100 to 1000 °C, indicates that at lower temperatures (< 600 °C), methanation is favored by thermodynamics. Conversely, at temperatures exceeding 700 °C, the formation of methane becomes negligible, and the primary product is CO. Nonetheless, efforts are made to maintain the temperature as low as possible to minimize energy losses and capital costs[9].

It is essential, however, to ensure that the chosen H_2/CO_2 ratio and temperature are within practical limits for economical and industrial applicability. Altering pressure does not significantly impact reaction activity and equilibrium position due to the reaction's stoichiometry.

The RWGS reaction serves as a desirable pathway for industrial applications, often employed in conjunction with the Fischer-Tropsch (FT) reaction to produce hydrocarbon fuels from syngas. It typically operates within the temperature range of 200–375 °C, with lower temperatures favoring the production of long-chain alkanes and higher temperatures favoring shorter ones. It is essential to consider that the thermodynamics of the RWGS reaction inherently demand higher temperatures to achieve acceptable levels of activity. Hence, enhancing catalytic activity for the RWGS reaction at lower temperatures becomes crucial to reduce the heat requirements for the FT process [47]. Mallapragada *et al.* [48] compared various methods of transforming CO_2 into liquid fuels using solar-assisted processes and H_2 provided by electrolysis. The methods investigated included biomass gasification, RWGS, algae-derived oils, and direct photosynthesis. The conversion of CO_2 to CO by reverse water gas shift reaction followed by CO conversion to fuels with FT had the highest current and estimated potential efficiency when CO_2 is captured from a flue gas or from the atmosphere. Moreover, converting CO_2 to CO provides additional versatility in the products that can be obtained from CO transformation. The RWGS reaction is also of great interest for space exploration due to the high (approximately 95%) atmospheric CO_2 concentration on Mars and the availability of H_2 as a byproduct of oxygen generation. Therefore, the RWGS reaction is a promising process, with products that have a wide variety of potential end uses [46].

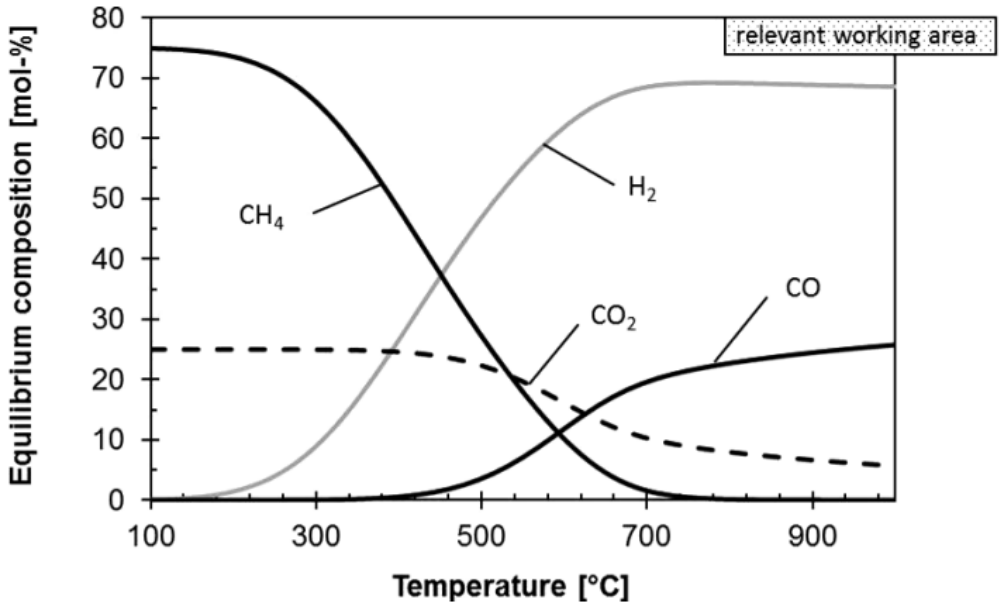

Figure 4.1. Thermodynamic equilibrium composition of the product gas of RWGS reaction at 1 bar for a molar H_2/CO_2 inlet ratio of 3 [9].

4.1 Hydrogen production using renewable energies

As it is outlined above, various products can be produced from carbon dioxide and hydrogen: syngas, methanol, dimethyl ether (DME), methane, formic acid, and short-chain olefins. The focus is on the utilization of hydrogen generated directly from renewable energy sources (r-H_2), acting as a key element in connecting renewable energy with basic chemicals production, based on the production of hydrogen using renewable energy electrolyzers and proton exchange membrane (PEM) cells, or solid-state high-temperature electrolyzers.

Recent papers mention alternative approaches to produce r-H_2 apart from electrolysis. These include:

1. Biological production (bio-H_2): utilizing cyanobacteria and other bacteria
2. Photocatalysis
3. Hydrogen from biomass
4. Microbial electrolysis
5. Wind power
6. Solar energy

All these approaches are currently under active research, and their maturity, greenhouse gas (GHG) impact, and associated costs are crucial factors to consider when evaluating the integration of renewable energy into energy or production chains through CO_2 recycling [49],[50].

4.1.1 Greenhousegases impact of hydrogen production routes from renewable energy

Hydrogen from renewable energy sources may be produced from biomass-derived products through different methods, such as aqueous phase catalytic reforming or thermocatalytic approaches. However, the cultivation of biomasses significantly affects greenhouse gases emissions, coupled with substantial energy consumption

in harvesting, transport, and processing. Consequently, the net impact on GHG emissions per mole of H_2 remains considerable, albeit lower than that from fossil fuels. Currently, methane steam reforming serves as the primary commercial method for H_2 production, yielding four moles of H_2 per mole of CO_2, equivalent to approximately 5.5 kg of CO_2 per kg of H_2. When considering the life-cycle perspective, this value increases to about 8.9 kg of CO_2 per kg of H_2. To address this, a focus on hydrogen-producing methods directly utilizing renewable energy (RE) sources is deemed more appropriate. For H_2 production using direct RE sources, the established approach involves generating electrical energy through photovoltaic panels, wind turbines, or similar alternatives (e.g., geothermal, waves) and subsequently employing an electrolyzer. Although life cycle assessment (LCA) data are not entirely reliable due to ongoing technological developments, estimates for wind/electrolysis suggest emissions below 1 kg of CO_2 per kg of H_2. Other studies indicate varying values, with H_2 from hydroelectric/electrolysis or solar thermal conversions estimated at around 2 kg of CO_2 per kg of H_2. Older photovoltaic (PV)/electrolysis combinations were reported at higher values (approximately 6 kg of CO_2 per kg of H_2), but recent advancements in PV technology warrant a more conservative estimate of 1–2 kg of CO_2 per kg of H_2.

While detailed comparisons are limited, it is tentatively suggested that direct routes for producing renewable hydrogen (r-H_2) contribute to CO_2 emissions approximately one-third of those associated with biomass conversion routes and about one-fifth of emissions from current H_2 production methods. Considering the pivotal role of H_2 production in the entire process of converting CO_2 to chemicals through hydrogenation, it becomes evident that direct methodologies utilizing RE for H_2 production are preferable over those relying on biomass to integrate renewable energy into the chemical production chain[50].

5 Hi-fuel catalyst

Highly efficient photocatalytic systems often involve coupling semiconductors with metal nanoparticles. This coupling enhances the performance of the photocatalyst by improving charge separation, facilitating CO2 activation and providing active catalytic sites for the reduction process. Surface decoration or wet impregnation of the nanostructured semiconductor with metal or metal oxide nanoparticles is typically used in this approach [7].

The $Cu/ZnO/Al_2O_3$ (CZA) catalyst is widely used in industry and has high activity for methanol production, both in terms of turnover frequency, based on Cu active sites, and MeOH yield. The industrial CZA catalyst components, which include semiconducting materials such as ZnO, Cu_2O and CuO, and potentially plasmonic Cu, suggest that catalytic performance could be enhanced by simultaneous thermal and light activation [1]. For the purpose of this study, this catalyst was used for the production of carbon monoxide and the loading was as follows: Cu 50%, ZnO 30%, and Al_2O_3 20%.

The use of noble metals is associated with significant costs. Abundant and cost-effective materials have been investigated to replace noble plasmonic metals (e.g. Au, Ag, Pd, Pt) in photothermocatalytic reactions [8]. The use of Cu for RWGS provides two major advantages: it has been shown to perform RWGS at low temperatures (down to 165°C) and little or no methane is produced as a by-product [46].

Zinc oxide is an important metal oxide because of its distinctive physical properties: a wide and direct band gap of about 3.37 eV, a large exciton binding energy of 60 meV, and an exciton Bohr radius of about 2.34 nm [51],[21]. It can promote the chemisorption of carbon dioxide and enhance the electronic interaction within the copper component. While Al_2O_3 improves the surface area of Cu/ZnO nanoparticles, acting as a substrate for their growth and dispersion in the catalyst [52].

As reported by Xie *et al.*, Cu nanoparticles are surrounded by smaller ZnO nanoparticles and the isolated entity are well dispersed within the Al_2O_3 carrier. After the reaction, the ZnO nanoparticles become highly aggregated and interconnected with small-sized Cu species, which supports the dynamic properties of the particles and the migration of ZnO to the Cu surface under the reaction conditions. The benefits of CZA are due to the unique promotion of ZnO in the stabilisation of intermediates involved in CO_2 hydrogenation over the Cu-ZnO system. In fact recent studies on Cu-ZnO catalysts have suggested that the Cu-ZnO interface can provide active sites for the reaction of a number of species or intermediates. Furthermore, a strong metal-support interaction (SMSI) between Cu and ZnO was identified as crucial in creating and maintaining Cu(I) active sites on the surface. This stabilises oxygenates in close proximity to Cu(I). ZnO can act as a structure modifier, hydrogen storage or direct promoter of bond activation [53],[1].

The significance of such complex catalytic systems, involving multiple catalyst components and products, lies in the synergistic effects of different photo-activation modes. The excitations linked to particular components of CZA, such as the ZnO band gap excitation (3.2 eV, $\sim$ 388nm), and Cu LSPR ($\sim$ 590nm), alter the electron population state of the catalyst, thereby regulating intermediate reactions and product distribution. The effects of band gap excitations associated with the Cu_2O and CuO components (2.2 eV and 1.7 eV, respectively) are negligible due to their limited presence after reduction. Furthermore, when Cu and ZnO are simultaneously photoexcited, the absorbed photon energy (visible light) can be trapped inside the metal nanostructure via the Cu LSPR, leading to local heating of the Cu metal lattice environment, which may contribute to the CO_2 hydrogenation reaction. However, deactivation of the CZA catalyst is one of its main drawbacks, caused by the water produced during the RWGS reaction. The presence of water causes agglomeration in the ZnO phase, resulting in a reduction of the interfacial contact area between the ZnO and Cu components [1].

6 Reaction mechanism

The reaction mechanisms and the interplay between the surface properties of the catalyst and the feed gases are still subject of debate. The effect of the so-called "Cu-ZnO synergy" is also controversial, as it is either considered to have no unique role, to be merely a structural promoter, or to be essential for the active site [54],[55]. Two mechanisms have been proposed for the reaction: a surface redox mechanism and a surface formate decomposition mechanism [10].

6.1 Surface redox mechanism

According to the surface redox mechanism, also known as the oxygen adatom mechanism, $CO_2 + H_2 \rightleftharpoons CO + H_2O$ is a sequential process whose first step is the decomposition of carbon dioxide on the copper surface. This results in adsorbed carbon monoxide and surface oxygen species, the latter of which are then scavenged by hydrogen in the gas phase.

$$CO_2 \rightleftharpoons CO^* + O^* \tag{6.1}$$

$$CO^* \rightleftharpoons CO \tag{6.2}$$

$$H_2 \rightleftharpoons 2\,H^* \tag{6.3}$$

$$H^* + O^* \rightleftharpoons OH^* \tag{6.4}$$

$$H^* + OH^* \longrightarrow H_2O^* \tag{6.5}$$

$$H_2O^* \rightleftharpoons H_2O \tag{6.6}$$

where "*" indicates adsorbed surface species. This results in CO being produced solely from CO_2 over the Cu nanoparticles. The product of the exposure to CO_2 is a layer of oxygen adatoms. The oxidation state of Cu is influenced by the surface population of O* and H* species, which result from the cleavage of the C=O bond of the CO_2 adsorbate and the dissociation of H_2, respectively. It is still unclear whether the step (6.4) takes place directly as an elementary step or instead via the "water-catalysed" sequence:

$$H_2O^* + O^* \rightleftharpoons 2\,OH^* \tag{6.7}$$

$$H^* + OH^* \rightleftharpoons H_2O^* \tag{6.8}$$

The reduction of the oxygen species takes place at a much faster rate than the oxidation of the catalyst with CO_2 and hydrogen is proposed to be a reduction reagent without direct involvement in the formation of intermediates. The RWGS reaction therefore proceeds via the scheme (6.1) involving oxidation and reduction of the Cu surface, $Cu(O) \rightleftharpoons Cu(I)$, with CO_2 and H_2, with oxidation with CO_2 being the rate-determining step [10],[56],[57],[58].

6.2 Surface formate decomposition mechanism

However, the above redox mechanism cannot be a complete explanation of the reaction behaviour of RWGS. In fact, CO_2 dissociation at the Cu(0) surface can lead to the formation of CO and oxygen adatoms, but

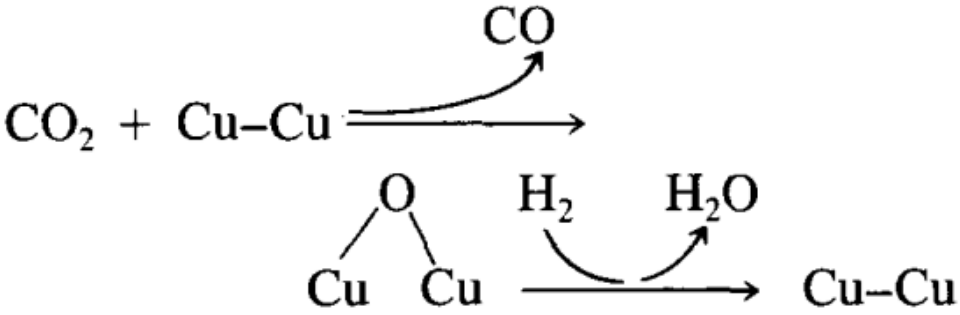

Figure 6.1. Surface redox mechanism [10].

it is not the only source of CO for the RWGS reaction. The formation of CO is strongly dependent on the involvement of hydrogen, the role of which is linked to the adsorption of CO_2 for the formation of reaction intermediates [58]. Xie *et al.* state that the defective ZnO surface, containing vacant oxygen sites with trapped electrons, provides the primary active sites for CO_2 chemisorption in the form of CO_3* (carbonate), HCO_3* (bicarbonate), HCOO* (formate) species. Cu contributes to this process through the promoting effect of the Cu-ZnO interface and the stimulation of H* supply. CO can be formed both on the ZnO surface and on the Cu surface. There are two possible pathways for CO formation:

1. CO forms mainly on the Cu surface by Cu-CO_3* dissociation
2. ZnO-HCOO* decomposes on the ZnO surface (adsorption of CO on ZnO is weak).

Bicarbonate species are converted to formate species due to the presence of hydrogen. The adsorbed reaction intermediates are then decomposed into CO* and OH* intermediates, which are finally desorbed as CO and H_2O. Formate species are reasonably proposed to be the dominant intermediate in the decomposition mechanism and the presence of the chemically bonded $Cu^{\delta+}$-O-ZnO interface is likely to facilitate the formation of formate [1],[54].

6.3 Photo-enhanced hydrogenation mechanism

Plasmon-induced hot electrons are reported to be capable of activating chemical bonds and driving chemical transformations in a well-designed, energetically matched surface-adsorbate configuration. Indeed, the changes in the oxidation state of Cu, the oxygen vacancy levels in ZnO, the weakening of the C=O bond (through electrons transferred to the anti-bonding orbital) and hence the performance of CO_2 hydrogenation are considered to be primarily driven by the excitation and transfer of electrons under irradiation conditions. Excitation of ZnO promotes electron transfer from ZnO to Cu, resulting in additional Cu(I)-O species and contributing to CO production. The hot electrons generated by the plasmon excitation of Cu are responsible for the activation and enhanced cleavage of adsorbed H_2 molecules, triggering Cu(I)-O reduction and oxygen defect formation in ZnO. Excitation of both compounds is likely to result in electron transfer from an excited Cu orbital state to the ZnO conduction band (termed plasmon-mediated electron transfer (PMET)) and electron donation from ZnO to Cu (termed photocatalyst-cocatalyst scheme), as displayed in Figure 6.3. These processes enhance the photocatalytic process and accelerate the formation of gaseous CO [1].

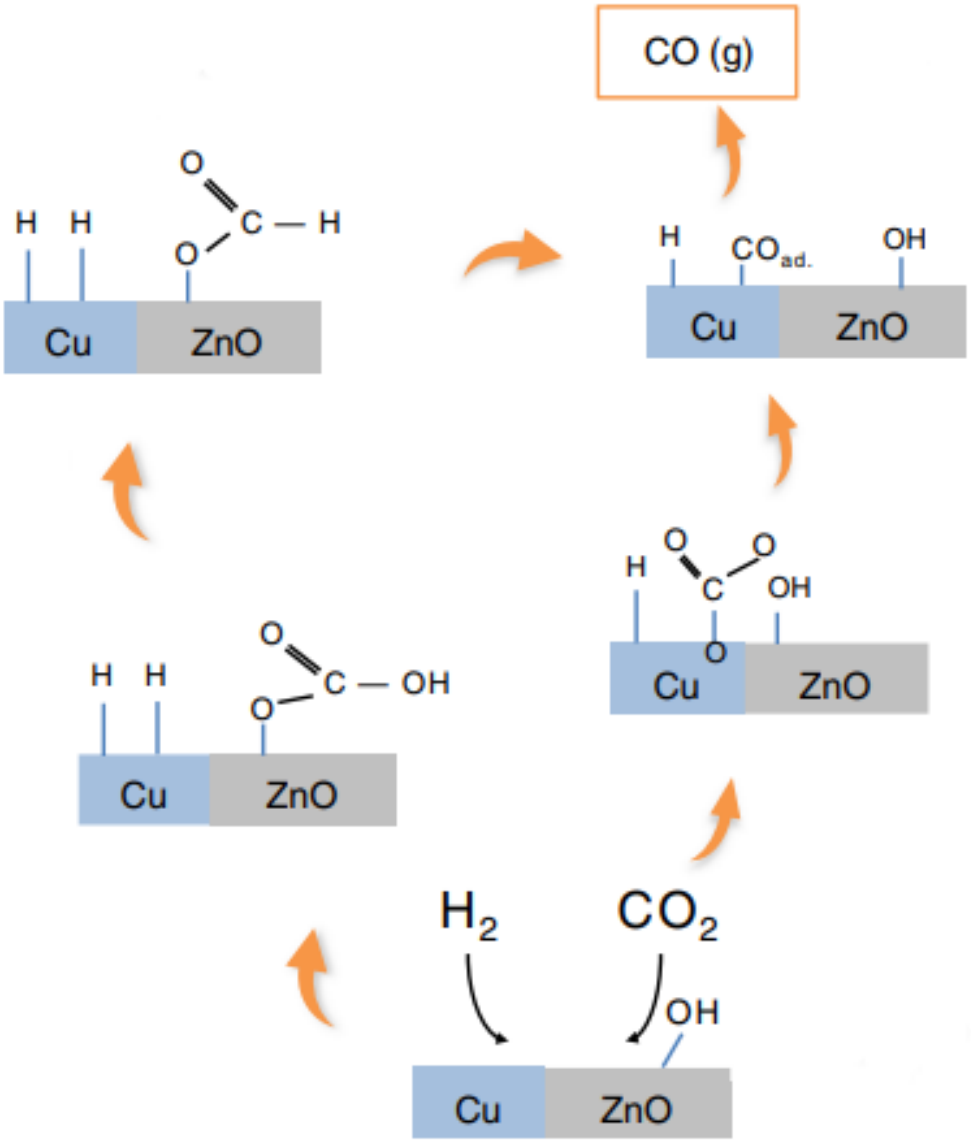

Figure 6.2. CO production pathway over Cu-ZnO catalyst through carbonate and formate decomposition [1].

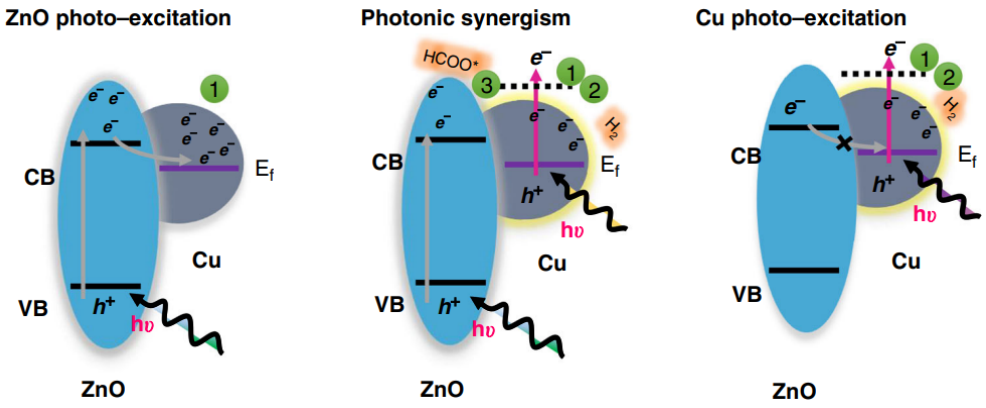

Figure 6.3. Electron transfer between Cu and ZnO [1].

7 Catalyst characterization

7.1 X-ray diffraction spectroscopy (XRD)

X-ray powder diffraction is a non-destructive analytical technique used for both qualitative and quantitative evaluations of pure substances and multi-component mixtures. It requires minimal sample preparation. Crystalline materials exhibit diffraction patterns that reveal their underlying structural and physicochemical properties when exposed to an X-ray beam. Hull in 1919 [59] stated that *"every crystalline substance gives a pattern; the same substance always gives the same pattern; and in a mixture of substances, each produces its pattern independently of the others."* This technique enables the identification of crystal structure, degree of crystallinity, crystallite size and atomic spacing, crystalline phase, transition and their quantitative proportion, microstructure, quantitative resolution of chemic species, isomorphous substitutions, unknown crystalline materials, and solids. X-ray diffraction patterns are commonly used to identify crystalline samples by matching their diffraction patterns to the Inorganic Crystal Structure Database (ICSD). Due to its ability to produce independent patterns of components in mixtures, this analytical technique is widely used in forensics, nanomaterials, geochemical materials, and catalysis. Crystalline materials exhibit a three-dimensional regularity of atoms, forming a crystal structure based on one of the 14 Bravais lattices. When a monochromatic X-ray beam interacts with the surface of a material, the atoms transmit, refract, scatter, or absorb the radiation. Diffraction occurs due to the coherent scattering of the radiation by the solid, which is possible because of the dimensional regularity of unit cells. The direction of the scattered beam is determined by both the interatomic spacing ($d_{\mathbf{hkl}}$) of the plane and the radiation wavelength. The intensity of the scattered beam is influenced by the crystal's orientation relative to the direction of the incident x-ray and the position of each atom within the unit cells. The overlapping of waveforms in scattering can result in either constructive or destructive interference. This leads to reflections that are either allowed with non-zero intensity or disallowed with minimal intensity, respectively. To meet diffraction criteria, the incident radiation wavelength (λ) must be smaller than the distance between scattering sites and the scattering must occur in a coherent way. This requires radiation with a wavelength of less than 0.2 nm to satisfy the diffraction criteria, since the atomic spacing is of the order of the lattice constant (0.2 nm to 0.4 nm). This criterion is only met by X-rays and high energy electrons. For coherent scattering, the energy of the incident radiation must be equal to the energy of the scattered radiation [11].

X-rays are high-energy electromagnetic waves with wavelengths between 10^3 and 10^1 nm. X-ray diffractometers consist of three basic components: an X-ray tube, a sample holder and an X-ray detector [60]. They are typically produced using sealed tubes, rotating anodes or synchrotron radiation sources. Sealed tubes and rotating anodes, both of which are used in laboratory equipment, generate X-rays using the same principle: a tungsten filament is heated in a vacuum to produce electrons. These are then accelerated by a high potential field and directed towards a target [12]. When the electrons have enough energy to eject inner-shell electrons from the target material, characteristic x-ray spectra are emitted, then collimated and directed at the sample. The intensity of the reflected X-rays is registered as the sample and detector are rotated through a range of 2θ angles (Figure 7.1). Constructive interference will occur and an intensity peak will appear if the geometry of the incident X-rays striking the sample obeys Bragg's law [60]:

$$n\lambda = 2d\sin(\theta) \tag{7.1}$$

where n is an integer, d_{hlk} is the interplanar spacing that produces the diffraction, and θ is the angle of incidence of the x-ray [11]. The details of the geometrical conditions for diffraction and the derivation of Bragg's law are shown in Figure 7.2 [12]. This law describes the relationship between the wavelength of the electromagnetic radiation produced, the lattice spacing of the crystalline sample and the angle of diffraction. The position and intensity of the diffraction are linked to the identity and position of the atoms in the unit cell [11].

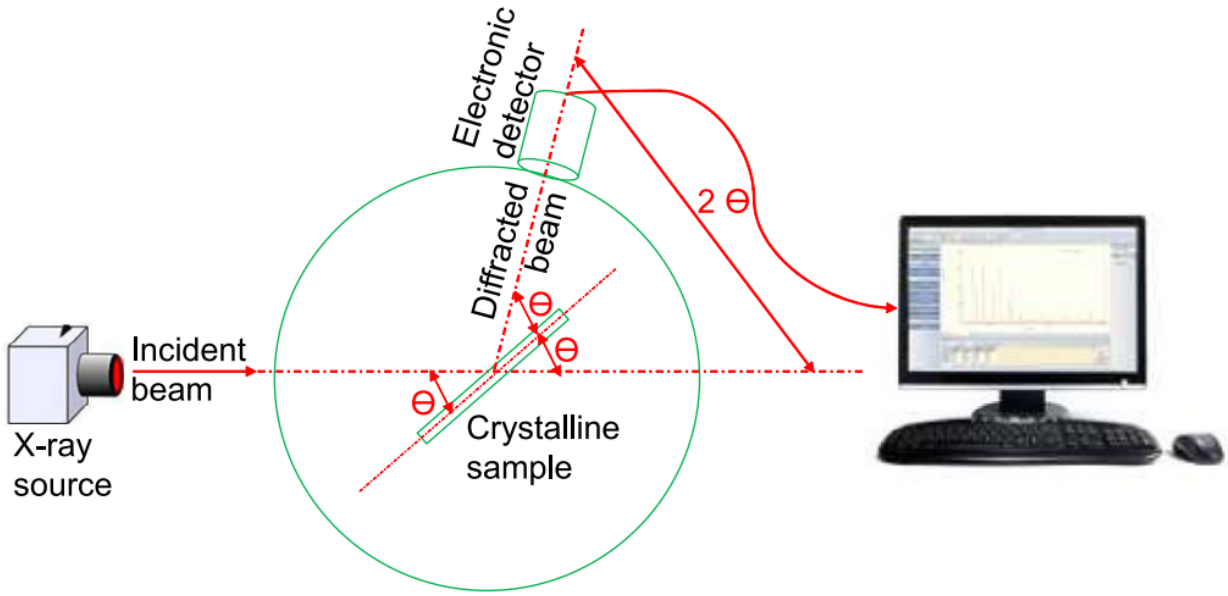

Figure 7.1. XRD instrument schematic. An incident X-ray beam irradiates the surface and a film or electronic detector records the signal as it covers an arc [11].

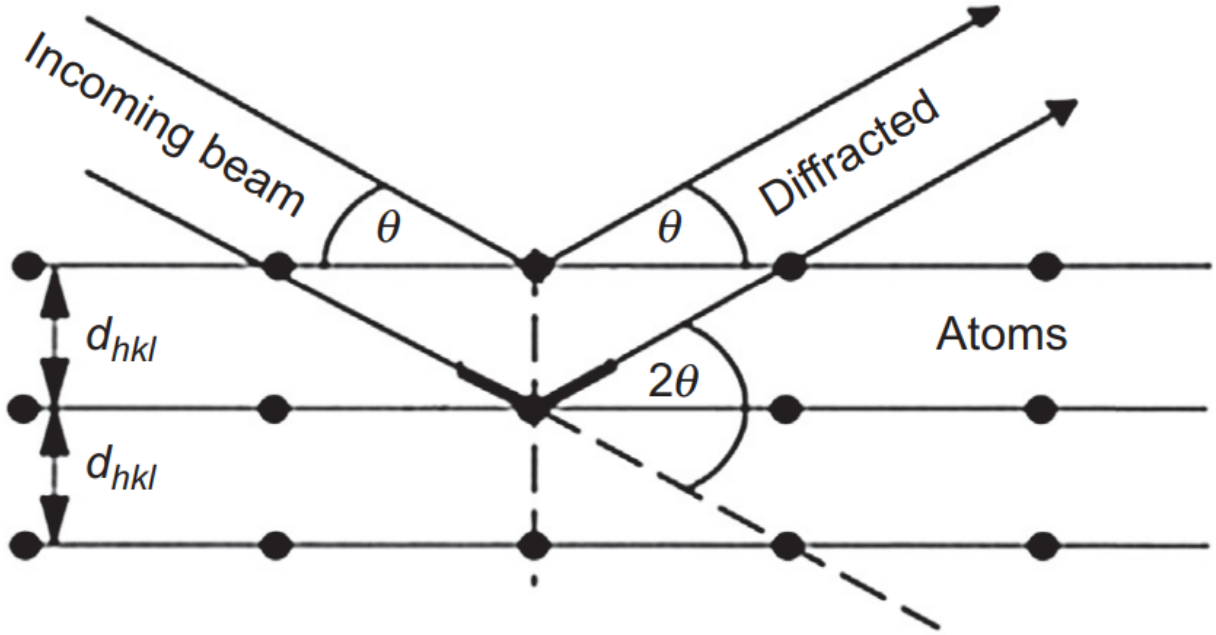

Figure 7.2. Geometrical condition for diffraction from lattice planes [12].

7.1.1 Experimental analysis and results

XRD analysis was carried out to confirm the exact crystal structures of the catalyst during the reaction. To characterise the $CuSiO_2$ and CuZnAlOx compounds in their actual state during the reaction, 30 mg were weighed and reduced in a PFR at 320°C in a 5% H_2/N_2 for 30 minutes at a rate of 10°C/min. The XRD patterns of the samples revealed the presence of CuO, ZnO and Cu metal. In contrast Al_2O_3 displayed amorphous-like structural features. As expected, the high-surface-area support material has broad diffraction peaks due to its limited long-range order. The presence of Cu_2O is difficult to detect in the XRD pattern due to the overlapping of the Cu_2O and ZnO peaks. As shown in Figure 7.4, before the reduction stage, both samples show diffraction peaks of crystalline CuO [ICSD 00-005-0661] at 35.6° and 38.7°, while in the HiFuel catalyst the peaks of ZnO [ICSD 01-079-0205] at 31.9° and 36.4° and a strong diffraction peak at 26.5° are clearly visible, representing the graphite [ICSD 03-065-6212] used as a binder in the catalyst. After the reduction stage, the diffraction peaks corresponding to CuO disappeared and the peaks corresponding to Cu [ICSD 01-070-3038] appeared clearly at 43.2°, 50.3° and 73.9°, indicating that the pre-reduction condition carried out is sufficient to completely reduce CuO to metallic Cu. [61],[62],[1]. Therefore, these were the catalyst reduction conditions chosen to be carried out before every activity test.

As crystallites become smaller, there are fewer planes available for Bragg diffraction to occur, so the diffraction peaks become broader. Therefore, this property can be utilised to determine the size of metal crystallites within a suitable range where the peaks are distinguishable from the instrumental line broadening, but not so broad that they cannot be differentiated from the background spectrum of the support [63]. The simplest and most used method for determining crystallite size from an XRD pattern is the Scherrer technique:

$$d = \frac{K\lambda}{\beta \cos(2\theta)} \tag{7.2}$$

where λ is the X-ray wavelength, β is the corrected Full Width at Half Maximum (FWHM), which is in radian, θ is the Bragg angle (degree) and K is the Scherrer constant. FWHM is the width of a spectrum curve measured between the background and the peak maximum (Figure 7.5). It has been obtained by fitting data via the drawing software OriginPro2023.

It should be emphasised that the unit of FWHM obtained from XRD patterns is in degrees. It must be converted to radians before being used in the Scherrer formula. It has been reported that the value of K is usually between 0.62 and 2.08, and between 0.9 and 1 for spherical particles, depending on the crystal shape, diffraction line indices and crystallite size dispersion of the powder. It was assumed to be 0.9 for the purpose of the calculations. The unit for d would be the same as the unit for λ. A limitation of this formula is that usually one peak is used for the calculation. Using this technique, the crystallite sizes of CuO, Cu and ZnO have been estimated from the respective broadening of the CuO (-111), Cu (111) and ZnO (101) lines at $2\theta = 35.55°, 43.19°$ and 36.36° respectively. The derived crystallite sizes are given in the table 7.1.

	Sample	Crystallite size (nm)
CuO	CZA	3
Cu	CuSiO2 reduced at 230°C	84
Cu	CZA reduced at 320°C	17
ZnO	CZA reduced at 320°C	2

Table 7.1. Average crystallite sizes of CuO, Cu and ZnO by X-ray line broadening analysis

It should be noted that the Scherrer method underestimates grain size because it ignores the broadening of diffraction peaks caused by microstrain in the lattice. This can lead to errors in the estimated crystallite size results which do not take into account the strain contribution to peak broadening [13],[64].

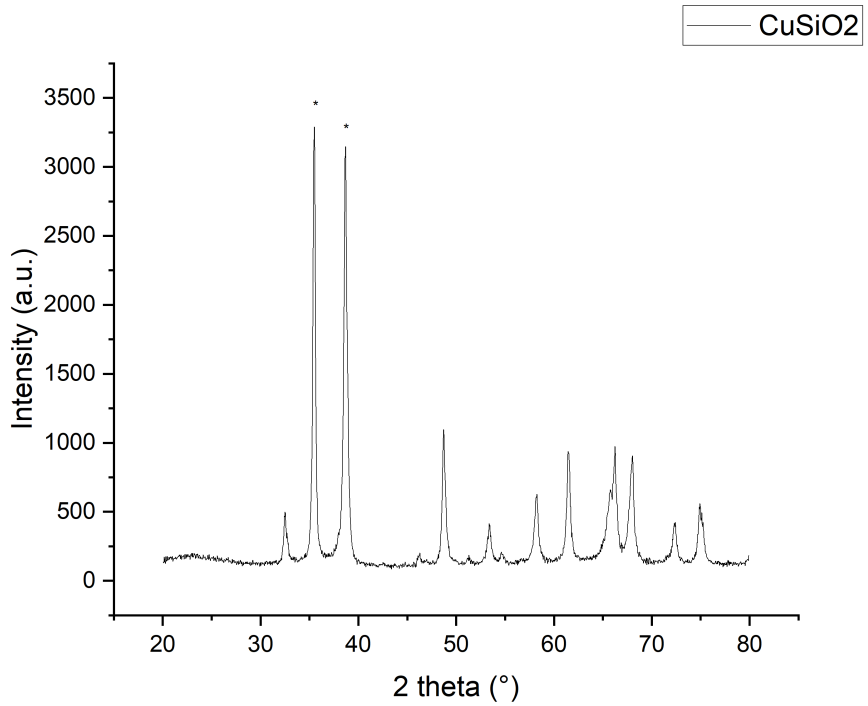

(a) $CuSiO_2$

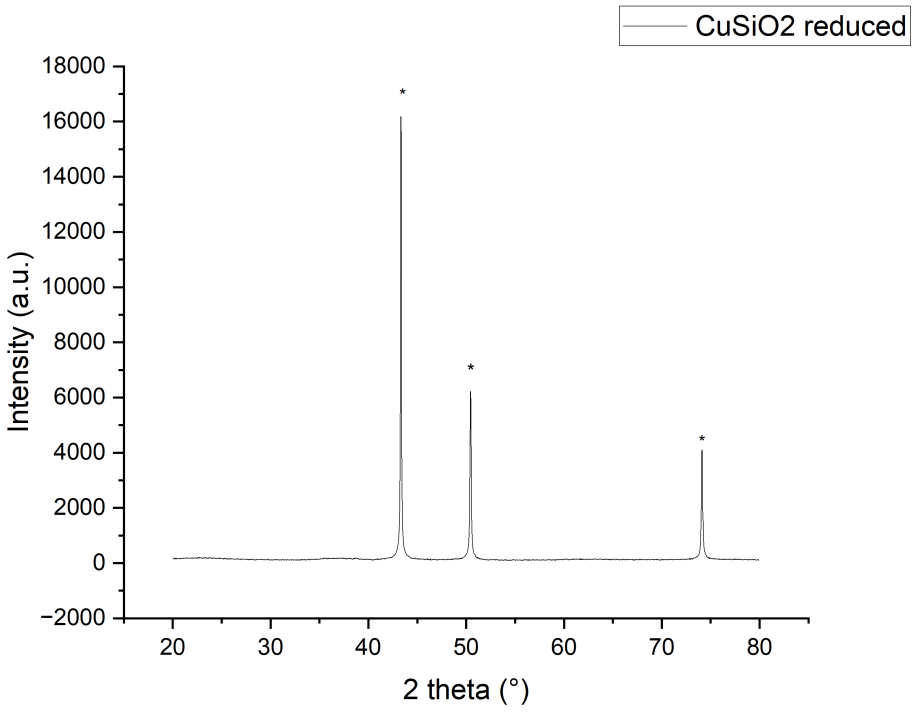

(b) $CuSiO_2$ reduced at 320°C

Figure 7.3. XRD patterns of $CuOSiO_2$ before and after the reduction stage

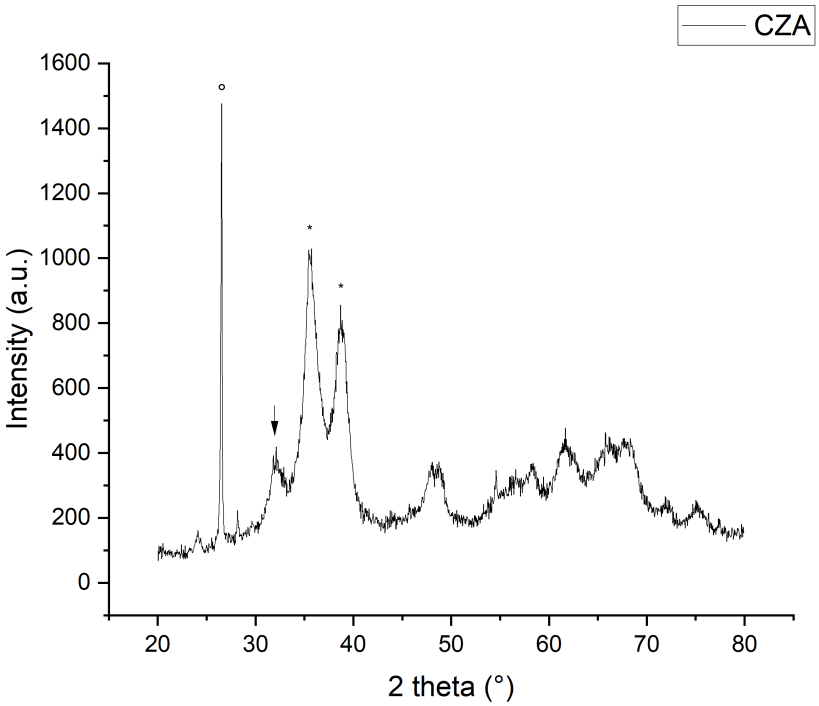

(a) $CuZnOAl_2O_3$

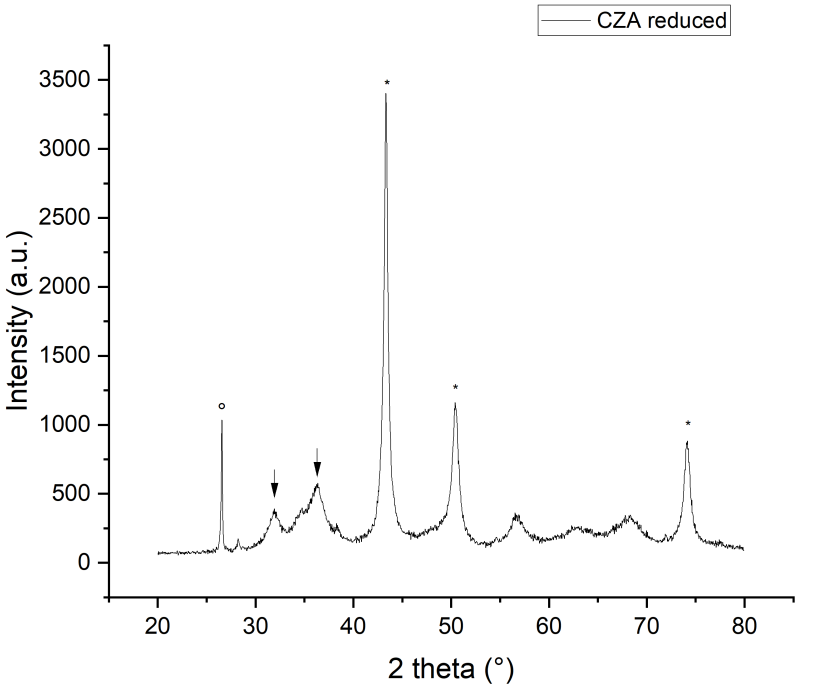

(b) $CuZnOAl_2O_3$ reduced at 320°C

Figure 7.4. XRD patterns of $CuZnOAl_2O_3$ before and after the reduction stage

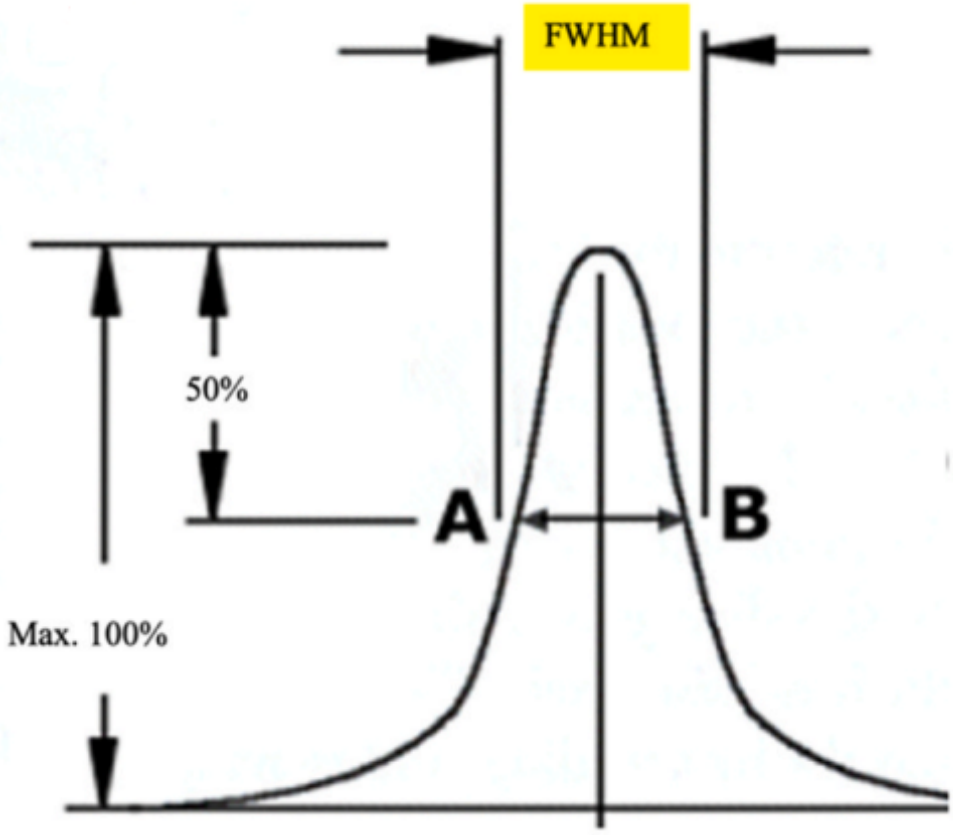

Figure 7.5. Determination of Full Width at Half Maximum (FWHM) [13].

7.2 Phisisorption of Nitrogen

In applications involving porous materials, such as industrial adsorbents, pigments, cement, polymers and catalysts, specific surface area is a crucial morphological characteristic. Pores with a diameter of less than 2 nm are classified as micropores, while mesopores range from 2 to 50 nm and macropores exceed 50 nm in diameter. Micropores can be divided into three categories: ultra-micropores ($d_{\text{pore}} < 0.7\text{nm}$), medium-micropores ($0.7\text{nm} < d_{\text{pore}} < 0.9\text{nm}$) and super-micropores ($d_{\text{pore}} > 0.9\text{nm}$). The most reliable methods for measuring specific surface area pore size distribution of porous materials, average pore diameter and volume are based on gas physisorption equilibrium isotherms of nitrogen, argon and carbon dioxide adsorbates. At temperatures below 100 K, the interaction between gas molecules and surfaces is ruled by Van der Waals forces with an adsorption heat of less than 4 kJmol^{-1}. These forces lead to the reversible physisorption of gas molecules onto the surface of a material in a multi-layer configuration. In contrast, chemisorption is a different process with higher heat of sorption in a monolayer irreversibly. Brunauer *et al.* [65] extended the Langmuir theory of monolayer adsorption to multilayer adsorption, where only adjacent layers of gas molecules interact, to calculate the surface area (S_{BET}). Barrett *et al.* [66] introduced the Kelvin equation for the calculation of pore size distribution, i.e. the Barrett-Joyner-Halenda (BJH) method. Nitrogen is the preferred gas adsorbate due to its inertness, high purity, affordability, and ability to interact with most solids. The N_2 physisorption analyzer comprises two main components: the degassing and adsorption stations (Figure 7.6). The first step involves calibrating a quartz cell for gas adsorption. This is achieved by evacuating the cell under high vacuum at 300°C for 2 hours (degassing), followed by a complete adsorption cycle in the empty cell at 77 K. After this, 50 - 150 mg of the sample is loaded into the cell, which is then connected to the degassing station. The purpose of sample degassing is the removal of physically adsorbed water and volatiles that may have accumulated during storage. For thermally sensitive solids, mild degassing temperatures are used. For mechanically fragile porous materials, a stream of inert gas is introduced instead of a vacuum, using the adsorbate path (ADS) connected to the degassing station (Figure 7.6). After degassing, the cell is transferred to the adsorption station and evacuated. The adsorption cycle is performed by incrementally introducing adsorbate gas using the calibration volume (CAL) connected to the adsorption station. The number of moles of nitrogen adsorbed is correlated to the difference between the measured pressure and that of the empty cell. The cell is kept at 77 K during measurements using a Dewar flask filled with liquid nitrogen [14].

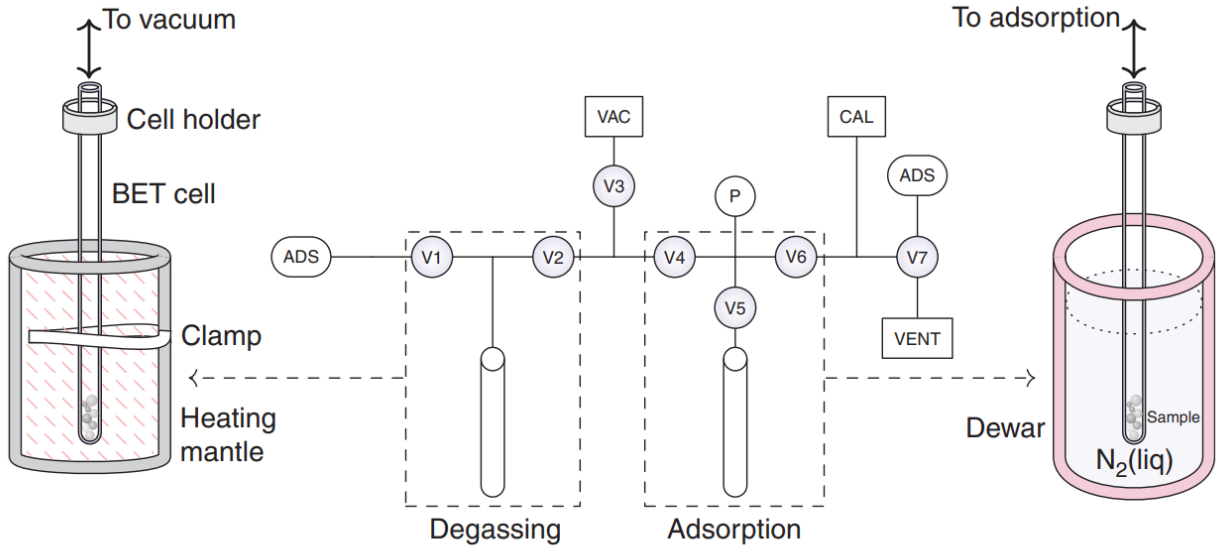

Figure 7.6. Gas physisorption adevice to achieve adsorption-desorption isotherm. Note: VAC = vacuum, CAL = calibration, ADS = adsorbate, P = pressure gauge, V1-V7 = valves [14].

7.2.1 Classification of physisorption isotherms

The categorization of nitrogen physisorption isotherms comprises six types, as shown in Figure 7.7.

Microporous solids with relatively small external surfaces, such as certain activated carbons, molecular sieve zeolites and porous oxides, exhibit reversible Type I isotherms. A Type I isotherm is concave with respect to the p/p_0 axis and the amount adsorbed approaches a limit. It is the available micropore volume, rather than the internal surface area, that limits the uptake. Enhanced adsorbent-adsorptive interactions in narrow micropores (micropores of molecular dimensions) result in micropore filling at very low p/p_0, causing a steep uptake. Microporous materials with predominantly narrow micropores (width $<\sim$ 1nm) exhibit Type I(a) isotherms, whereas materials with broader pore size distributions, including wider micropores and possibly narrow mesopores ($<\sim$ 2.5nm), exhibit Type I(b) isotherms. The physisorption on non-porous or macro-porous adsorbents results in reversible type II isotherms. The shape of the adsorption isotherm is a consequence of the unrestricted monolayer - multilayer adsorption up to high p/p_0 fractions. If the knee is sharp, this usually corresponds to the completion of the monolayer coverage at point B, which marks the beginning of the middle, almost linear portion. A more gradual curvature, with a less pronounced point B, indicates a significant overlap of the monolayer coverage and the beginning of the multilayer adsorption. When $p/p_0 = 1$, the thickness of the adsorbed multilayer generally increases indefinitely. For a Type III isotherm, there is no Point B and therefore no recognisable monolayer starting to form. The interactions between the adsorbent and the adsorbate are now relatively weak and the adsorbed molecules will cluster around the most favourable sites on the surface of a non-porous or macro-porous solid. Unlike a Type II isotherm, the amount adsorbed remains finite at the saturation pressure, i.e. when p/p_0 is equal to 1. Mesoporous adsorbents, such as many oxide gels, industrial adsorbents, and mesoporous molecular sieves, give rise to Type IV isotherms. The adsorbent-adsorptive interactions and also the interactions between the molecules in the condensed state determine the adsorption characteristics in mesopores. The adsorption process begins with the initial monolayer-multilayer adsorption on the mesopore surfaces, taking the same course as the corresponding portion of the Type II isotherm. This stage is followed by pore condensation, a phenomenon in which a gas condenses to a liquid-like phase in a pore at a pressure below the saturation pressure of the bulk liquid. Type IV isotherms typically have a final saturation plateau, which may collapse to a mere inflection point. Capillary condensation is associated with hysteresis in a Type IVa isotherm. This occurs when the pore diameter passes a certain critical value, which depends on the adsorption system and the temperature. Pores wider than approximately 4 nm exhibit this behaviour for nitrogen and argon adsorption at 77 K and 87 K respectively. A completely reversible Type IVb isotherm is displayed by mesopores of smaller sizes. They are also typically associated with conical and cylindrical mesopores which are closed at the tapered end. The shape of the Type V isotherm is very similar to that of Type III in the low p/p_0 range. This similarity can be explained by the relatively weak adsorbent-adsorbate interactions. At higher p/p_0, molecular agglomeration is followed by pore filling. For example, hydrophobic microporous and mesoporous adsorbents exhibit Type V isotherms during water adsorption. The Type VI isotherm is a reversible stepwise process that represents layer-by-layer adsorption on a highly uniform nonporous surface. The step-height indicates the capacity for each adsorbed layer, while the steepness of the step depends on the system and the temperature [15].

7.2.2 Adsorption hysteresis

Capillary condensation is considered to be the primary cause of the reproducible and permanent hysteresis loops observed in the multi-layer region. This phenomenon is governed by adsorption metastability and/or network effects. Due to the metastability of the adsorbed multilayer in an open-ended pore, delayed condensation occurs. This means that, in such a collection of pores, the adsorption stage of the hysteresis loop is not in thermodynamic equilibrium. On the other hand, the desorption stage represents a reversible transition from liquid to vapour. This means that when the pores are filled with liquid-like condensate, thermodynamic equilibration occurs during the desorption process. Additionally, in complex pore structures, desorption paths may be influenced by network effects and pore blocking. These phenomena occur when broad pores can only access the outer surface through narrow necks, such as in the shape of an ink bottle pore. The broad pores remain filled throughout desorption until the narrow necks are emptied at lower vapour pressures. The

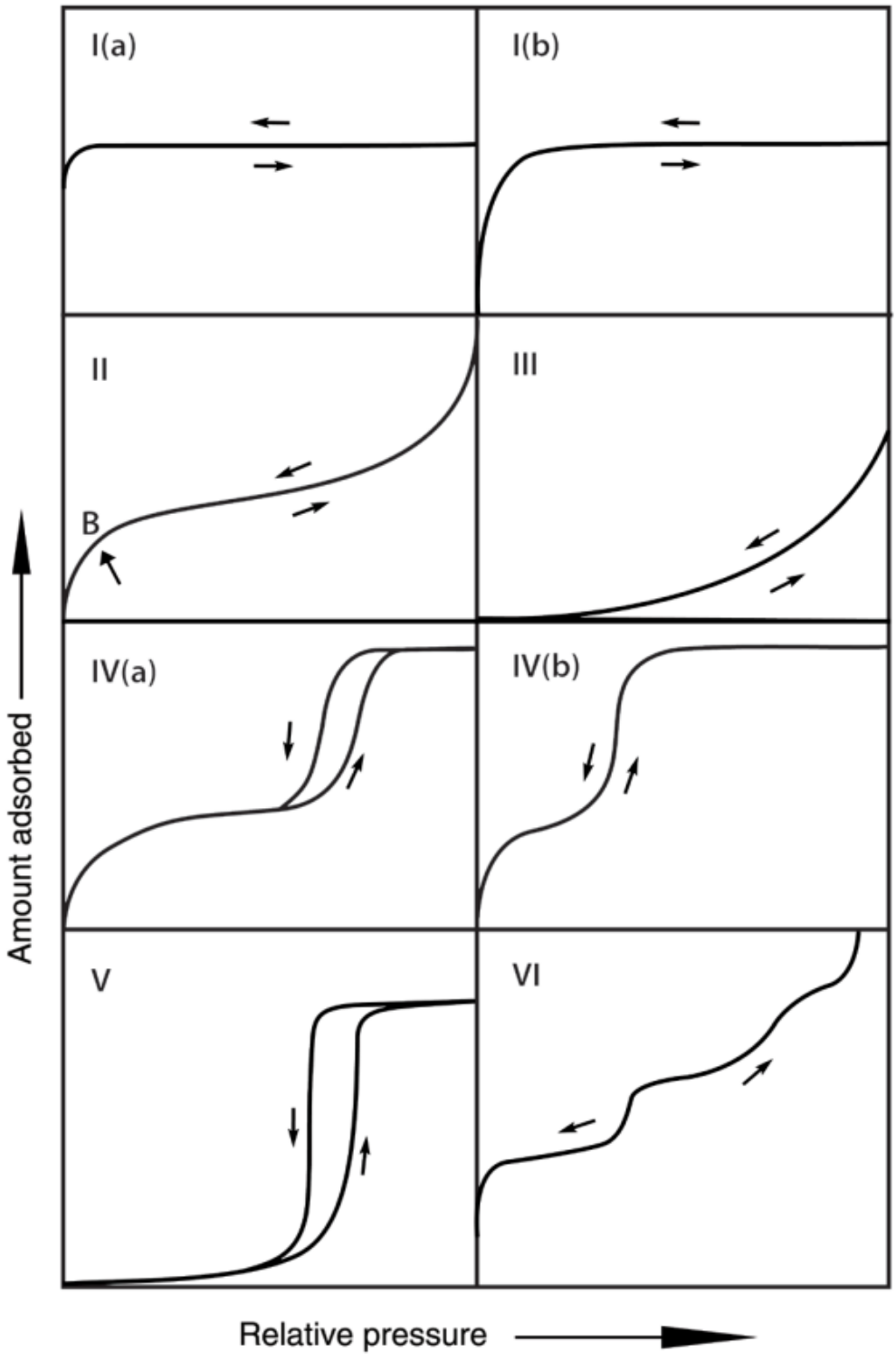

Figure 7.7. Nitrogen adsorption-desorption isotherms [15].

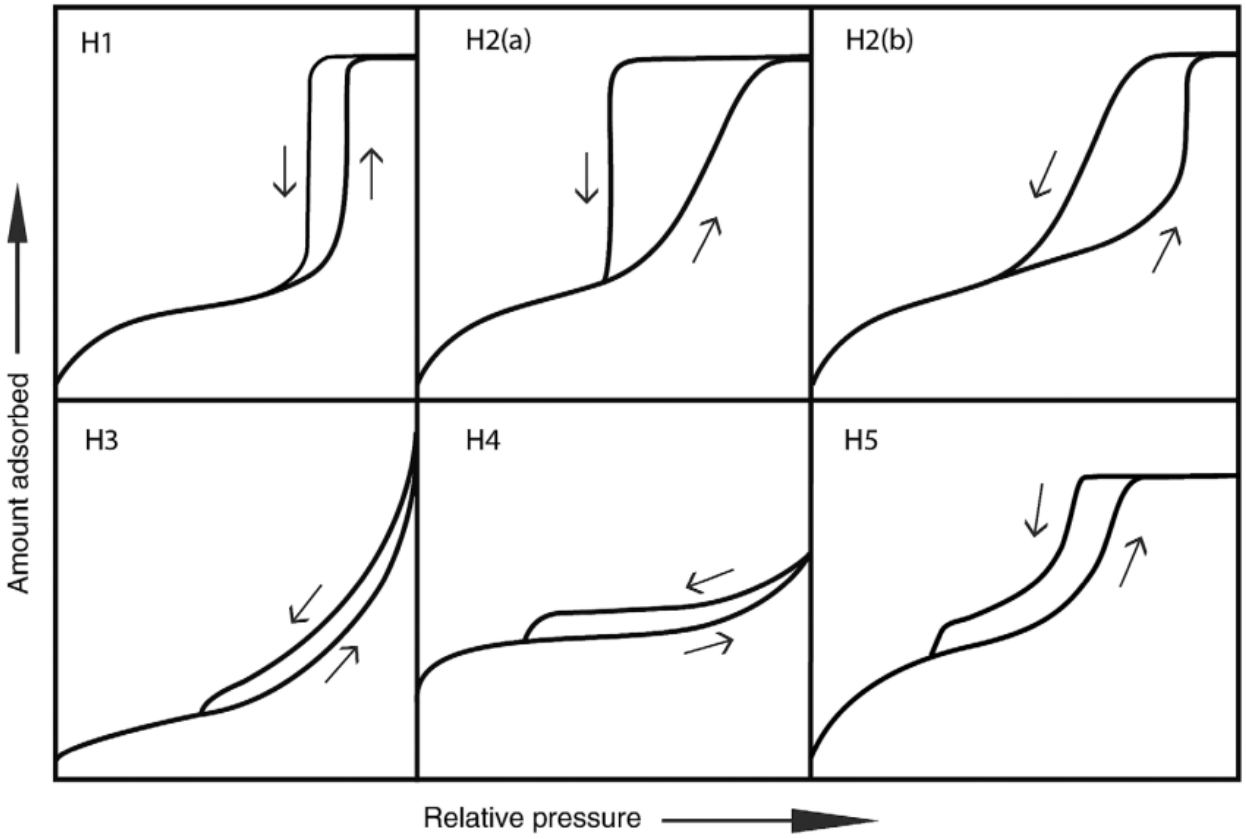

Figure 7.8. Types of hysteresis loops obtained by nitrogen physisorption [15].

desorption vapour pressures in a pore network are determined by the size and spatial distribution of the necks. Consequently, if the neck diameters are not too narrow, the network can empty at a relative pressure corresponding to a characteristic percolation threshold. This means that valuable information about the size of the necks can be obtained from the desorption branch of the isotherm [15].

7.2.3 Type of hysteresis loops

The hysteresis loops Type H1, H2(a), H3 and H4 were originally identified in the IUPAC classification of 1985. Due to more recent findings, the types have been enlarged and the main types are shown in Figure 7.8. Specific features of the pore structure and the underlying adsorption mechanism are fairly closely associated with each of these six characteristic types. The Type H1 loop is typically observed in materials that possess a narrow and uniform range of mesopores. Examples of such materials include templated silicas, some controlled pore glasses, and ordered mesoporous carbons. The steep and narrow loop is a clear indication of delayed condensation on the adsorption branch, and network effects are generally minimal. However, it has also been found that H1 type hysteresis can occur in networks of ink bottle pores where the width of the neck size distribution is similar to that of the pore/cavity size distribution. Type H2 hysteresis loops are characterised by more complex pore structures where network effects play an important role. Either cavitation-induced evaporation or, in a narrow range of pore necks, pore blocking/percolation is attributed to the steep desorption branch. The H2(b) type loop is also related to pore blocking, but the size distribution of the neck widths is now much wider. The H3 loop has two peculiarities: the adsorption path resembles a Type II isotherm; the lower limit of the desorption path is usually at cavitation-induced p/p0. The H4 loop is similar to the previous one, but the adsorption branch now consists of a combination of Types I and II and the more significant uptake at low p/p0 is due to the filling of micropores. The H5 type loop has a

distinctive shape that is associated with certain pore structures that contain both open and partially blocked mesopores [15].

7.2.4 Application of the BET method

Although the model on which the theory is based is oversimplified, the Brunauer-Emmett-Teller (BET) gas adsorption method is the most commonly used standard method for determining the surface area of finely divided and porous materials. The BET equation is typically applied in its linear form, which is as follows:

$$\frac{p}{n^a(p^0-p)} = \frac{1}{n^a_m C} + \frac{(C-1)}{n^a_m C}(p/p^0) \tag{7.3}$$

where n^a is the amount adsorbed at the relative pressure p/p^0, n^a_m is the monolayer capacity and the constant C is exponentially related to the enthalpy of adsorption in the first adsorbed layer. The isotherm's shape in the BET range is characterised by the value of C, but it does not offer a quantitative measure of the enthalpy of adsorption. It is generally acknowledged that C only gives an approximation of the order of magnitude of the adsorbent-adsorbate interaction energy. As a consequence, when reporting BET data, the C values are stated but not converted to enthalpies of adsorption. A sharp knee in the isotherm is associated with high values of C (~ 100), which allows for the visual determination of the uptake at Point B. This value typically agrees with the n^a_m value derived from equation 7.3 within a few percent. However, if C is low (~ 20), Point B cannot be detected as a single point on the isotherm. Regrettably, it is not possible to provide a precise mathematical description of Point B, and therefore, the theoretical significance of the amount adsorbed at Point B is uncertain. The BET equation necessitates a linear relationship between $p/n^a(p^0_p)$ and p/p^0. However, this linearity is limited to a small portion of the isotherm, usually within the relative pressure range of 0.05-0.30. For energetically more homogeneous surfaces, such as nitrogen adsorption on graphitised carbon, this range shifts to lower relative pressures. The BET method's second stage involves calculating the surface area, commonly referred to as the BET area. This requires the knowledge of the average area occupied by the adsorbate molecule in the complete monolayer, also termed the molecular cross sectional area a_m.

$$A_S(BET) = n^a_m L a_m \tag{7.4}$$

$$a_S(BET) = A_S(BET)/m \tag{7.5}$$

where $A_S(BET)$ and $a_S(BET)$ are respectively the total and specific surface areas of the adsorbent of mass m and L is the Avogadro constant. For the closed-packed nitrogen monolayer at 77 K, the area per molecule is $a_m(N2) = 0.162\text{nm}^2$. This value was calculated based on the density of liquid nitrogen at 77 K, assuming hexagonal close packing. This value seems to be acceptable within a range of approximately $\pm 10\%$ for various surfaces. For finely divided or porous industrial products, a simplified method can be used for routine surface area measurements. This involves the use of only a single point on the adsorption isotherm, which should be located in the linear region of the BET plot [67].

7.2.5 Application of the Kelvin equation

The Kelvin equation can be used to analyse the size of mesopores. It describes the shift of the gas-liquid phase transition of a confined fluid from bulk coexistence in terms of the surface tension of the bulk fluid and the molar volume of the liquid [15]:

$$\frac{1}{r_1} + \frac{1}{r_2} = -\frac{RT}{\gamma V_m} \ln \frac{p}{p^0} \tag{7.6}$$

This relationship relates the relative pressure at which condensation occurs to the principal radii r_1 and r_2 of the curvature of the liquid meniscus in the pore. This approach requires us to assume a model for the pore shape and that the curvature of the meniscus is directly related to the pore width. The shape of the pore is typically assumed to be either cylindrical, with a hemispherical meniscus and $r_1 = r_2$, or slit-shaped, with a hemicylindrical meniscus and $r_2 = \infty$. By rearranging the Kelvin equation and replacing the terms

for principal radii of curvature with $2/r_K$, the resulting equation is as follows:

$$r_K = \frac{2\gamma V_m}{RT \ln p^0/p} \tag{7.7}$$

where r_K is often called the Kelvin radius. For a cylindrical pore with a radius of r_p, a correction is required to take into account the thickness of the layer already adsorbed on the walls of the pore, known as the multi-layer thickness t_c [67]:

$$r_p = r_K + 2t_c \tag{7.8}$$

The modified Kelvin equation for cylindrical pores is as follows:

$$\ln p/p^0 = -\frac{2\gamma V_m}{RT(r_p - t_c)} \tag{7.9}$$

Various methods for analyzing mesopore size, which utilize the modified Kelvin equation, have been proposed, including those by Barrett, Joyner, and Halenda (BJH) and Broeckhoff and de Boer. To account for the pre-adsorbed multilayer film, the Kelvin equation is combined with a standard isotherm (the t-curve) determined on certain well-defined non-porous solids [15]. The change in the thickness of the adsorbed film is calculated by BJH through the decrease of relative pressure in the desorption branch. Each decrement is believed to be a result of the evacuation of the largest pores from the capillary condensate, as well as a reduction in the thickness of the physically adsorbed layer [14]. However, due to the restrictive hypotheses of BJH, this method is unable to describe both the micropore diameter and the narrow mesopores, as it does not properly account for the curvature and enhanced surface forces (it was shown that for pore diameters $<\sim$ 10nm the pore size will be underestimated by approximately 20-30%) [14],[15].

7.2.6 Experimental results

A Micromeritics TriStar II 3020 was deployed for the N_2 physisorption of the CZA catalyst. Prior to analysis, two pre-treatment stages were carried out with nitrogen flow to remove all impurities. The first stage was performed at 90°C for 60 minutes with a ramp rate of 5°C/min, the second at 300°C for 240 minutes with a ramp rate of 10°C/min. Figure 7.9 shows the adsorption-desorption isotherm, which corresponds to the type IV(a) isotherm of the IUPAC categorisation, characteristic of the mesoporous adsorbents. In this case, the final plateau of saturation has collapsed to a point of inflexion. It is also clearly visible the hysteresis loop associated with capillary condensation, corresponding to the H1 type shown in Figure 7.8, with a characteristic narrow and steep loop in the relative pressure range 0.5-1. It is expected to be found in materials that are characterised by a narrow and uniform range of mesopores.

The BET and BJH methods were used to determine the surface area and pore size and volume respectively. All the measurements were conducted at 77K. The results are given in Table 7.2.

Sample	BET surface area (m^2g^{-1})	BJH pore size (nm)	BJH pore volume (cm^3g^{-1})
CZA	67	15.2	0.26

Table 7.2. BET and BJH analysis of CZA catalyst results

7.3 Scanning electron microscopy (SEM)

Scanning electron microscopy (SEM) produces high-resolution images of an object's surface, revealing its physical features and composition. SEM uses a focused beam of electrons that passes through a series of lenses and apertures to scan the sample. The vacuum conditions ensure high-quality imaging and prevent any interaction between molecules or atoms already present in the microscope column and the electron beam. Additionally, the vacuum protects the electron source from vibrations and noise.

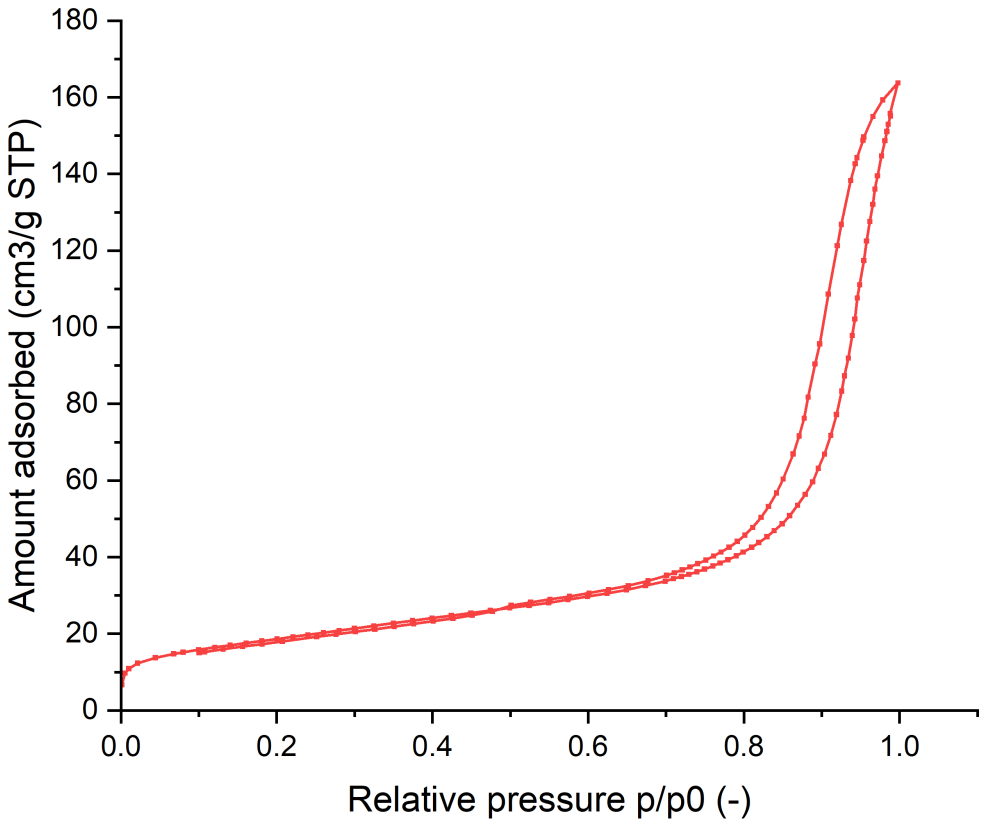

Figure 7.9. N_2 adsorption-desorption isotherm of the CZA catalyst

The sample is scanned by electron beams in a raster pattern, moving from side to side and top to bottom. The beams interact with surface atoms, producing signals such as secondary electrons, backscattered electrons, and rays that are unique to the sample. These signals are detected by the microscope and displayed as high-resolution images on a computer screen. Figure 7.10 shows a schematic illustration of the main components of the SEM microscope.

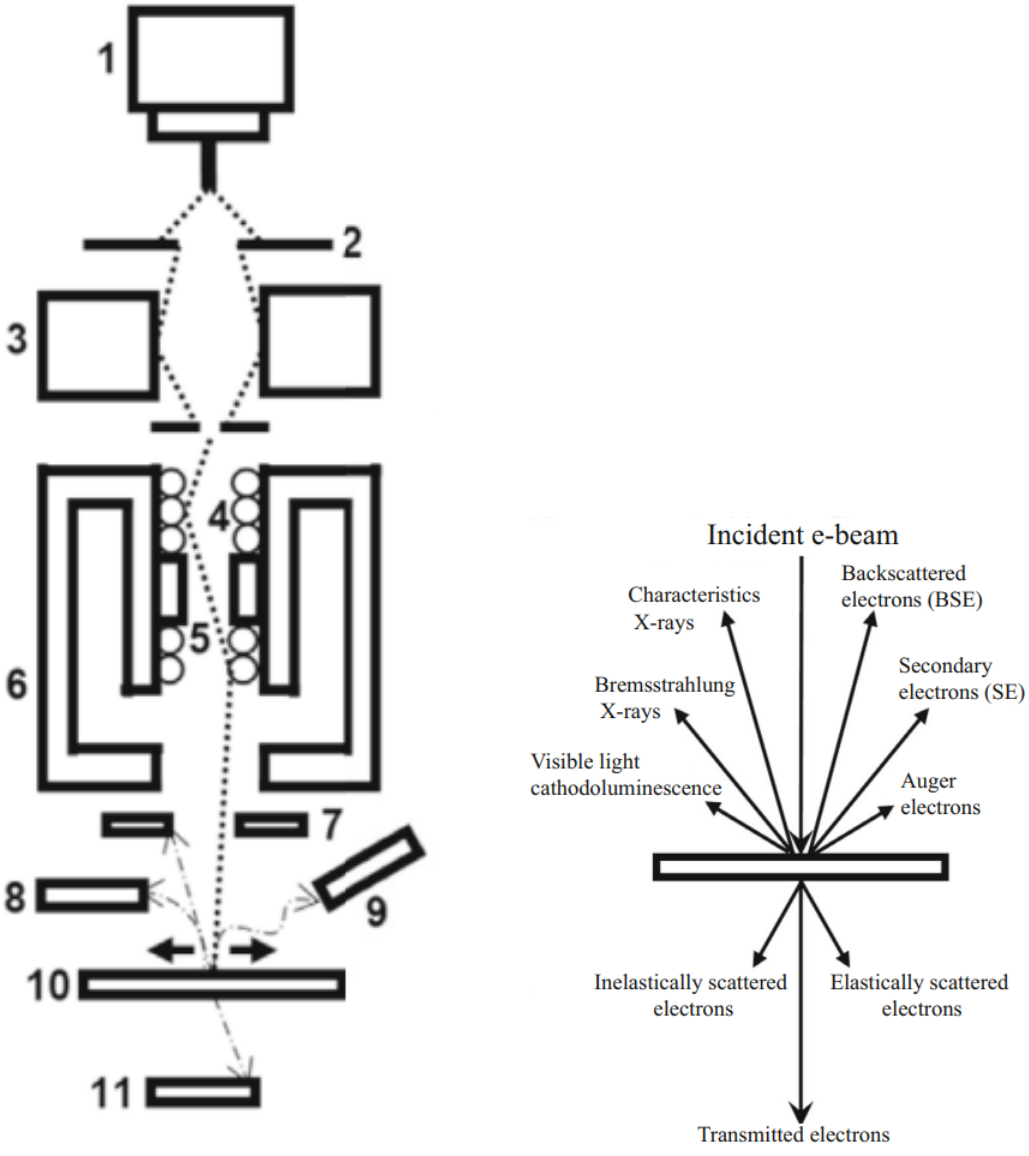

(a) **(b)**

Figure 7.10. (a) Schematic figure showing the basic components of a scanning electron microscope: (1) electron gun, (2) spray aperture, (3) condenser lens,(4) deflection coils, (5) stigmator, (6) objective lens, (7) backscatter detector, (8) secondary electron detector, (9) X-ray detector, (10) sample stage, and (11) scanning transmission electron detector. (b) Illustration of the interaction between the electron beam and the specimen. Figures taken from [16].

Electrons are generated at the top of the microscope's column by the electron source. The anode plate, which has a positive charge, attracts the electrons to form a beam. The size of the beam is controlled by the

condenser lens, which also determines the number of electrons in the beam. The beam size can be controlled by the apertures, which determines the image resolution. The scanning coils deflect the beam along the x and y axes, scanning the sample surface in a raster pattern. The objective lens, the last lens in the electron beam sequence and closest to the sample, focuses the beam to a small spot on the sample. SEM lenses are electromagnetic (electrons cannot pass through glass) and made up of a coil of wires inside metal poles. When an electric current passes through these coils, they generate a magnetic field. Electrons are highly sensitive to these magnetic fields, which enables the microscope lenses to control them.

SEM instruments may use three different methods for generating electrons (electron sources): the field emission gun, which creates a powerful electric field to pull electrons away from atoms and produce high-resolution images in a vacuum; the thermionic filament, which heats tungsten to emit electrons and has a lifespan of approximately 100 hours under intense heat conditions; cerium hexaboride cathode provides a signal-to-noise ratio that is ten times better than tungsten and a longer lifetime of over 1,500 hours. Scanning electron microscopy (SEM) has a wide range of research and practical applications due to its ability to provide detailed topographical images and versatile data. Other advantages of this technique include the straightforward operation of SEM equipment with specialist but user-friendly software support, and the fact that modern SEM data is in digital form. Analysis can be completed in less than five minutes, making it a rapid process that provides valuable insights with minimal preparation [S1].

7.3.1 Experimental analysis and results

The surface morphology of the CZA catalyst was examined using a FE-SEM SUPRA 35VP (Carl Zeiss) field-emission scanning electron microscope for chemical characterization. The images below provide information on the catalyst's overall morphology (Figures 7.11 and 7.12).

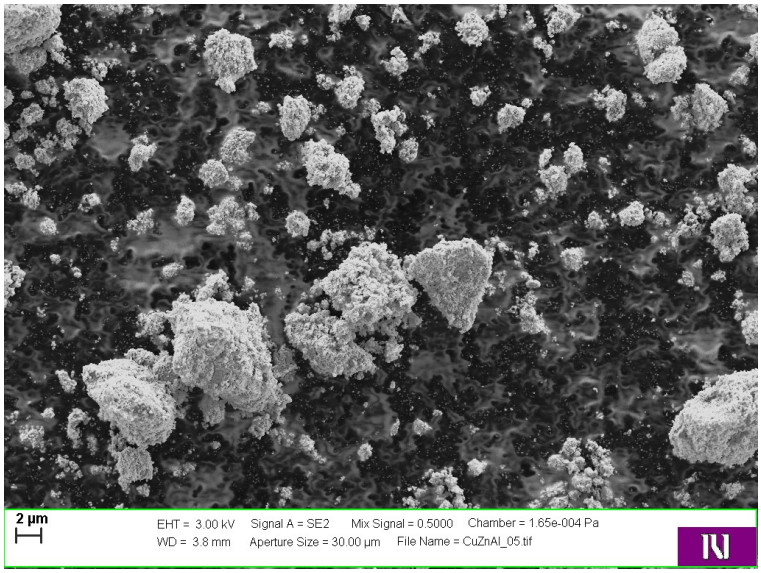

Figure 7.11. SEM image of the CZA catalyst

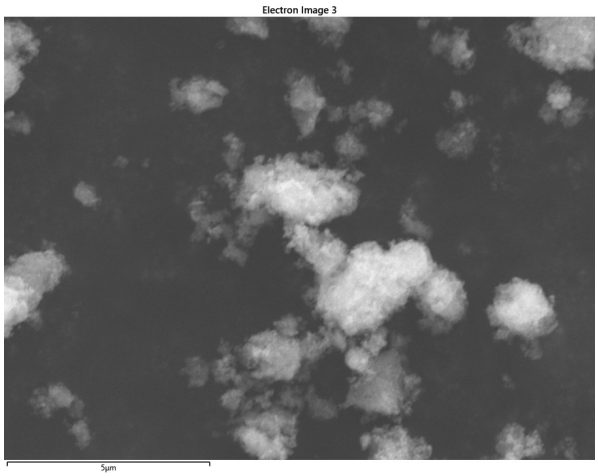

(a)

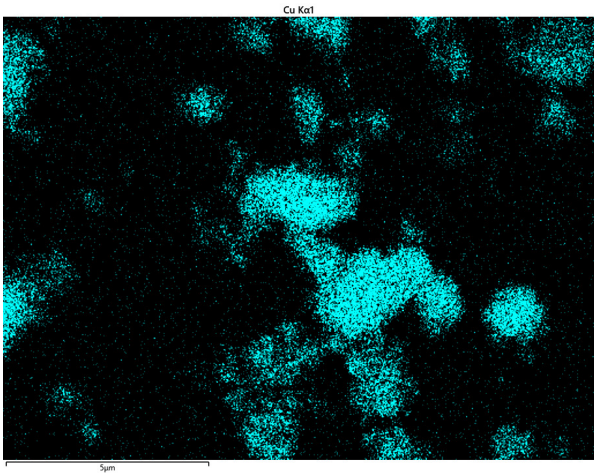

(b)

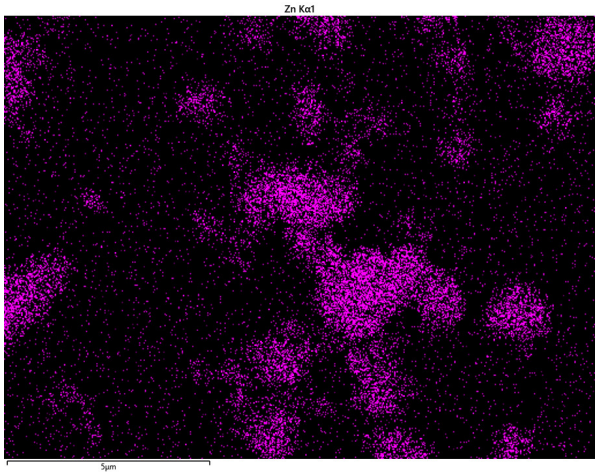

(c)

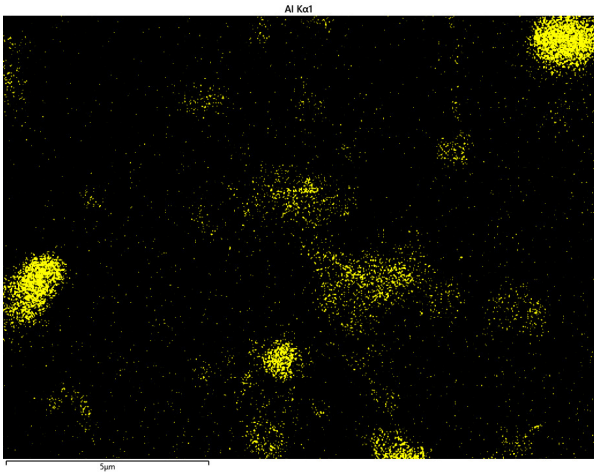

(d)

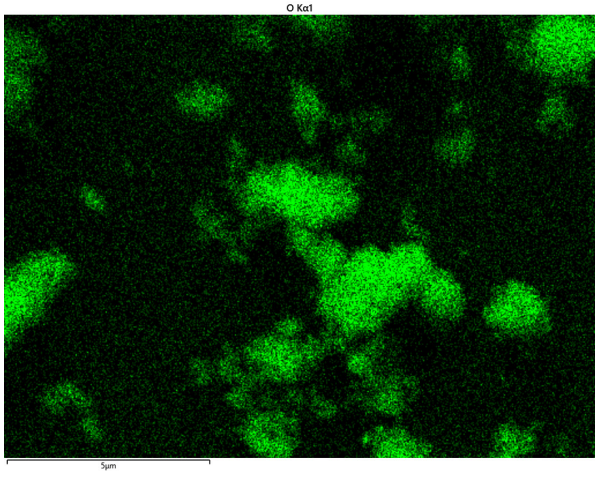

(e)

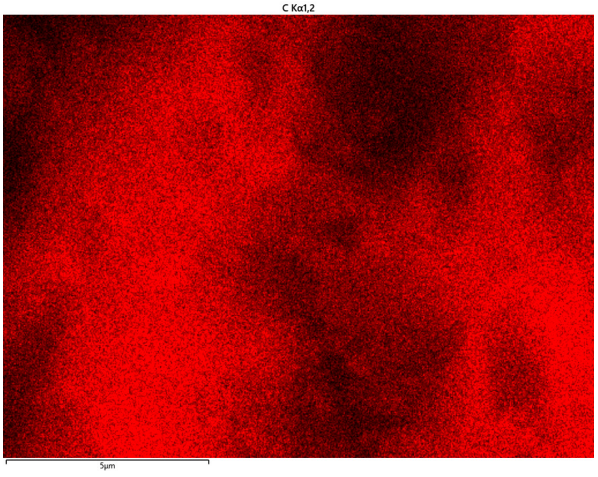

(f)

Figure 7.12. SEM images and EDX mapping which show spatial distribution of elements in the sample: (a) general morphology; (b) Copper; (c) Zinc; (d) Aluminium; (e) Oxygen; (f) Carbon. Note: The intensity of the carbon map (red) is high due to the positioning of the samples on glue that contains carbon, resulting in a strong C signal.

8 Activity tests and reaction mechanism insights

8.1 Reactor and analitycal setup

The experimental setup for evaluating catalyst activity in the Reverse Water-Gas Shift reaction involves a Harrick Scientific reactor (HVC-MRA-5), a fixed bed reactor capable of operating at high temperatures (until *ca.* 500°C), shown in Figure 8.1 [68].

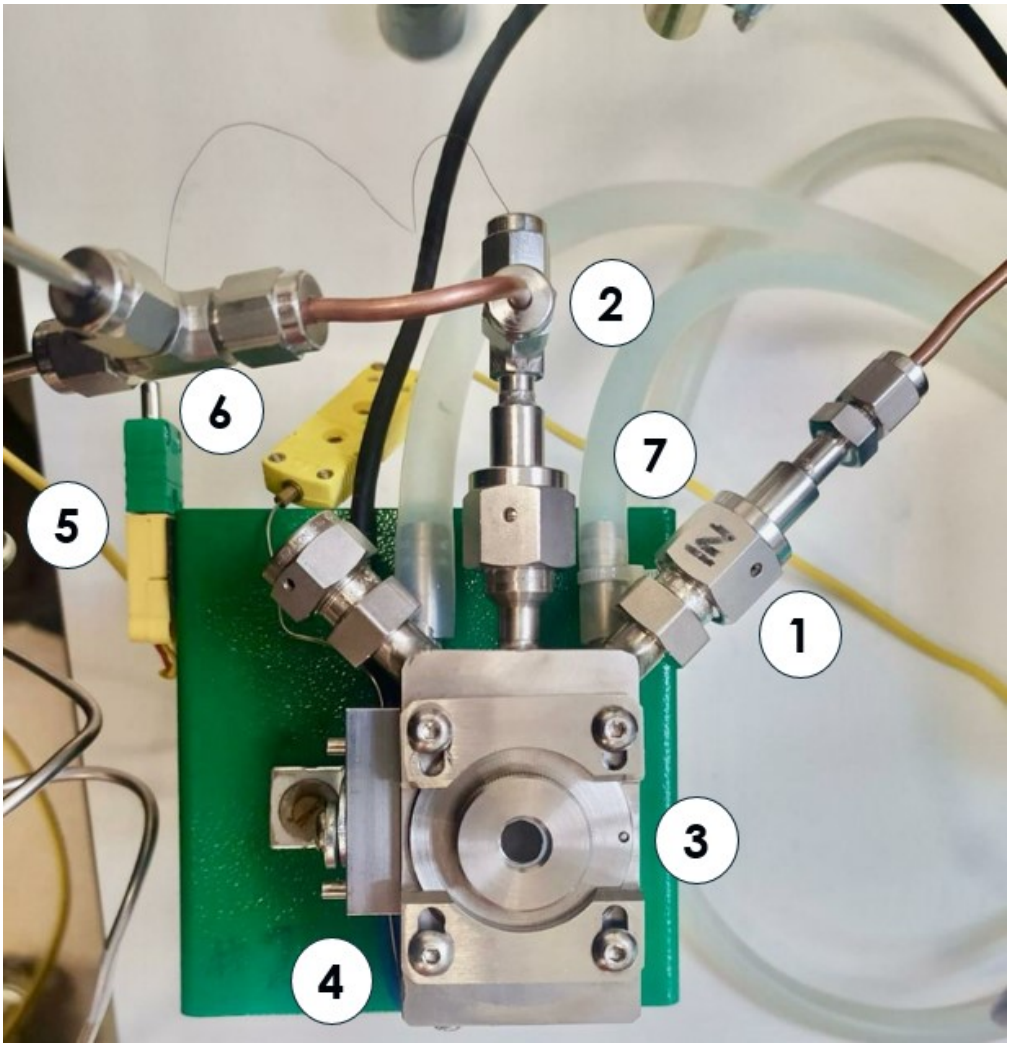

Figure 8.1. Harrick Scientific reactor employed for the catalytic tests: (1) gas inlet; (2) gas outlet; (3) Raman dome assembly with fused silica window (HVC-MRA); (4) cartridge heater; (5) cartridge heater/cell body thermocouple; (6) sample thermocouple via outlet line; (7) cooling ports.

Brooks mass flow controllers 5850 E regulate the flow rates of CO_2, H_2, and N_2 gases. The gases are sourced from CO_2, H_2 and N_2 gas cylinders from Messer. The catalysts, ranging from 3 to 30 mg, are loaded into the reactor's heater cup. The catalyst support (SiC), which showed no catalyst activity, is placed at the bottom, with only the top 1–2 mm of the cup containing the catalyst for proper illumination. SiO2 windows on the reactor allow visible light illumination of the catalyst bed. A PID temperature controller, Harrick ATK/low voltage, maintaines the catalyst bed temperature, with the heating block located at the bottom of the bed. The reactor's window is exposed to room temperature, and has a radius of 0.64 cm. The cooling water circuit is controlled through a Masterflex Console Drive. The catalyst bed was illuminating using a

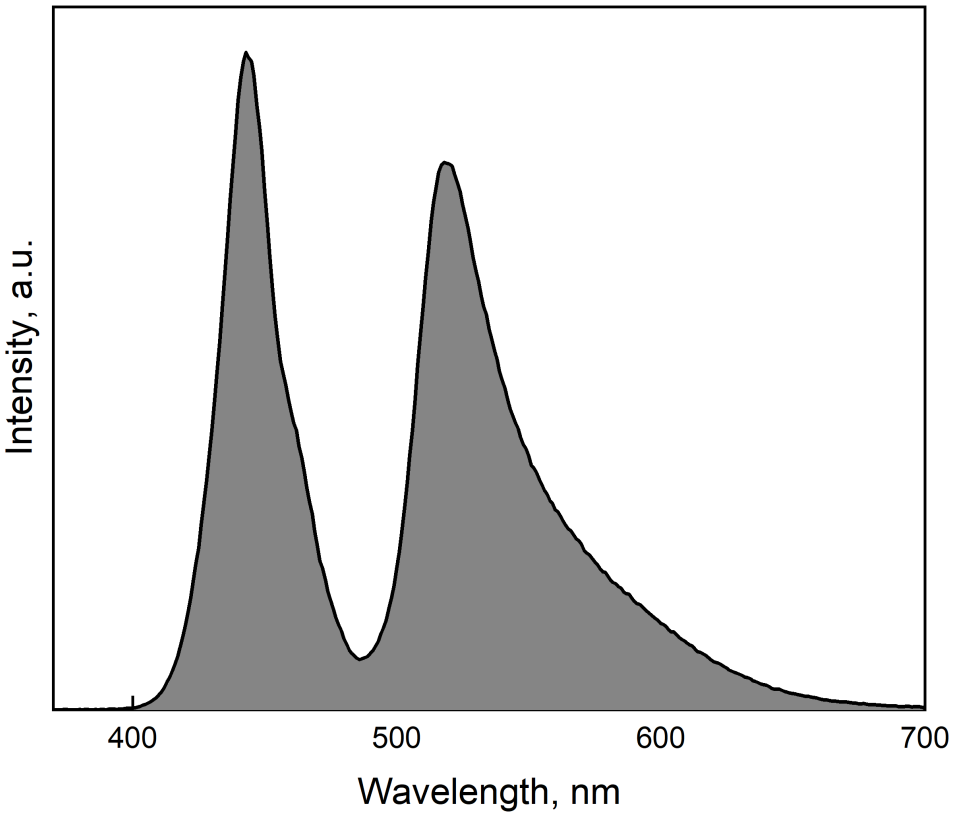

Figure 8.2. Schott KL2500 LED emission spectrum

Schott KL 2500 LED visible light source with fiber optic cable. Using this setup the light intensity reaching the catalyst bed was measured as 0.77 W (Figure 8.2). An Agilent Technologies 490 Micro GC is used to identify and quantify the product gases [2]. The entire experimental set up is schematized in Figure 8.3.

8.2 Light-assisted CO_2 hydrogenation performances

Using Mears dimensionless criteria, the effect of mass transport was estimated for photo-enhanced RWGS reaction over CuZnAlOx catalyst. Mears criterion for external diffusion:

$$\text{If } \frac{-r'_A \rho_b R n}{k_c C_{Ab}} < 0.15 \tag{8.1}$$

then the external mass transfer effects can be neglected, where $-r'_A[\text{kmol}\,\text{kg}_{\text{cat}}^{-1}\text{s}^{-1}]$, $n[-]$ is the reaction order, $R[\text{m}]$ is the catalyst particle radius, $\rho_b[\text{kg}\,\text{m}^{-3}]$ is the bulk density of catalyst bed, $\rho_c[\text{kg}\,\text{m}^{-3}]$ is the solid catalyst density, $C_{Ab}[\text{kmol}\,\text{m}^{-3}]$ is the bulk gas concentration of the component A and $k_c[\text{m}\,\text{s}^{-1}]$ is the mass transfer coefficient. Mears criterion for internal diffusion:

$$\text{If } C_{\text{WP}} = \frac{-r'_{\text{A(obs)}} \rho_c R^2}{D_e C_{As}} < 1 \tag{8.2}$$

then the internal mass transfer effect can be neglected, where $-r'_{\text{A(obs)}}[\text{kmol}\,\text{kg}_{\text{cat}}^{-1}\,\text{s}^{-1}]$, $R[\text{m}]$ is the catalyst particle radius, $\rho_c[\text{kg}\,\text{m}^{-3}]$ is the solid catalyst density, $D_e = \frac{D_{AB}\phi_p\sigma_c}{\tau}[\text{m}^2\,\text{s}^{-1}]$ is the effective gas-phase diffusivity, $D_{AB}[\text{m}^2\text{s}^{-1}]$ is the gas-phase diffusivity, $\phi_p[-]$ is the pellet porosity, $\sigma_c[-]$ is the constriction factor, $\tau[-]$ is the tortuosity and $C_{As}[\text{kmol}\,\text{m}^{-3}]$ is the gas concentration of the component A at the catalyst

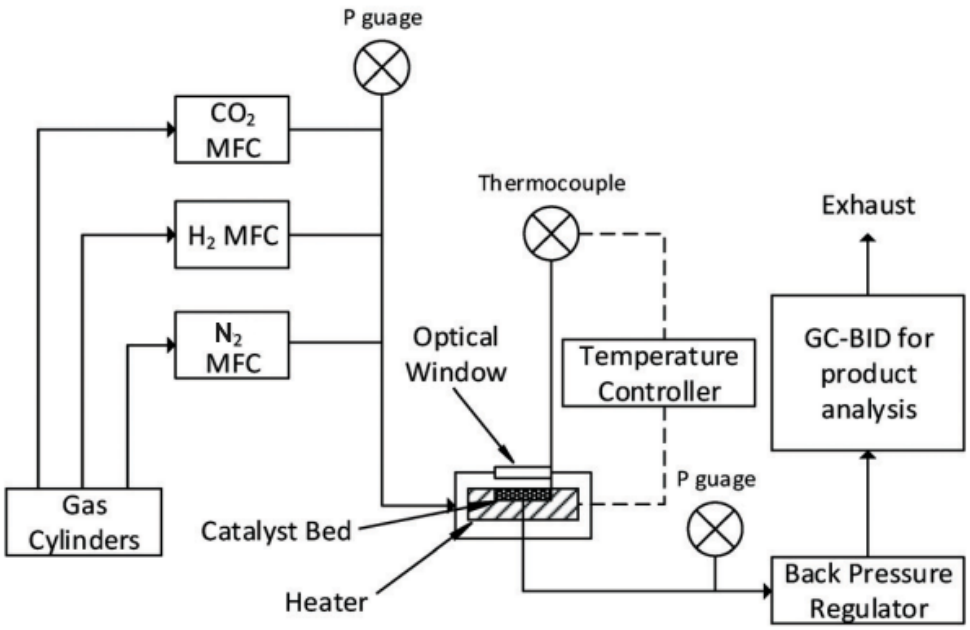

Figure 8.3. Experimental setup for test of activity of different catalyst under light and dark conditions [2].

surface.

The calculations were based on reaction data obtained in both dark and light conditions. All calculated values are below the control regime criteria, indicating the absence of mass diffusion limitations. Moreover The reactor was operated in differential mode at low conversions, typically less than 15%, to not overcome the thermodynamic limit.

8.2.1 Effect of CO_2/H_2 ratio

The catalyst was tested under three different CO_2/H_2 ratios: 25/60, 1 and 1.5, in both dark and light conditions at a constant temperature of 300°C. Two parameters were used to describe the photo-enhancement of the CO production rate:

1. the difference between the reaction rates in light and dark: Light-Dark (absolute gain)
2. the ratio between the reaction rate in light and dark: Light/Dark (relative gain)

The experiments in equimolar CO_2/H_2 and surplus CO_2 concentration gave results that were similar and better than that with surplus hydrogen (Figure 8.4). Consequently, all subsequent experiments were carried out with a CO_2/H_2=1 reactant ratio.

8.2.2 Effect of temperature

The temperature of the reaction was varied between 230 and 320 °C while maintaining the pressure constant, and the catalyst was tested under both dark and light conditions. When illuminated with visible light, CO production was enhanced over the entire temperature range. Figure 8.5 shows that the enhancement of the rate decreased as the temperature was increased from 230 °C to 320 °C. These results suggest that the plasmonic effect becomes less dominant as the temperature rises. At 230 °C, the most significant photo-enhancement of CO production was observed. All subsequent experiments were therefore performed at this temperature. Furthermore, irradiation with visible light allows a lower reaction temperature to achieve the

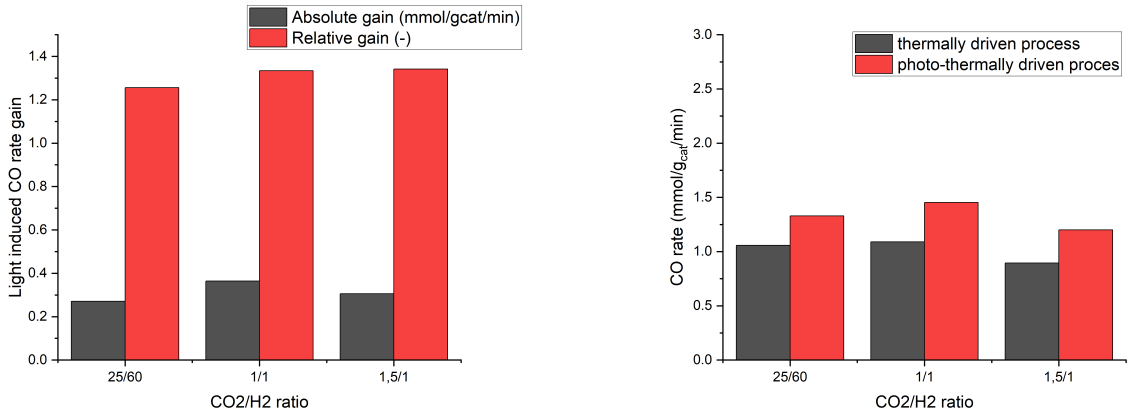

(a) **(b)**

Figure 8.4. Dependence of CO rate enhancement on CO_2/H_2 ratio in photo-enhanced RWGS reaction over CZA catalyst: (a) CO rate at different CO_2/H_2 ratios under dark and light conditions; (b) absolute and relative enhancement of CO rate under dark and light conditions. Experimental conditions: T=300°C, p=1 bar, total flow rate = 30 mL/min, catalyst amount = 22 mg.

same CO yield compared to performance in the dark. In order to determine whether photon-induced charge carriers contribute to the increase in reaction rate, the calculation of the activation energy is a useful method. A reduction in activation energy under light irradiation is typical of a hot carrier driven mechanism, where electrons produced on accessible unoccupied adsorbate orbitals can activate the CO_2 reactant by forming transient negatively charged ions or polarised species, reducing the activation energy for the overall RWGS reaction. Figure 8.5(d) shows the calculated apparent activation energy for the RWGS reaction, which decreased from 83 to 50 kJ/mol under irradiated conditions. This decrease can be explained by a mechanism whereby the electrons generated by the Cu LSPR (or potentially transferred from excited ZnO) transiently occupy the orbital states of the surface CO_2 to promote its activation and subsequent processes, before decaying into thermal energy in the lattice [1].

8.2.3 Effect of illumination power

The rate of chemical transformation in a photochemical process in plasmonics, such as near-field enhancement of photochemical reactions or hot carrier-assisted redox reactions at the nanoparticle surface, is proportional to the rate of incident photons and thus to the incident light power applied to the sample. The case of a photothermal process, however, is different and is not expected to show such a linear dependence. To a good approximation, the temperature rise caused by absorbing light is also proportional to the incident optical power. However, the rate constant k of a chemical reaction typically follows an Arrhenius-like temperature dependence: $k = A\exp(-E_a/RT)$, (where R is the gas constant, T is the absolute temperature, E_a is the molar activation energy and A is the pre-exponential constant factor). As a result the rate of chemical transformation will follow an exponential dependence on the power of the illumination. Figure 8.6 shows the relationship between the rate of CO production and the light power in the range 0-0.77 W. The reaction rate shows a nearly linear relationship, indicating a charge carrier driven reaction. This suggests that excited electrons can efficiently interact with surface adsorbates and that a photocatalytic mechanism is responsible for the observed photo-enhancement [33],[1].

8.2.4 Effect of the wavelength

Three different band ranges have been tested: 400–450 nm, 500–600 nm, and 600–700 nm through the employment of optical filters. The 400-450 nm range was used to excite the ZnO band gap (3.2 eV), while the

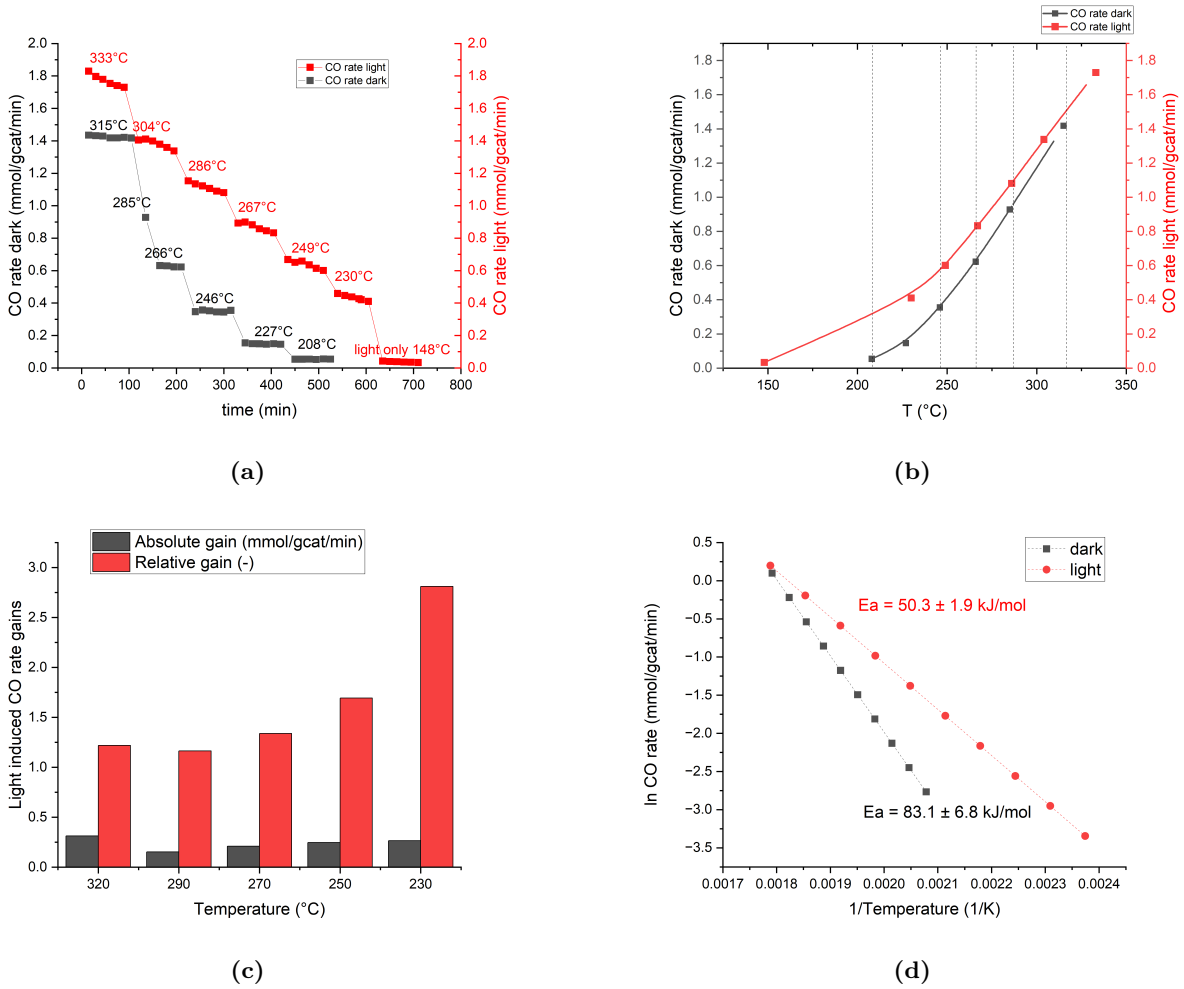

Figure 8.5. Temperature dependence of CO rate photo-enhanced reverse water gas shift reaction over CZA catalyst: (a) CO rate at different temperatures under dark and light conditions over time; (b) CO rate over a temperature range of 230-320 °C; (c) absolute and relative enhancement of CO rate under dark and light conditions; (d) calculated activation energies for the RWGS reaction under dark and light conditions (Arrhenius plot). Experimental conditions: p=1 bar, CO_2/H_2=1:1, total flow rate = 30 mL/min, catalyst amount = 22 mg.

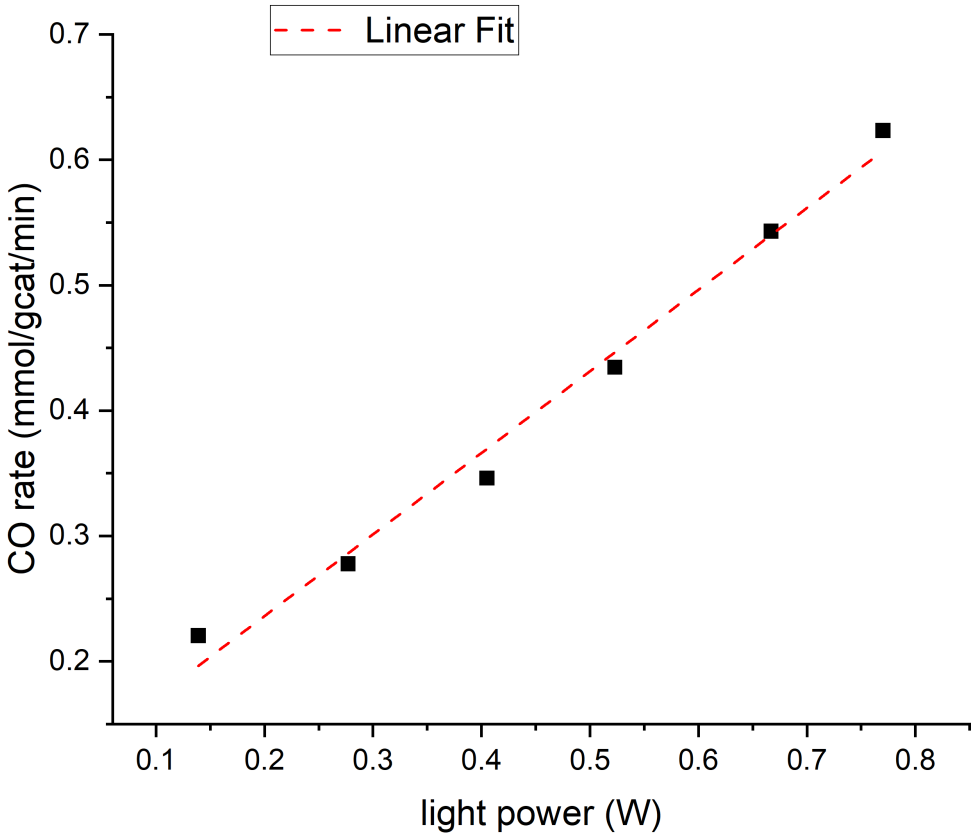

Figure 8.6. Power-dependent photothermal CO production rate, showing a near-linear relationship between rate and light intensity ($R^2 = 0.987$). Experimental conditions: T=230°C, p=1 bar, CO_2/H_2=1:1, total flow rate = 30 mL/min, catalyst amount = 22 mg.

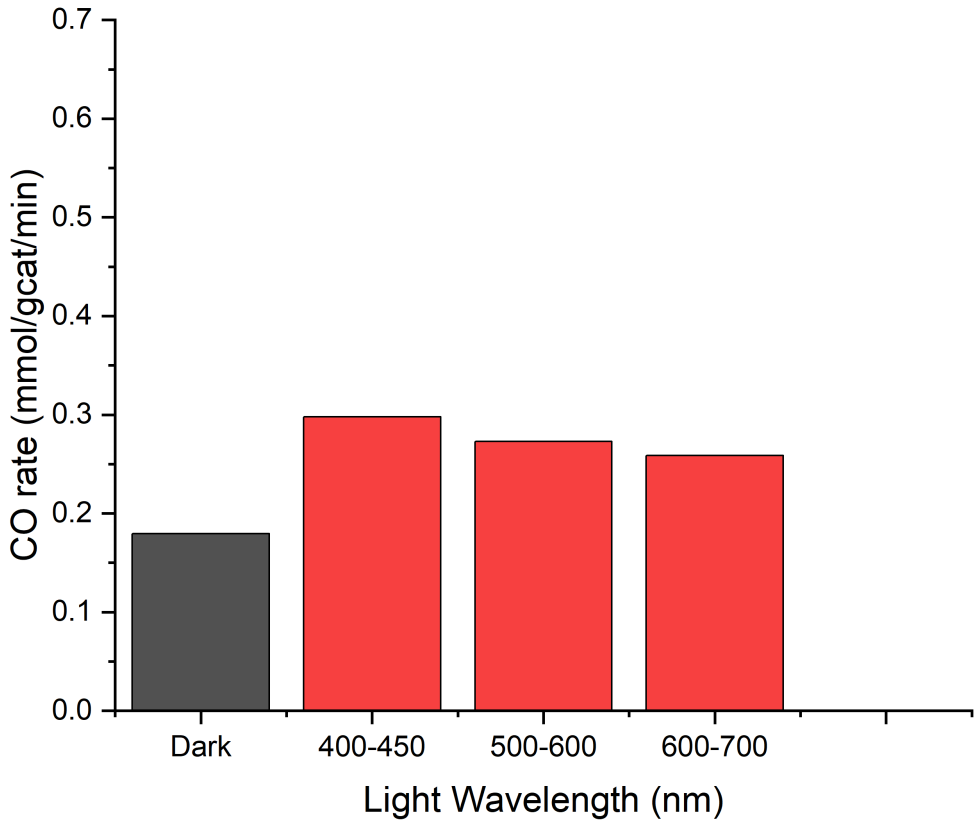

Figure 8.7. Wavelength dependence of CO rate photo-enhanced reverse water gas shift reaction over CZA catalyst. Experimental conditions: T=230°C, p=1 bar, CO_2/H_2=1:1, total flow rate = 30 mL/min, catalyst amount = 22 mg, light power = 228 mW.

500-600 nm range was used to cover the Cu LSPR. CO production was enhanced under all three irradiation conditions compared with the dark results (Figure 8.7). However, while the sample temperature remains constant, the graph shows that different illumination wavelengths result in different chemical rates. This suggests that photon energy also plays a role, as the increase in photochemical rate cannot be explained by optical heating alone. In particular, as the photon energy decreases (i.e. the wavelength increases), a decrease in the CO photochemical rate is observed (Figure 8.7). Throughout the experiment, the intensity of the light source incident on the catalyst bed was maintained at a level of approximately 228 mW. In fact, the temperature of the reaction and the intensity of the irradiation are both maintained constant for the reactions to guarantee that the effect of the external heating on each reaction remains the same. Spectral dependence analysis distinguishes between energetic electron mediated reactions and plasmon-induced heating reactions. Indeed, the dependence of the photoreaction spectrum on the irradiation wavelength provides further evidence for the electron-driven reaction pathways.

The experimental results of the CO rate were used to calculate the apparent quantum yield for the three different wavelength ranges of light tested:

$$AQY = \frac{\text{number of electrons in the reaction}}{\text{number of incident photons}} \times 100 \tag{8.3}$$

that is, expressed as a percentage at each wavelength, the number of product molecules produced by each photon absorbed by the metal NPs. The number of electrons is calculated from the difference between the CO rate in light conditions and the one produced in the dark at the same temperature, so that AQY directly measures only the influence of light. The calculated values are given in Table 8.1.

Wavelength range (nm)	AQY (%)
400-450	10.6
500-600	6.5
600-700	4.7

Table 8.1. Calculated wavelength dependence of the photocatalytic AQY

The photocatalytic performance of a metal nanoparticle is expected to follow its light absorption spectrum, i.e. the higher the light absorption, the greater the photocatalytic activity. However, the results presented above demonstrate that shorter wavelength photons are more effective in driving the reaction. The mismatch between the AQY spectral dependences and the most intensive light absorption of metal NP catalysts (plasmonic resonance at approximately 590 nm) directly demonstrates that the primary driving force of direct photocatalysis in this case is not a simple photothermal effect. Indeed, the rate of direct photocatalytic conversion at each wavelength is determined not only by the photocatalyst absorption spectrum but also by the energy level of the relevant reactant molecular orbitals, suggesting the existence of an energy threshold for inducing carbon dioxide bond cleavage. The alignment of energy levels between the hot electrons (and hence photons) and the molecular orbitals of the reactants determines the threshold energy of photons involved in hot electron transfer reactions. This suggests that shorter wavelengths are necessary to produce a substantial population of hot electrons with enough energy to transfer to the LUMO of CO_2. The excitation of the LSPR is the collective excitation of the conduction electrons of metal nanoparticles by the resonant incident light. Importantly, the number of hot electrons excited by LSPR can differ significantly from the number of photons of incident light. It is reasonable to assume that the LSPR effect generates more hot electrons per unit of absorbed light energy than single-photon excitation. However, the energy levels of the hot electrons generated by the LSPR effect are lower, which limits their ability to induce reactions with high-energy thresholds. As shown in Figure 8.8, the majority of the hot electrons that are excited by LSPR absorption cannot transfer to the LUMO due to insufficient energy. As a result, the long wavelength exhibits a lower AQY compared to the shorter wavelength. This is because the shorter wavelength can produce more hot electrons at higher energy levels than the longer wavelength [17].

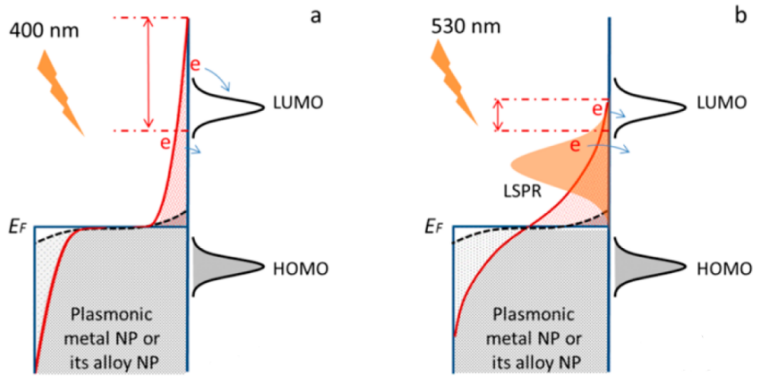

Figure 8.8. Distribution of hot electrons in a plasmonic metal under irradiation of different wavelengths. (a) Short-wavelength (400 nm) absorption occurs via single-electron excitation, also known as interband excitation. Only hot electrons that lie above the LUMO level (area between two red dashed lines) are likely to contribute to the AQY. (b) Irradiation at the plasmonic wavelength (LSPR absorption, 530 nm in this example) results in a much smaller hot electron distribution area above the LUMO level compared to the first case [17].

8.3 Kinetic analysis

Examinations conducted on copper surfaces [69] and supported Cu/ZnO systems [70] have concurred that the reaction orders, and consequently the rate-limiting step, exhibit variations under different reaction conditions. By investigating the dependence of the reaction rate on the CO_2 and H_2 concentrations, the study aimed to gain insight into how visible light irradiation affects the reaction mechanism. Although the reaction orders are not the only determinants, they may provide a useful insight into the atomistic origin of the reaction mechanism. Figure 8.9(a) illustrates the relationship between the reaction rate and CO_2 concentration under dark and light conditions, while maintaining a constant H_2 concentration. The reaction order with respect to CO_2 remains relatively constant, changing only slightly from 0.89 to 0.81. These values, close to unity, suggest that the rate of the RWGS reaction here may be limited by the dissociation of CO_2 under both dark and light conditions [56]. However the changes that occur upon illumination are mainly related to the reactivity with respect of H_2, as the order of its reaction is shifted from 0.7 to -2.6 (Figure 8.9(b)). The results can be interpreted using Hougen-Watson heterogeneous catalytic reaction models based on Langmuir adsorption. According to this model, a reaction order of less than 1 is indicative of the presence of adsorbed surface species that inhibit the rate of the reaction. The decrease in reaction order with respect to H_2 in the presence of light suggests an increase in inhibition by surface coverage of adsorbed H* species, also known as hydrogen poisoning: molecularly adsorbed H_2 is present in concentrations sufficient to have a significant poisoning effect on surface sites. This can be explained by the LSPR excitation of the Cu, which induces a higher catalytic performance for the H_2 cleavage on the Cu, thus improving the H* supply at the catalyst surface [2].

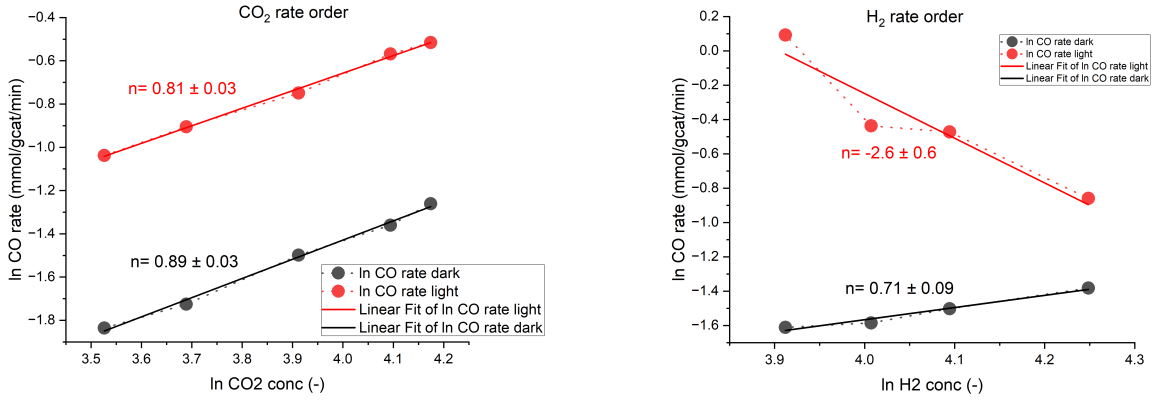

(a) **(b)**

Figure 8.9. Dependence of CO production rate in photo-enhanced RWGS reaction on (a) CO_2 concentration and (b) H_2 concentration under dark and light conditions over CZA catalyst. Experimental conditions: T=230°C, p=1 bar, total flow rate = 40 mL/min, catalyst amount = 22 mg, flowrate of the other reactant kept constant at 11.4 mL/min for H_2 and 12 mL/min for CO_2 using N_2 as an inert gas

8.4 Desorption test through mass spectroscopy analysis

Gas analysis by mass spectrometry (MS) is a technique in which a charged ion is produced from a chemical species (atomic or molecular) in the gas phase and the mass-to-charge ratio (m/z) is measured. The technique uses a family of instruments and is widely used in various fields of research. Typically, ionisation and measurement take place in a vacuum and therefore the samples must consist of permanent gases or volatile species, where larger molecules are required to use alternative vaporization-ionization methods. As each empirical molecular formula has a different mass, this method has the potential to both identify and quantify the components within a sample. There are two typical applications for gas mass spectrometry: static analysis and continuous analysis. Static analysis involves measuring a fixed or static gas volume and assembling a

plot of signal intensity versus m/z value for each species in the gas. Fragmentation can complicate data interpretation in some cases. Static analysis is used for both the qualitative and quantitative analysis of the composition of individually collected samples. Continuous analysis involves monitoring specific m/z values (when analytes are known) or repeatedly scanning the instrument across an m/z range. The output is usually a plot of analyte m/z versus time or total ion signal (per scan) versus time. This method can be either qualitative or quantitative and is commonly used in applications such as reactions, industrial processes and environmental monitoring. All gas mass spectrometers require the same common functions to perform an analysis: sample introduction, ionization, mass separation and detection (Figure 8.10, 8.11) [18].

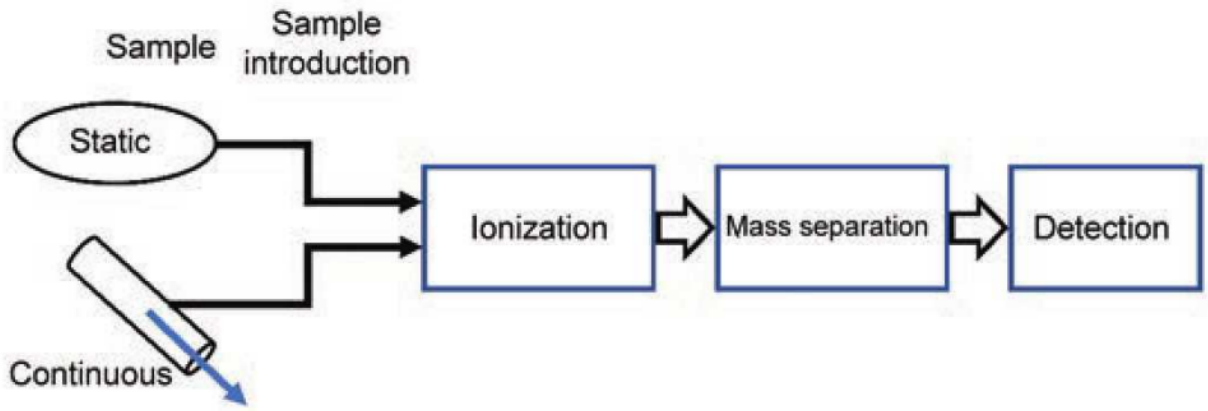

Figure 8.10. Schematic of the functions of a gas mass spectrometer [18]

8.4.1 Ionization Source

The ionization source converts the neutral species of the analyte into charged species that can be manipulated by means of magnetic or electric fields for mass analysis. Plasmas, lasers and surfaces under vacuum or atmospheric pressure are used in research environments for ionisation techniques. In the context of gas analysis, the two primary methods in widespread use are electron ionization (EI) and chemical ionization (CI). Proton-transfer reaction (PTR) is a specific variant of CI that is currently experiencing increased usage. Electron ionization is the most commonly used method for producing positive ions of analyte species within the ionization region (Figure 8.11). Electrons are generated by passing a current through a tungsten or rhenium filament, which are then accelerated and focused into a beam that penetrates the cloud of neutral gas supplied into the vacuum by the sample introduction system. Consistent fragmentation of the analyte species is achieved with a kinetic energy of 70 eV, which is the standard condition for ionization peak. This enables spectral comparison between systems and identification through standard libraries. In certain situations, using a lower energy level can decrease fragmentation, but this may also lead to lower ionization efficiency and subsequently, a weaker signal. The electron energy is adequate for interacting with neutral atoms and molecules, causing the removal of an electron and producing a positive analyte ion through the following reactions:

$$\text{analyte} + \text{e}^- \longrightarrow [\text{analyte}]^+ + 2\,\text{e}^- \tag{8.4}$$

$$\text{analyte} + \text{e}^- \longrightarrow [\text{analyte}]^{2+} + 3\,\text{e}^- \tag{8.5}$$

Analyte fragmentation produces a charged fragment ion species (fragment) and a neutral product (neutral) during the reaction:

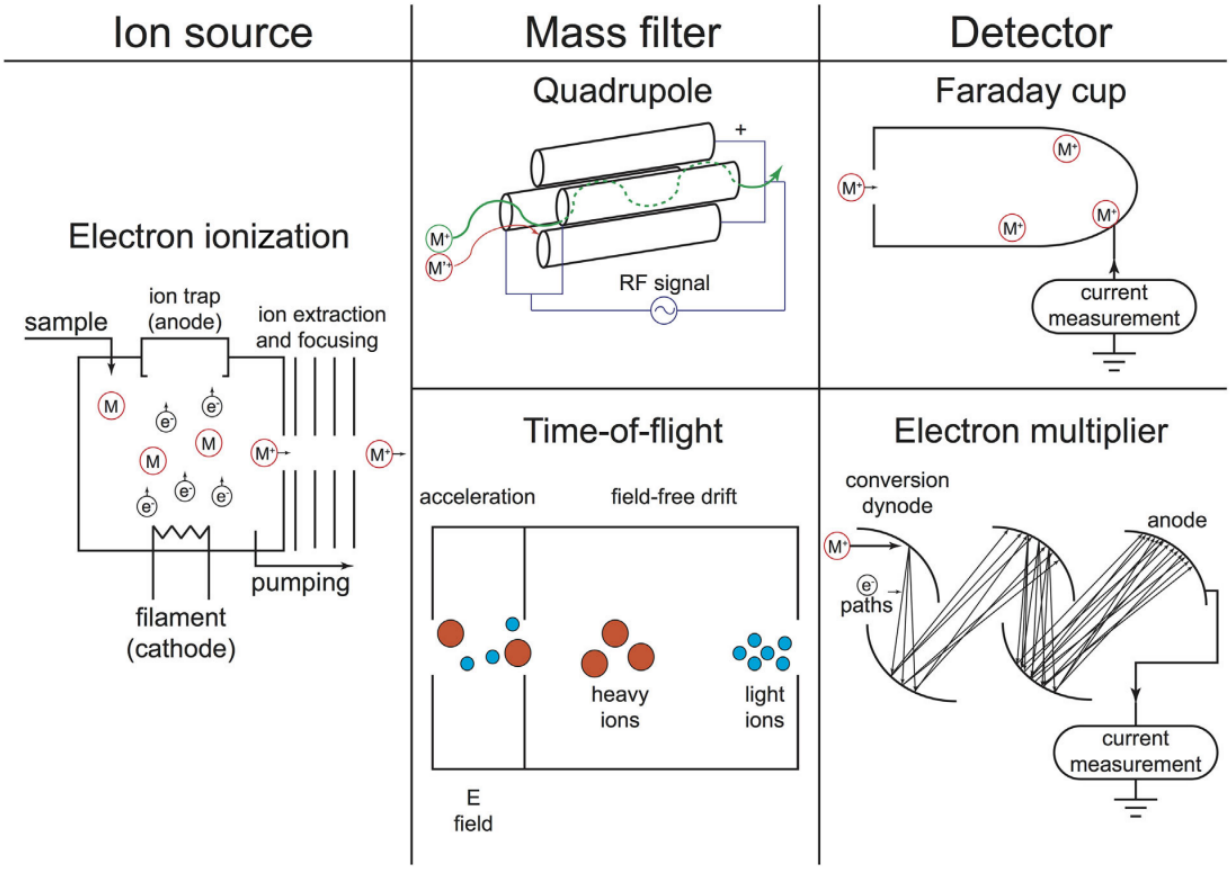

Figure 8.11. Components of a gas mass spectrometer [19]

$$\text{analyte} + \text{e}^- \longrightarrow [\text{fragment}_1]^+ + \text{neutral}_1 + 2\,\text{e}^- \tag{8.6}$$

Due to the distribution of energies in the electron cloud, other fragmentation pathways may also occur, generating fragment_2, fragment_3, etc.. Although some species have low ionization probabilities, EI is still regarded as a universal ionization method.

The aim of chemical ionization (CI) is to reduce the likelihood of fragmentation by reducing the excess energy of the ionization process. The result may be an increase in signal as the analyte signal is no longer split between the $[\text{analyte}]^+$ and a certain number of fragments $[\text{fragment}_n]^+$. The implementation of CI typically involves the use of electron ionization EI or other methods to produce a reagent ion which then interacts with the analytes to produce a charged analyte. Proton transfer reaction (PTR) ionization is a specific version of CI that limits the reaction to proton transfer only:

$$\text{analyte} + \text{H}_3\text{O}^+ \longrightarrow [\text{analyte} + \text{H}]^+ + \text{H}_2\text{O} \tag{8.7}$$

Both CI and PTR offer the advantage of being able to tune this reaction by using different reagents to achieve selectivity. To simplify data and increase sensitivity, a single species in a mixture can be ionized. For known targets, CI and PTR are commonly used. PTR instruments utilise alternative reagent ions, such as NO^+ and ${O_2}^+$, to selectively react with specific analyte targets [18].

8.4.2 Mass Analyzer

Mass analyzers utilize static or dynamic electric and/or magnetic fields to separate ions depending on their mass-to-charge ratio (m/Z). Scanning analyzers measure the m/Z ratios individually, while simultaneous analyzers measure them all simultaneously. The performance parameters comprise:

- mass range (m/Z);
- acquisition frequency (referred to the number of mass scans obtained per unit of time);
- trasmission efficiency of ions reaching the detector;
- mass accuracy, which is the difference between the theoretical and measured values;
- resolution (referred to the ability to distinguish between ions with similar m/Z values);
- sensitivity.

Along with magnetic sector instruments, the quadrupole mass filter is a member of the scanning family of analyzers. Quadrupole mass analyzers (QMA) are relatively inexpensive and easy to operate, but they have comparatively low resolution. The device consists of four circular or hyperbolic parallel rods which separate according to the stability of the ion trajectory in the space between them (Figure 8.11). A dynamic electric field is generated by a high frequency alternating current superimposed on a direct voltage between pairs of opposing rods. The field frequency is chosen so that only ions with a narrow m/Z ratio pass through a transmission QMA filter. All the other ions have an unstable trajectories and lose their charge upon impacting the rods. In less than a minute, a QMA can scan the full spectra, but it can also repeatedly measure a single mass in under 100 milliseconds. Time-of-flight (TOF) analyzers are simultaneous analyzers that assign m/Z ratios on the basis of the transit time of the ions to a detector after they have been ionized (Figure 8.11). All ions have the same kinetic energy after being accelerated by a static electric field. However, lighter ions move faster and drift in a fieldless flight chamber under high vacuum, arriving at the detector at different times depending on their m/Z. In comparison to QMAs, TOFs have slightly lower resolution but significantly higher acquisition rate - of up to 500 full spectra per second - and produce a continuous spectrum [19].

8.4.3 Ion detection

Detectors produce an electrical current from incoming ions in proportion to their abundance. Point detectors count ions at a fixed point in space. They either send only a narrow m/Z range to that point (QMA) or separate the arriving ions in time (TOF). In contrast, array detectors count multiple m/Z ratios at the same time over a specific region in which the mass analyzer separates the ions in space. The Faraday cup is a simple point detector that consists of a metal cup with a small opening on the other side that is connected to the vacuum of the mass analyser (Figure 8.11). When the grounded surface of the cup neutralizes the ion beam, the detector generates a direct current. The effectiveness of the cup in preventing ion reflection and secondary electron ejection determines its accuracy. The reduction of these phenomena can be achieved by improving the design of the cup geometry, coating, and magnetic field. Faraday cups are less sensitive than other detectors and are a suitable choice for abundant analytes. Secondary electrons are generated when ions collide with the surface of SEM detectors (secondary electron emission). These secondary electrons, in turn, produce more secondary electrons through a cascade effect, resulting in the electron multiplier schematized in Figure 8.11. The current is amplified by discrete dynodes at decreasing negative potential and continuous dynodes (channeltron) with a voltage applied at the two extremities. A current is generated by low frequency collision ions hitting the detector surface, which is then amplified. SEMs scan faster than Faraday detectors but are less accurate. They are best suited to light ions which, due to their high velocity, produce more secondary ions than heavy ions. However, sputtering of the semiconductor-coated surface and contamination limit their lifetime to 1-2 years [19].

8.4.4 Experimental analysis and results

Mass spectrometry was used to continuously monitor the effluent gases from the Harrick reactor in order to gain insight into the reaction mechanisms in both dark and light conditions (Figure 8.12). Initially, the reaction was conducted in the absence of light and a stream of hydrogen (m/Z = 2) in helium (m/Z = 4) was used for the 30-minute reduction stage. A stream of He was then used for the purge stage and then CO_2 was fed to the reactor. Following the switch-off of the CO_2 flow rate, the light stage began and the reactor was then supplied with hydrogen. This is accompanied by a slight increase in the CO signal.

Figure 8.12b shows an enlargement of the red square portion of the graph, to better see and explain the behaviour of the signals of CO_2 and CO from the CO_2 adsorption stage to the H_2 shut-off in light conditions. After CO_2 was added to the reduced and purged catalyst, the curves for carbon monoxides (m/Z = 28 and 29) followed the CO_2 curve. It is important to note that CO_2 (m/Z = 44) may also contribute to these signals, as the m/z=29 ion is shared by both CO and CO_2 during electron ionization in the mass spectrometer. However, the difference between the CO_2 and CO traces provides compelling evidence for the creation of CO [71]. The trend of the CO signals shows that the introduction of CO_2 does not cause the formation of distinct CO peaks, indicating that the redox mechanism is not the main course of the RWGS reaction. Indeed, CO is not produced solely from CO_2 over the catalyst surface. In contrast, as hydrogen approaches the catalyst surface at about 150 min, the CO signal increases from 1.9×10^{-10} to 4.9×10^{-10}. A further purging stage is carried out with He to cause desorption of the adsorbed species and to clean the catalyst surface. Subsequent addition of CO_2 in light conditions does not cause any differences in forming distinct CO peaks compared to dark conditions, confirming the absence of the redox mechanism. The H_2O signal (m/Z = 18) is also visible, but it is much lower compared to the others. As expected, it increases with the introduction of hydrogen into the reactor (Figure 8.12b).

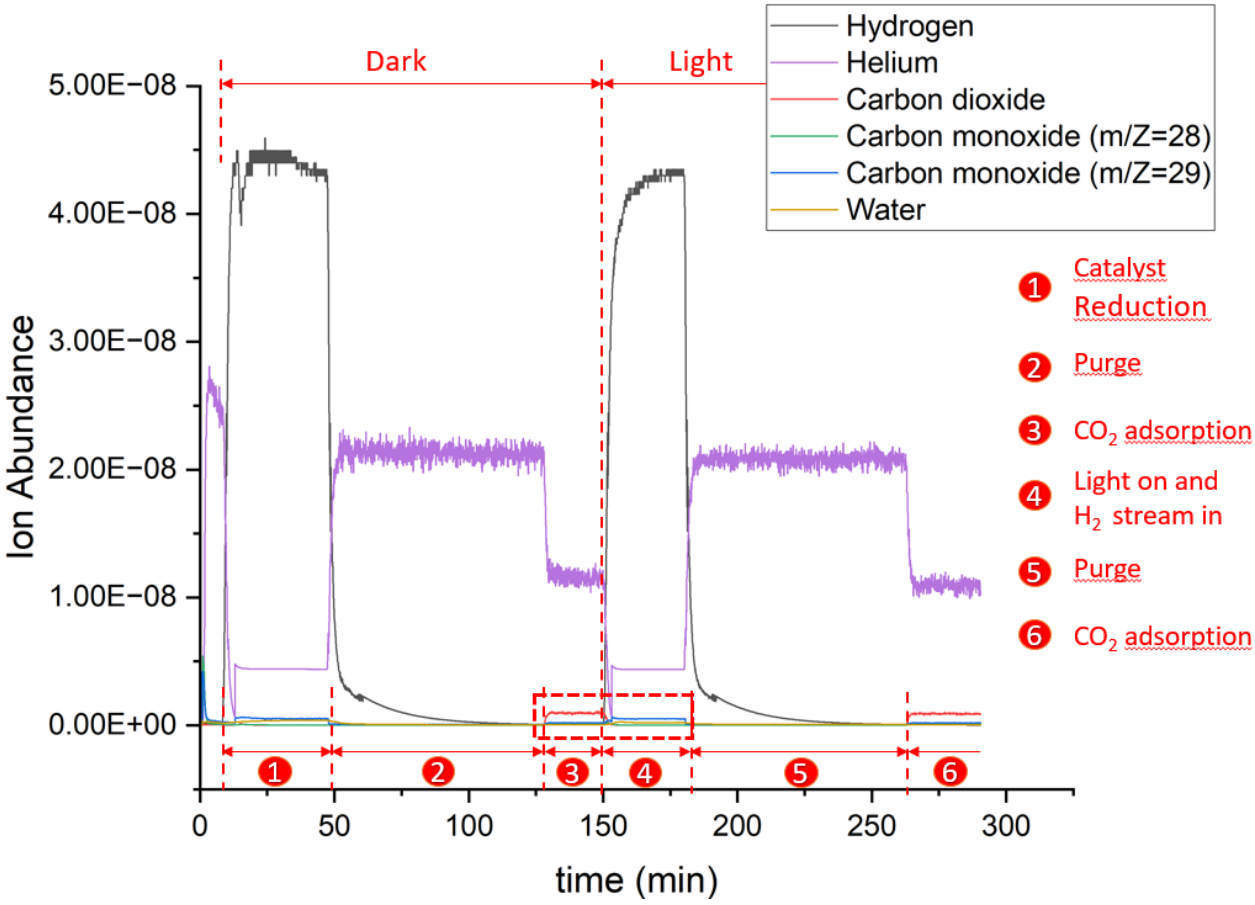

(a)

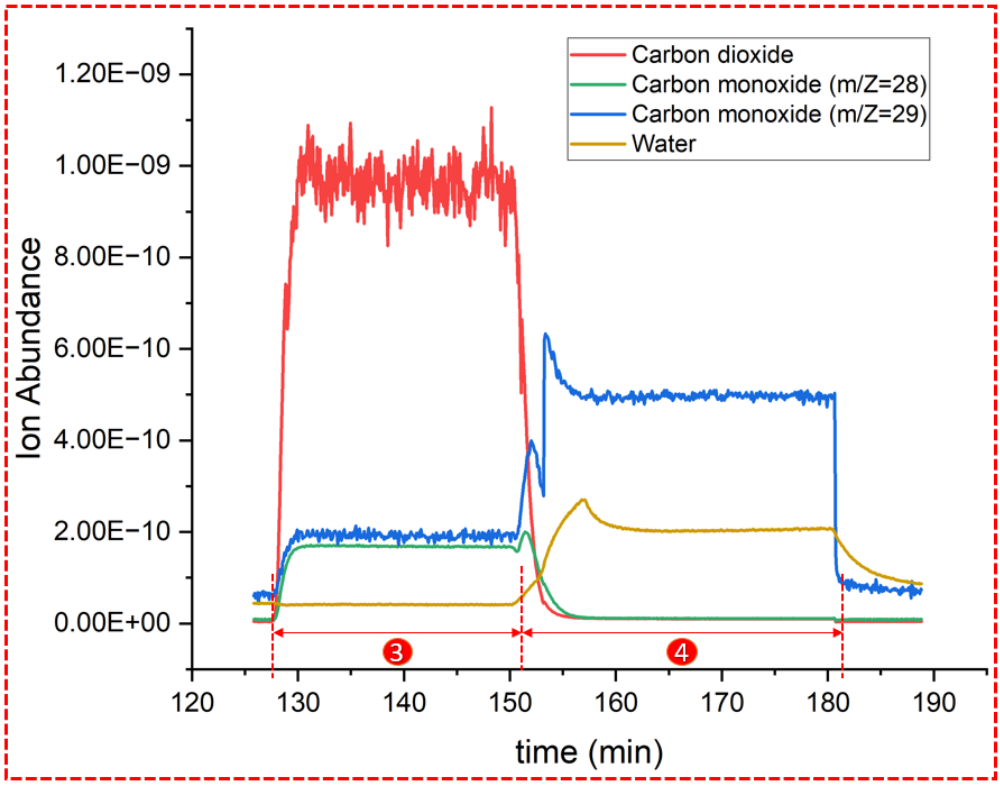

(b)

Figure 8.12. Mass spectroscopy continuous monitoring of the effluent gas of the RWGS reaction. Experimental conditions: p = 1 bar, T = 230°C, total flow rate = 30 mL/min, catalyst amount = 22 mg.

9 In situ spectroscopy

9.1 UV-visible Diffuse Reflectance Spectroscopy

9.1.1 Reflectance of diffusing media

When a beam of light interacts with a material medium (Figure 9.1), it is deflected from the rectilinear path of light expected in a vacuum. According to the laws of geometrical optics, the beam is propagated through the thickness of the medium and undergoes refraction, reflection, diffraction and diffusion as it travels. The interaction depends on various properties of the medium, such as its homogeneity, transparency and surface characteristics (e.g. roughness). The re-emitted beam is then subtracted from the adsorbed portion (subtractive aspect) at each wavelength (selective aspect). The resulting emitted spectrum, consisting of the plot of reflectance values R versus wavelength λ, is the reflectance spectrum. Reflectance, defined as the ratio of reflected to incident incident flux for a given wavelength, is a dimensionless quantity, usually expressed as a percentage. It measures the ability of a surface to reflect incident energy flux, taking into account absorption and diffusion in the underlying medium.

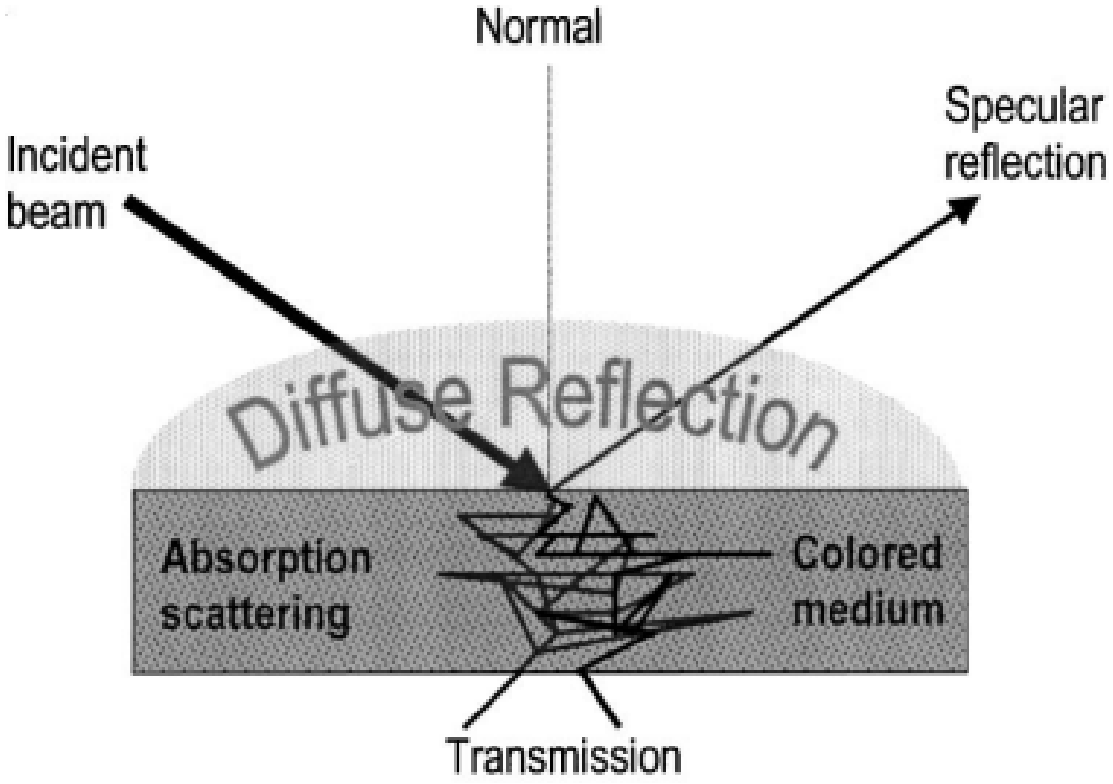

Figure 9.1. Interactions between light and matter [20].

Reflectance is a bidirectional property that is influenced by the direction of light incidence (from the object to the light source) and the direction of observation (from the object to the sensor). Therefore, the diffusely reflected energy flux is always measured in accordance with a known source-object-observer geometry. Natural surfaces often cause diffuse reflections due to their heterogeneity, leading to diffuse reflections distributed in every direction (i.e. scattering). A perfectly matte surface exhibits uniform diffuse reflection in all directions. In contrast with the purely diffusing material, a purely specular material reflects the whole incident radiation

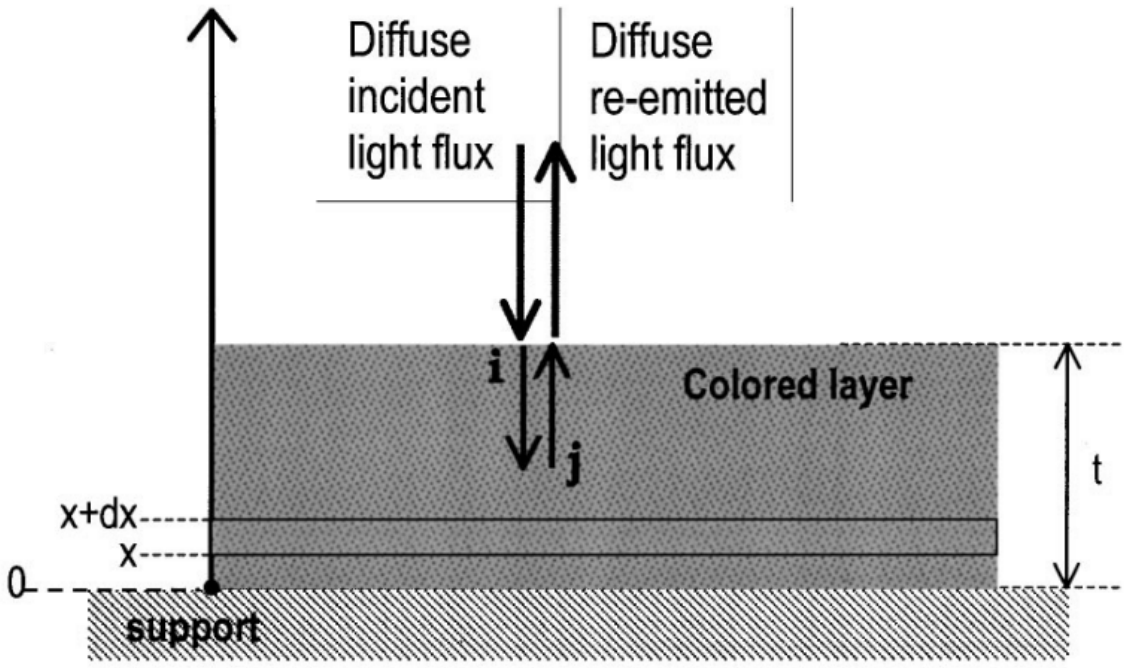

Figure 9.2. Kubelka and Munk's theoretical model scheme [20].

(i.e. a purely smooth one). However, real surfaces consist of both diffuse and specular components. The interaction between light and particles in a medium depends on the size of the particles relative to the wavelength of the incident radiation [20].

9.1.2 Kubelka and Munk's Theory

In 1931, Kubelka and Munk proposed a simplified model for light propagation in a dull painted layer parallel to a plane support, illustrated in Figure 9.2.

Their model focused on considering only two diffuse fluxes, one in the direction of incidence (i) and the other in the opposite direction (j). The scattering phenomenon was conceptualised as a reversal of the direction of the light flux, and geometric variations in the light distribution through the coloured layer were ignored. Assumptions included isotropy and homogeneity of the medium, with optical heterogeneities assumed to be small compared to the layer thickness. Specular reflection was ignored (dull paint) and the boundary surfaces were assumed to be flat, parallel and infinite, eliminating boundary effects. The absorption and scattering coefficients (k and s respectively, measured in inverse meters) were assumed to be constant regardless of the film thickness, and polarisation and spontaneous emission (fluorescence, phosphorescence) were not taken into account. Kubelka and Munk derived a system of two differential equations for an infinitesimal layer dx, which was then integrated over the entire thickness (t) of the coloured material. This integration process provided a simple system of equations that could be applied to obtain reflectance values for a given wavelength, R_∞ for an infinite layer or R for a finite layer. They were expressed in terms of absorption and scattering coefficients and the reflectance of the substrate. In practical terms, R represents the reflectance of a layer thick enough to completely obscure the substrate, and serves as the boundary reflectance, unaltered by any additional thickness of the same material [20]. Furthermore, the calculation of R facilitates the determination of the ratio between absorption and scattering coefficients (k/s) through the use of the Kubelka-Munk function:

$$F(R) = \frac{k}{s} = \frac{(1 - R_\infty)^2}{2R_\infty} \tag{9.1}$$

9.1.3 Experimental results

UV-Vis Diffuse Reflectance Spectroscopy (DRS) is a spectrophotometric technique commonly used for analysing powders and surfaces. It offers the advantage of requiring minimal sample preparation. This method relies on the surface dispersion of a portion of the incident UV-Vis radiation. The procedure requires directing a collimated light beam onto the sample, positioned at an angle, inducing various optical processes that reflect radiation from the sample surface throughout the entire hemisphere above it. The reflected radiation usually appears in two components: regular (or specular) and diffuse (or nondirectional) reflectance. Regular reflectance occurs when radiation strikes a smooth and planar surface of the sample, and is reflected at an angle equal to the angle of incidence. In contrast, diffuse reflectance results from a combination of optical phenomena, including multiple reflections, scattering, and refraction, which disperse the radiation at all angles within the hemisphere of origin of the incident radiation. The physico-chemical properties and colour of the surface determine the characteristics of diffuse reflectance, making it the most informative component in this spectroscopic technique. To assess the spectral characteristics, the percentage reflectance, was determined. This parameter was specifically measured over the wavelength range (λ) of the incident UV-Vis radiation, resulting in reflectance spectra. The instrumental parameters for these measurements included a wavelength range of 800 - 200 nm, a resolution of 1 nm [72]. To improve the interpretation of the data, the Kubelka-Munk function spectra was calculated over the UV-Vis DRS spectra (Figure 9.4).

As shown in Figure 9.3, the CuO absorption edge in the UV-vis spectrum at $\sim$ 750nm is absent for the CuSiO2 sample. This proves that the standard reduction of 5% H_2:N_2 at 320°C is sufficient to reduce the CuO crystallites to metallic Cu, which has no band gap. As a result, there is strong absorption over the entire Vis and UV range and a peak appears in the region between 570nm and 590nm , corresponding to the plasmon resonance of metallic copper (LSPR of Cu NPs). For the commercial Hifuel sample, this resonance is much smaller (red oval in the graph), probably because the copper particles in this sample are much smaller (Scherrer analysis). The ZnO adsorption peak at 390 nm is masked by the strong metallic Cu absorption as reported by Stone *et al.* and by Xie *et al.* [64],[1]. Both compounds show strong charge transfer absorption below 400-450 nm, while the stronger absorption band between 250 and 290 nm characterises copper-alumina samples.

9.1.4 Determination of the band gap energy based on UV -Vis Spectra

The band gap energy of a semiconductor represents the energy needed to excite an electron from the valence band to the conduction band. The determination of the band gap energy is typically achieved through diffuse reflectance spectra. In 1968, Tauc proposed an equation for calculating the absorption edges (bandgaps) of amorphous Ge and Si based on their absorption data:

$$(\alpha h\nu)^\gamma = A(h\nu - E_g) \tag{9.2}$$

In this equation, α is the absorption coefficient, h is Planck's constant, ν is the frequency of the incident photon, E_g is the bandgap energy and A is a proportionality constant, determined by the index of refraction, electron and hole effective masses, usually taken as 1 for amorphous materials. The exponent γ is a crucial term indicating the nature of the electronic transition:

- $\gamma = 2$: direct allowed transition
- $\gamma = 1/2$: indirect allowed transition
- $\gamma = 2/3$: direct forbidden transition

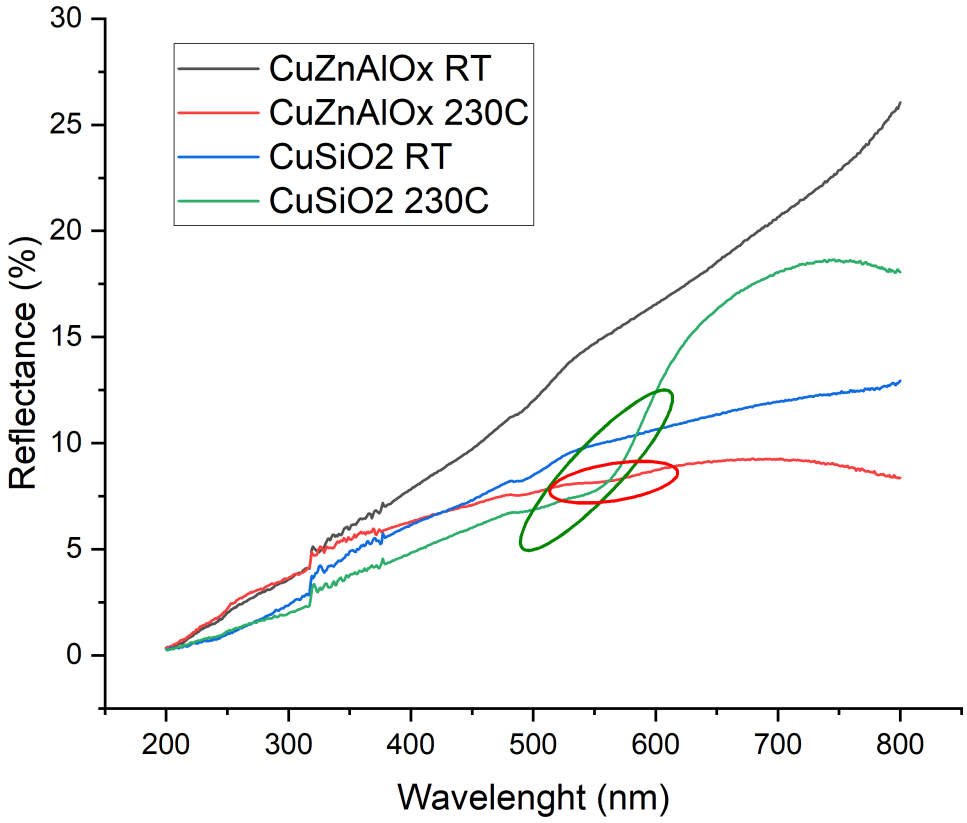

Figure 9.3. UV-vis diffuse reflectance spectra

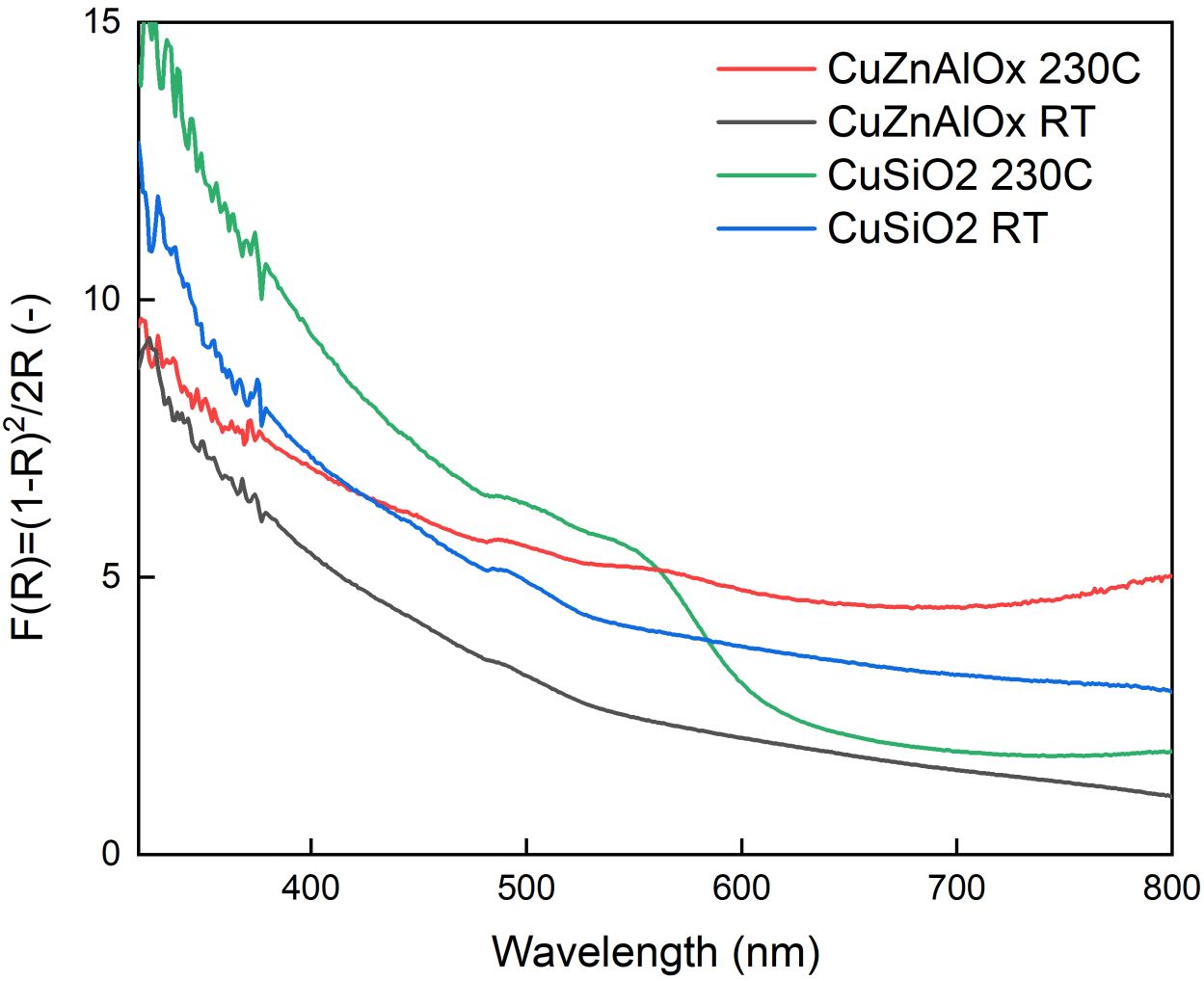

Figure 9.4. Kubelka-Munk function spectra

- $\gamma = 1/3$: indirect forbidden transition

Typically, basic absorption processes are dominated by allowed transitions, leading to either direct or indirect transitions. The Tauc analysis involves obtaining optical absorbance data for a sample covering a range of energies from below the band-gap transition to above it. Plotting $(\alpha h\nu)^{\gamma}$ versus $h\nu$ involves testing $\gamma = 2$ or $\gamma = 1/2$ to determine which provides a better fit, thereby identifying the correct transition type. In accordance with the theory formulated by Kubelka and Munk in 1931, the measured reflectance spectra can be converted into the corresponding absorption spectra by utilizing the Kubelka-Munk function $F(R_{\infty})$. Substituting $F(R_{\infty})$ for α in equation 9.2 results in the following expression:

$$(F(R_{\infty})h\nu)^{\gamma} = A(h\nu - E_g) \tag{9.3}$$

Figure 9.5 illustrates the reflectance spectrum of CuZnAlOx, where a direct band gap transition is considered for ZnO, transformed based on equation (9.2), plotted against photon energy. The segment displaying a pronounced, linear increase in light absorption as energy increases is indicative of semiconductor materials. The point of intersection with the x-axis from the linear fit of the Tauc plot provides an approximation of the band gap energy [73],[74].

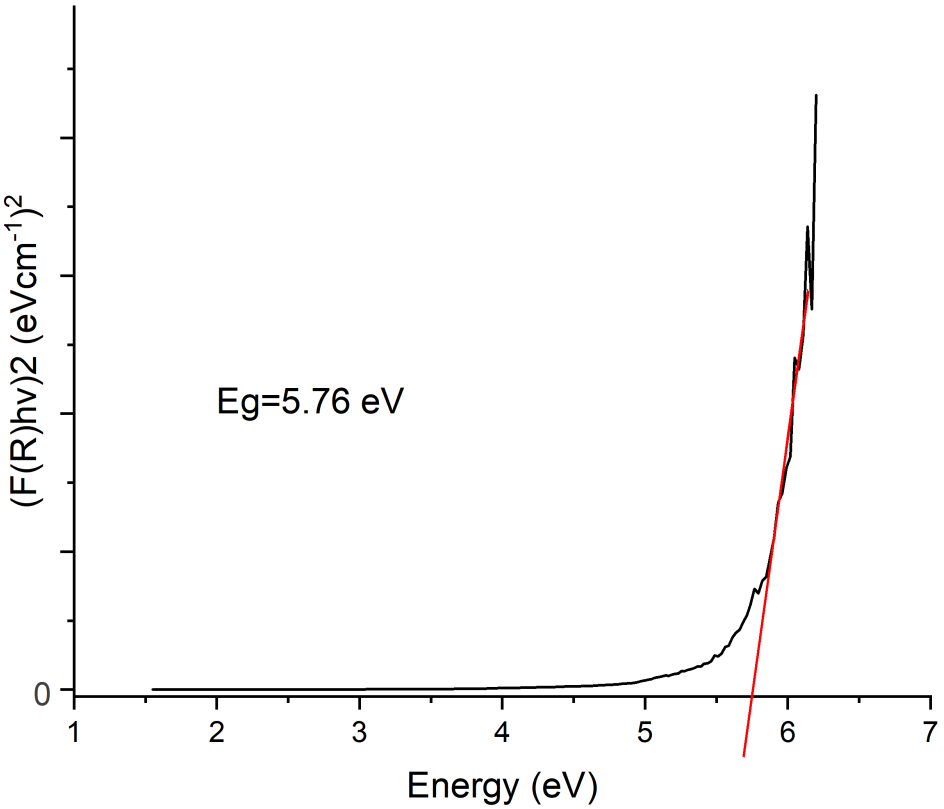

Figure 9.5. Tauc plot from UV–Vis analysis of CuZnAlOx at 230°C that illustrates the fitting of the linear region to evaluate the optical band-gap at the X-axis intercept

As reported above, all CuO has been reduced to metallic copper at 320°C, which has no band gap.

The band gap energy calculation therefore consists of determining the band gap energy of ZnO. Zinc oxide belongs to the group of II-VI compounds with a direct wide bandgap semiconductor ($E_g \sim 3.37$eV) at room temperature [74]. However, Wang *et al.* reported the band gap energy dependence on the length scale of the ZnO nanostructure. In fact, when the size of the semiconducting nanostructures is reduced to the order of the Bohr radius of the bulk exciton (a few nanometres), a quantum confinement effect occurs and the optical properties of the exciton are changed. Theoretically, ZnO nanoparticles can have a band gap above 4.5 eV, but the nanoparticle size must be comparable to or smaller than the ZnO Bohr exciton radius: $a_B \sim 2.3$nm (ZnO quantum dots, QDs), because this significant band gap blue-shift (relative to the bulk one of 3.37 eV) can only be achieved by strong quantum confinement effects. This trend can be theoretically reproduced by expressing the energy of the lowest excited state as a function of the nanostructure size (radius) by the following equation:

$$E_{\text{gap,dot}} = E_{\text{gap,bulk}} + \frac{\hbar^2\pi^2}{2R^2}\left(\frac{1}{m_e^*} + \frac{1}{m_h^*}\right) - 0.248E_{\text{Ryd}}^* \tag{9.4}$$

where $\hbar$ is the Planck's constant, R is the radius of ZnO QDs, m_e^* and m_h^* are, respectively, the effective masses of electron and hole, $E_{\text{gap,bulk}}$ is the bulk ZnO band gap and E_{Ryd}^* is the exciton-binding energy of 60 meV. Based on Equation 9.4, Wang *et al.* obtained the relationship between the size and band gap of ZnO QDs, as depicted in Figure 9.6 [21].

9.2 Infrared Spectroscopy

Infrared spectroscopy is a valuable tool for identifying the functional groups within a given sample. In addition, this technique can sometimes provide information on the spatial proximity of one group to another or on the quantity of the sample under investigation. Molecular constituents exhibit dynamic behaviour as the atoms within molecules vibrate about their equilibrium positions, even in the solid state. The frequency of each atom's vibration depends on factors such as its mass and the length and strength of the bonds it has formed. The excitation of molecular vibrations occurs when the bonds absorb radiation of a frequency aligned with the natural frequency of the bond, typically in the infrared region of the electromagnetic spectrum (specifically in the range of 1.20 x 10^{13} - 1.20 x 10^{14} Hz).

An infrared spectrum is commonly obtained by passing infrared radiation through a sample and determining what fraction of the incident radiation is absorbed at a given energy. For a molecule to exhibit infrared absorption, it must have an electric dipole moment that changes as it moves. The interactions between infrared radiation and matter can be explained by considering changes in molecular dipoles associated with vibrations and rotations. Molecules allow their constituent atoms to move relative to each other, where bond lengths may vary or an atom may deviate from its existing plane (Figure 9.7). These motions, collectively known as vibrations, include stretching and bending. The centre of mass of the molecule remains invariant throughout these modes. Oscillations can involve changes in bond length (stretching) or bond angle (bending). Bonds can stretch either in phase (symmetric stretching) or out of phase (asymmetric stretching). In cases where a molecule has different terminal atoms, the two stretching modes will show different proportions of the stretching motion of each group, leading to symmetric and asymmetric vibrations of similar bonds (coupling). Even relatively simple molecules can have many different vibrations. The complexity of an infrared spectrum arises from the coupling of vibrations that occur over a significant part or all of the molecule, known as skeletal vibrations [75]. For a more manageable numerical representation, absorption is commonly expressed in wavenumbers (units cm^{-1}), which are the reciprocal of the wavelength in centimetres. For most purposes, it is often assumed that each vibration is independent of its neighbours and that atoms behave like simple harmonic oscillators.

Infrared spectroscopy is less sensitive than ultraviolet/visible spectroscopy due to the lower energies involved in the vibration of atoms compared to electronic transitions. However, correctly prepared samples can yield good and reproducible spectra even with small amounts of sample [76].

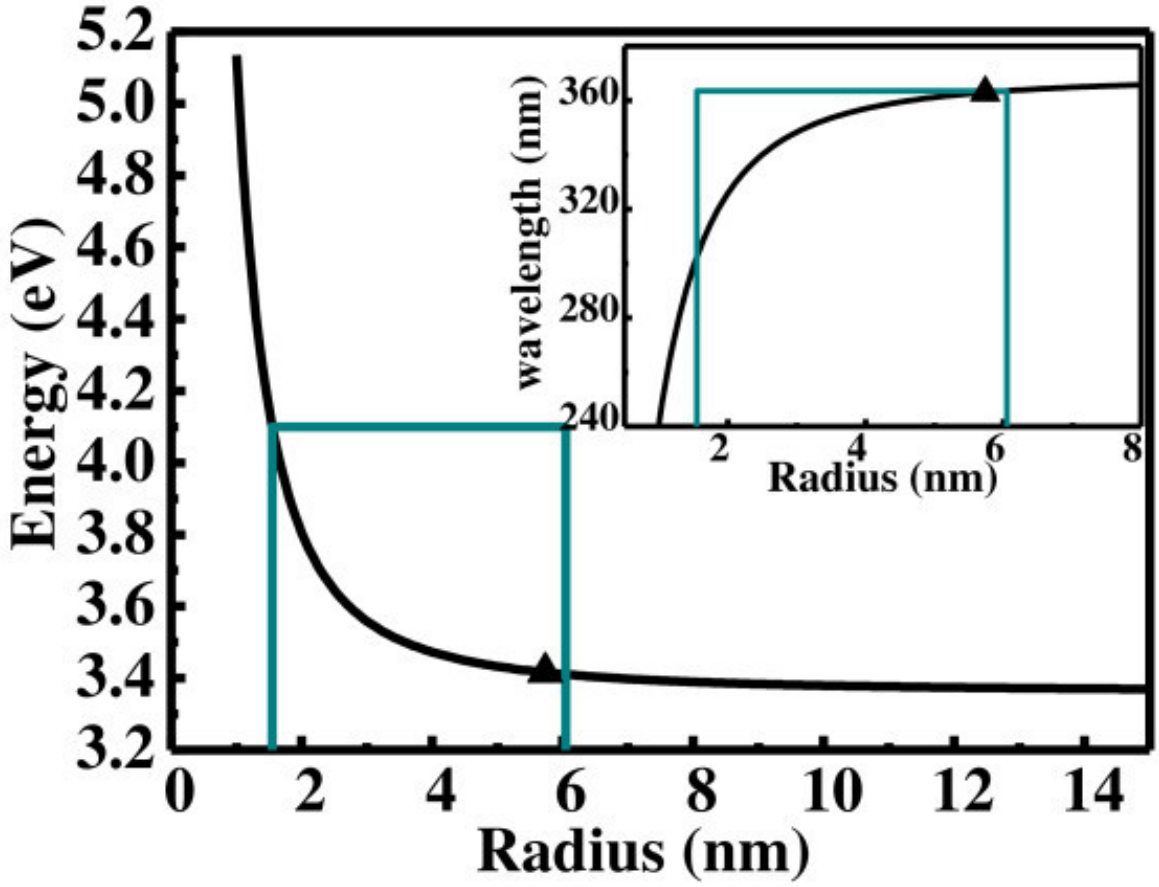

Figure 9.6. The dependence of the band gap on the dimension of the quantum dots according to Equation 9.4 and the inset of the corresponding emission wavelength depending on the dimension of the quantum dots. The triangular mark indicates the energy and wavelength corresponding to the experimental peak of 363 nm [21].

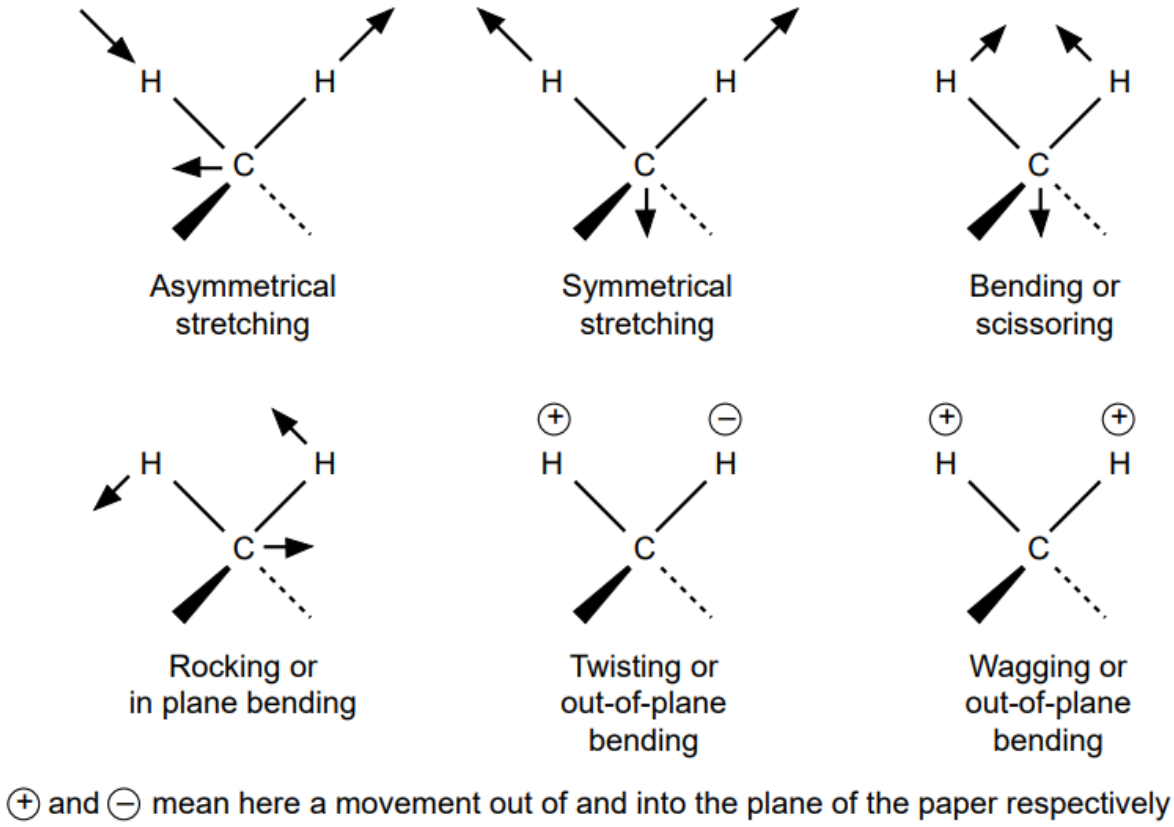

Figure 9.7. Molecular vibrations

9.2.1 The spectrometer

Traditional infrared spectrometers, commonly referred to as dispersive infrared spectrometers, use two radiation beams - one passing through the sample and the other through a reference cell, as shown in Figure 9.8. The infrared source used can range from a simple coil of nichrome wire to a more complex water-cooled silicon carbide rod. Radiation across the frequency spectrum is directed through the sample. As the sample absorbs a particular frequency, less radiation is transmitted and the detector compares the intensity passing through the sample with that passing through the reference. Detection of the radiation passing through the sample or reference cell typically involves a photomultiplier or photodiode, which converts the photons of radiation into tiny electrical currents. Alternatively, a semiconductor cell, which emits electrons when radiation strikes it, is followed by an electron multiplier. Triglycine sulphate (TGS) photocells are commonly used, although a mercury-cadmium-telluride (MCT) cell is preferred for fast scans with a high-sensitivity detector, particularly those performed at liquid nitrogen temperatures. In both cases, the spectrum is generated by contrasting the currents produced by the sample and reference beams. The recorded spectrum, maintained by a data system (typically a computer), is plotted as a function of transmittance (indicating the amount of radiation passing through the sample) against decreasing wave number, corresponding to increasing wavelength [76].

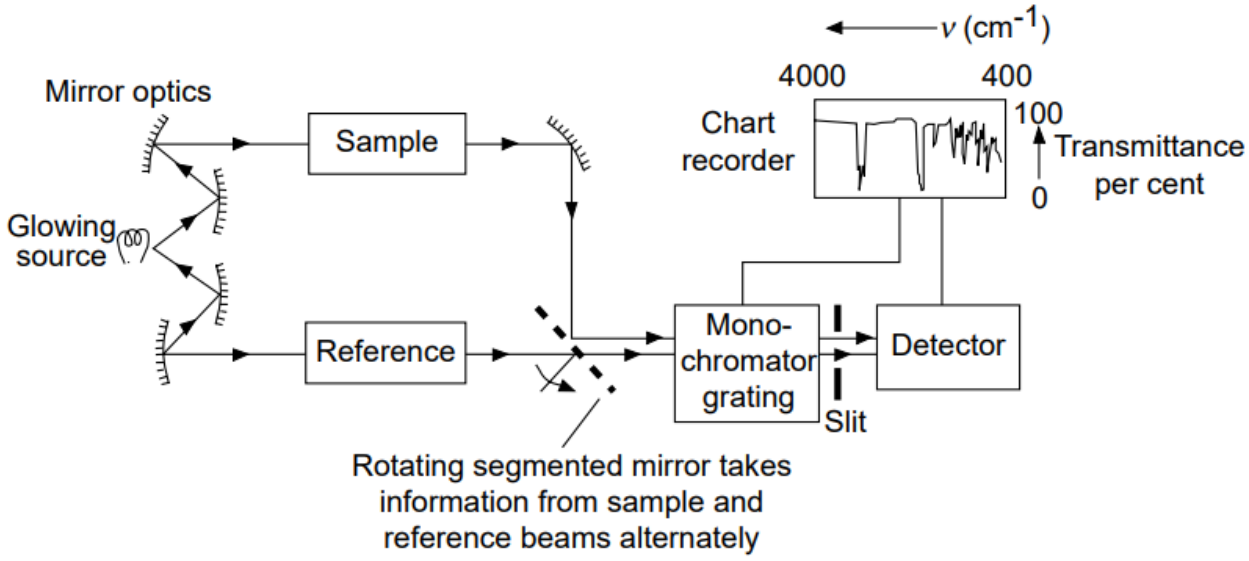

Figure 9.8. The infrared spectrometer

9.2.2 Fourier transform infrared (FT-IR)

In conventional infrared spectroscopy, radiation is passed through both the sample and the reference using a monochromator to select radiation of only one frequency at a time (monochromatic radiation). Fourier Transform Infrared spectroscopy uses only one beam, allowing all the required frequencies to pass through the instrument simultaneously. A computer interprets the resulting information through a Fourier transformation and plots the spectrum. Although the spectrum obtained by FTIR may differ slightly from that obtained by conventional scanning, these variations are usually considered insignificant. FTIR has several advantages over conventional infrared spectroscopy [76]:

1. the entire spectrum can be acquired in a few seconds as opposed to several minutes with conventional methods
2. the faster scan speed allows spectra of compounds to be obtained as they leave a chromatography column, without the need for prior collection

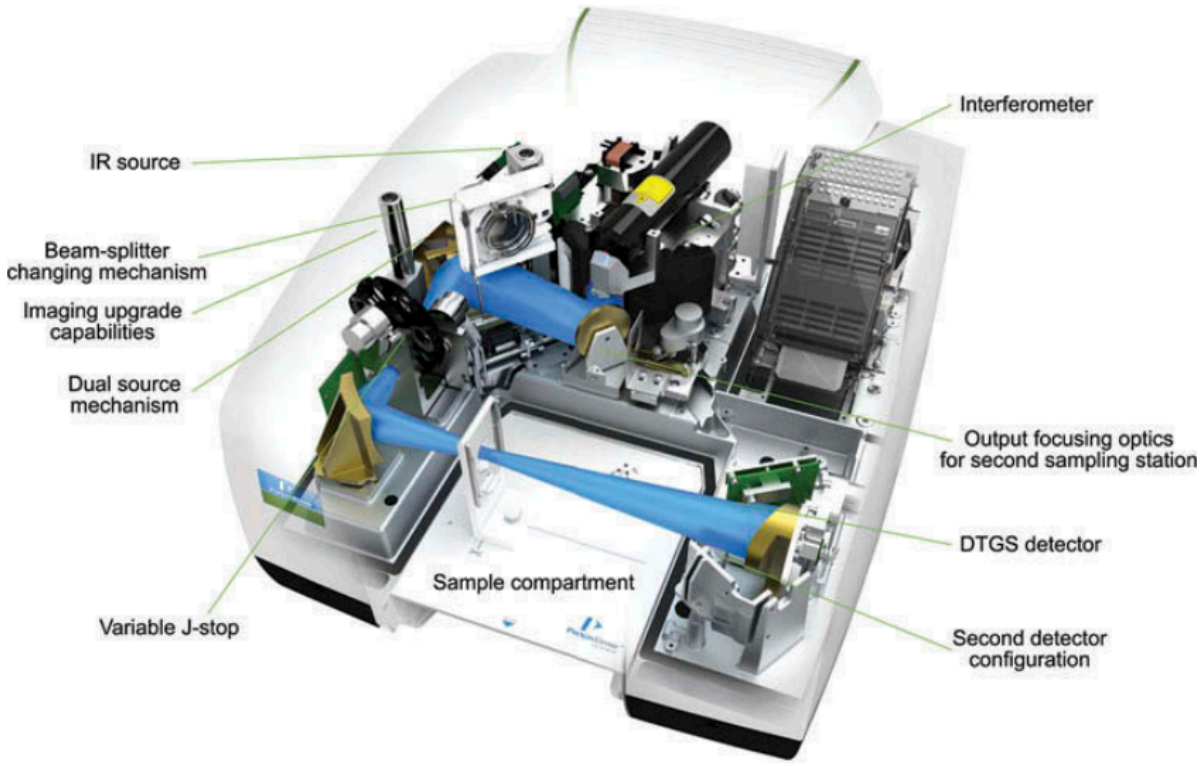

Figure 9.9. Photo of a PerkinElmer Frontier benchtop FTIR spectrometer [22].

3. increased sensitivity is achieved by significantly reducing background noise
4. removal of solvent or known impurity spectra from the observed spectrum is facilitated because the information is first converted to a digital signal, allowing a computer to subtract one spectrum from another
5. for a small sample, a spectrum can be generated by combining information from multiple scans to produce a single, comprehensive spectrum

9.2.3 Experimental analysis and results

DRIFTS (diffuse reflectance infrared Fourier transform spectroscopy) experiments were conducted to investigate the adsorption of CO2 on the CZA catalyst under reaction conditions of 230°C and 1 bar, in both dark and light conditions. The aim was to identify possible reaction intermediates and spectator species that could provide mechanistic clues. The tests were performed using a PerkinElmer FTIR spectrometer (Figure 9.9) equipped with a DTGS detector cooled with liquid nitrogen and an IR cell in praying mantis geometry (VCDRM-5, Harrick), as schematized in Figure 9.10. The catalyst illumination was carried out using a Led Schott KL2500 at 100% power. The spectra were recorded in absorbance mode with a resolution of 4 cm^{-1} and an average of 16 accumulations per scan.

The CZA sample was placed on the temperature-controlled sample holder in the IR cell. The sample compartment was then flushed with Ar to remove any impurities before spectra collection. Next, the catalyst was activated by flowing H_2/Ar gas mixture in a 2:1 ratio for 30 minutes at a total flow rate of 30 mL/min. To characterize the behaviour of CO2 adsorption, the sample was cooled to 230°C after activation and background acquisition. The sample was exposed to a 1:1 flow of 20 mL/min CO2/He, in addition to the 10 mL/min hydrogen flow, for 60 minutes for the RWGS reaction studies. The CO_2/He flow was shut off, followed by the introduction of an argon stream at a rate of 20 mL/min. This caused the carbon dioxide to

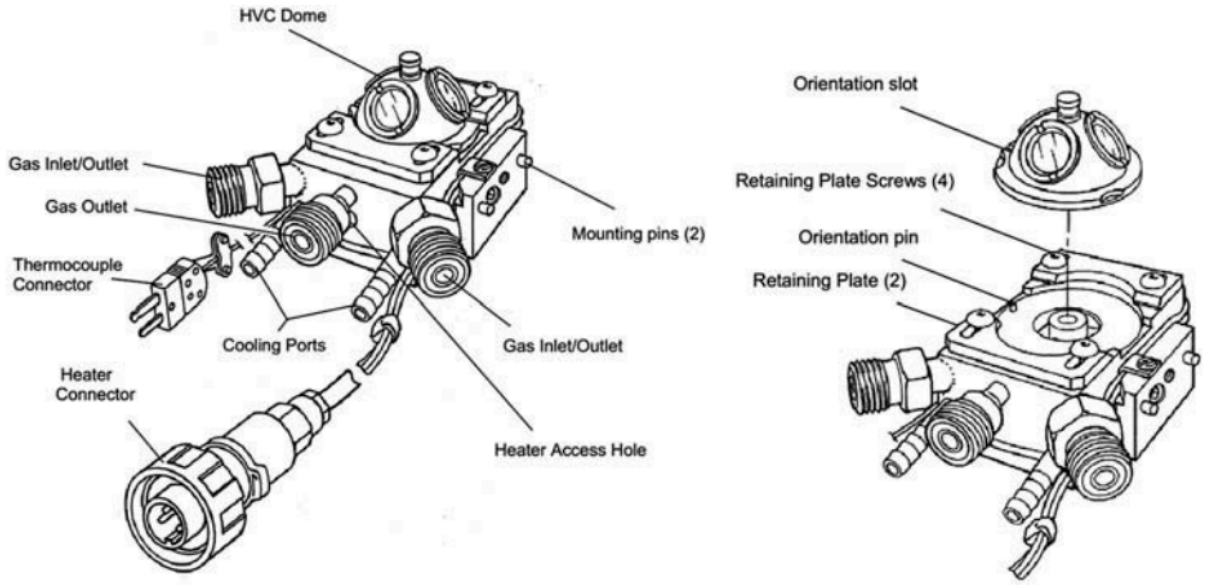

Figure 9.10. Interior view of the Praying Mantis diffuse reflectance accessory [22].

be evacuated and the adsorbed intermediates to be desorbed. A needle valve was used to switch between the two inlets (Ar and CO_2/He). Spectra were recorded before and immediately after the CO_2 shut-off. The same procedure was carried out under light conditions. Figures 9.11 and 9.12 show the DRIFTS signals in the wavelength range of 800-2200 cm^{-1}. The former shows, in dark and light conditions, the increasing band with the formation of the peaks due to CO_2 adsorption on the catalyst surface. Conversely, Figure 9.12 corresponds to the adsorption peaks after the carbon dioxide cut-off, which underlie the decreasing trend with time of the DRIFTS bands, and is the one of greatest interest for the mechanistic study.

The region 1950-2200 cm^{-1} is the region of the C-O stretch of CO adsorbed on the catalyst, where can be found the peaks relative to gas phase and linear carbon monoxide. Indeed it is clearly visible the characteristic band path with the two peaks at $\sim$ 2174 and 2115 cm^{-1}. The 1300-1650 cm^{-1} region is characteristic of C-O vibrations in the bidentate and unidentate carbonate and formate species [77]. The main infrared peaks are in this region, at 1594 and 1372 cm^{-1} (HCOO*). Under light conditions another peak is clearly visible at 1507 cm^{-1} (bidentate CO_3*). Another carbonate peak is present at 815 cm^{-1}. The catalyst surface also appears to be covered by methoxy species (peak at $\sim$ 1075 cm^{-1}). Table 9.1 summarizes the assignments mentioned above with reference to infrared data. The main differences between dark and light conditions concern the magnitude of the adsorption peaks and the disappearance of some specific peaks after CO_2 cut-off. Indeed, after CO_2 evacuation, all the adsorption peaks disappear, with the sole exception of the two HCOO* peaks at 1594 and 1372 cm^{-1}, proving that the formates are stable intermediates. Conversely, under light irradiation, the formate peak at *ca.* 1376 cm^{-1} also disappears, with more formate apparently converted to carbon monoxide and removed from the surface (Figure 9.12). In addition, the height of the two formate peaks at $\sim$ 1594 and 1372 cm^{-1} decreases from dark to light conditions by about 30% and 40% respectively. This is accompanied by an increase in the height of the CO peak of about 65% (Figure 9.12), confirming the photo-enhancement of CO production noted after the activity tests.

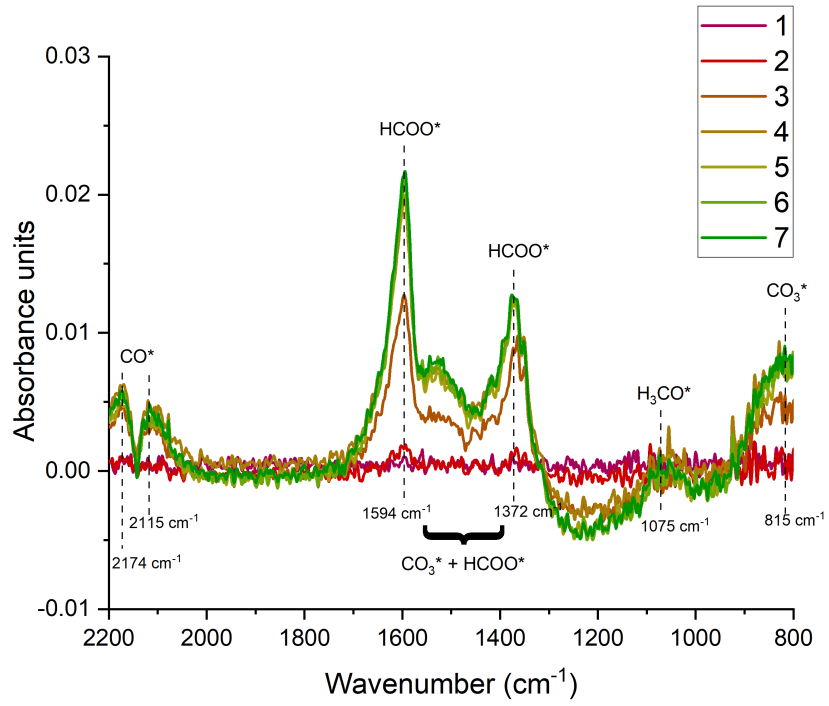

(a)

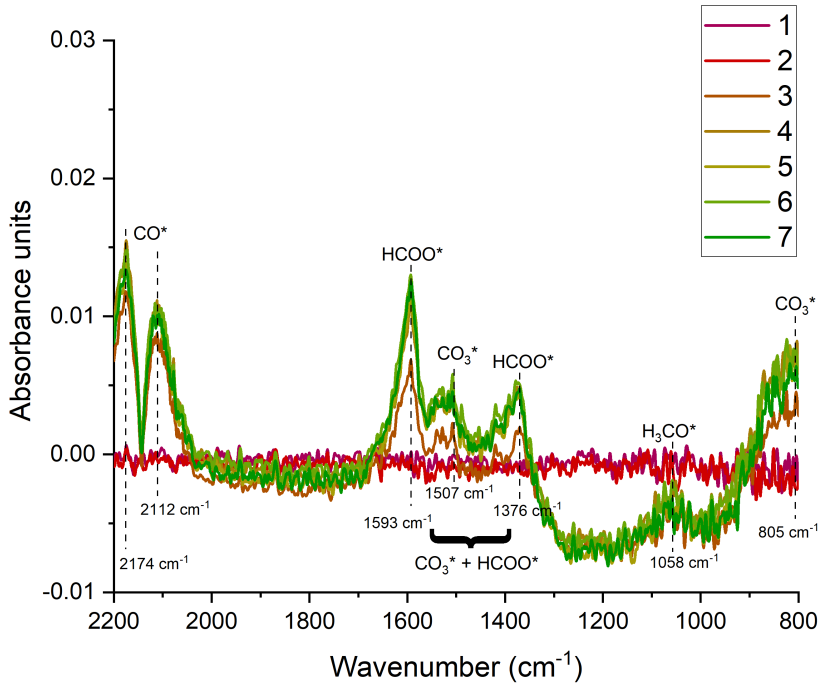

(b)

Figure 9.11. DRIFTS spectra taken over a $Cu/ZnO/Al_2O_3$ before CO_2 cut-off in dark (a) and under light illumination (b). Experimental conditions: p=1 bar, T=230°C, H2/CO2/He=1:1:1, total flowrate = 30 mL/min, catalyst amount = 22 mg.

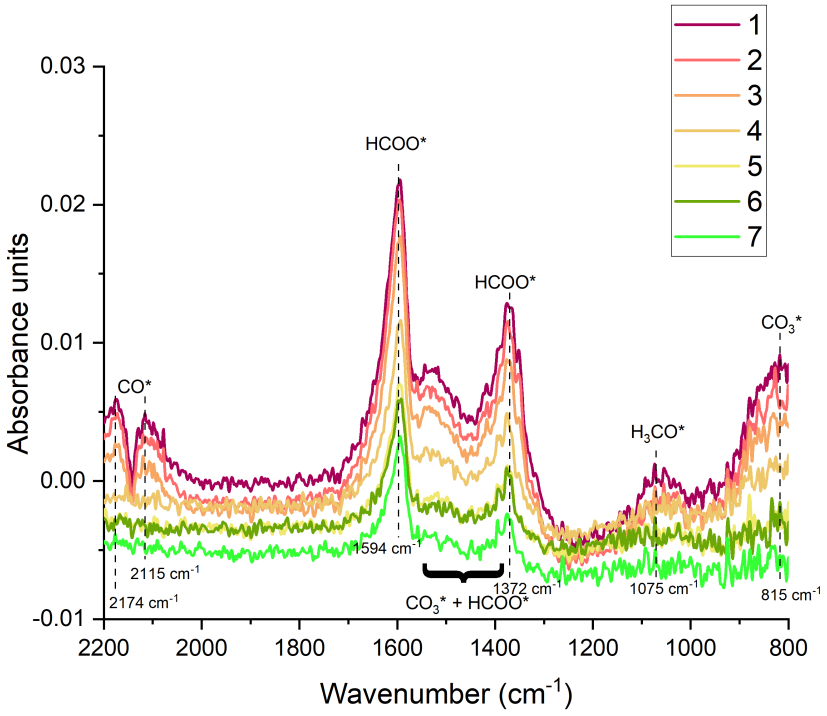

(a)

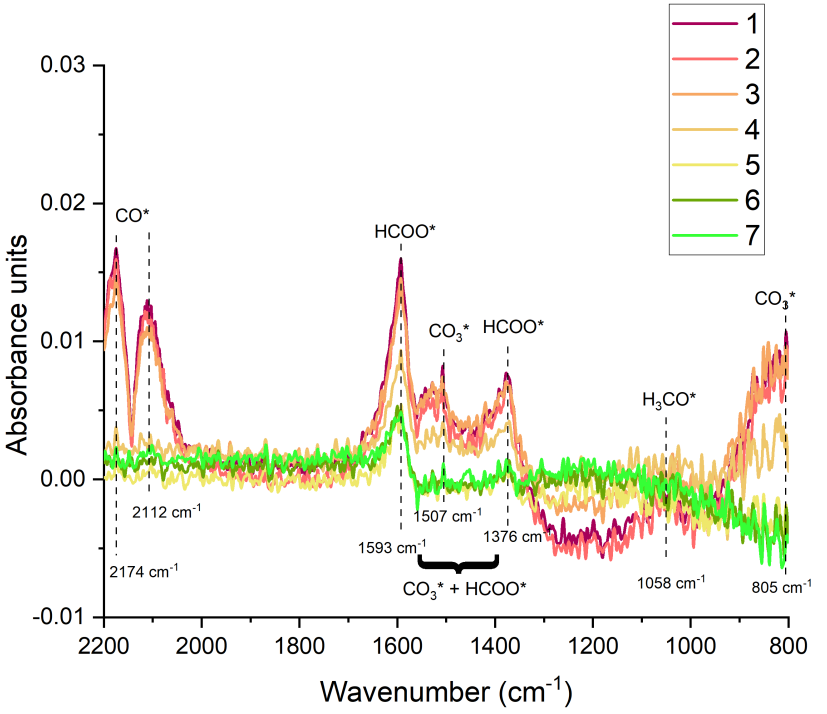

(b)

Figure 9.12. DRIFTS spectra taken over a $Cu/ZnO/Al_2O_3$ after CO_2 cut-off in dark (a) and under light illumination (b). Experimental conditions: p=1 bar, T=230°C, H2/Ar=1:2, total flowrate = 30 mL/min, catalyst amount = 22 mg. Time after CO2 cut off: 1= 0; 2= 105s; 3= 157s; 4= 383s; 5= 1044s; 6= 1636s; 7= 2663s.

Wavenumber (cm^{-1})	Adsorbed species	Reference
2174	CO	[1],[78],[77],[79]
2115	CO	[1],[78],[77],[79]
1594	HCOO* formate	[1],[77],[79]
1507	CO_3* carbonate	[1],[78]
1372	HCOO* formate	[1],[77]
1075	H_3CO* methoxy	[77],[79]
815	CO_3* carbonate	[80]

Table 9.1. Assigned surface species of observed wavenumbers on CZA catalyst

The DRIFTS data were used to plot the normalized band intensity for each species and compare the rate of their decay. This was done to demonstrate the extent to which the rates change from the spectroscopic analysis and how much all the decays are accelerated upon visible light irradiation. Figure 9.13 shows the normalized intensity curves of the CO peaks. These data have been used to calculate the decay rate in dark and light conditions of 0.018 and 0.047 min^{-1} respectively, resulting in a light enhancement of 61%. This emphasizes as the addition of visible light to the RWGS catalytic reaction accelerates CO removal from the catalyst, as well as increasing the production rate as observed by GC during activity tests.

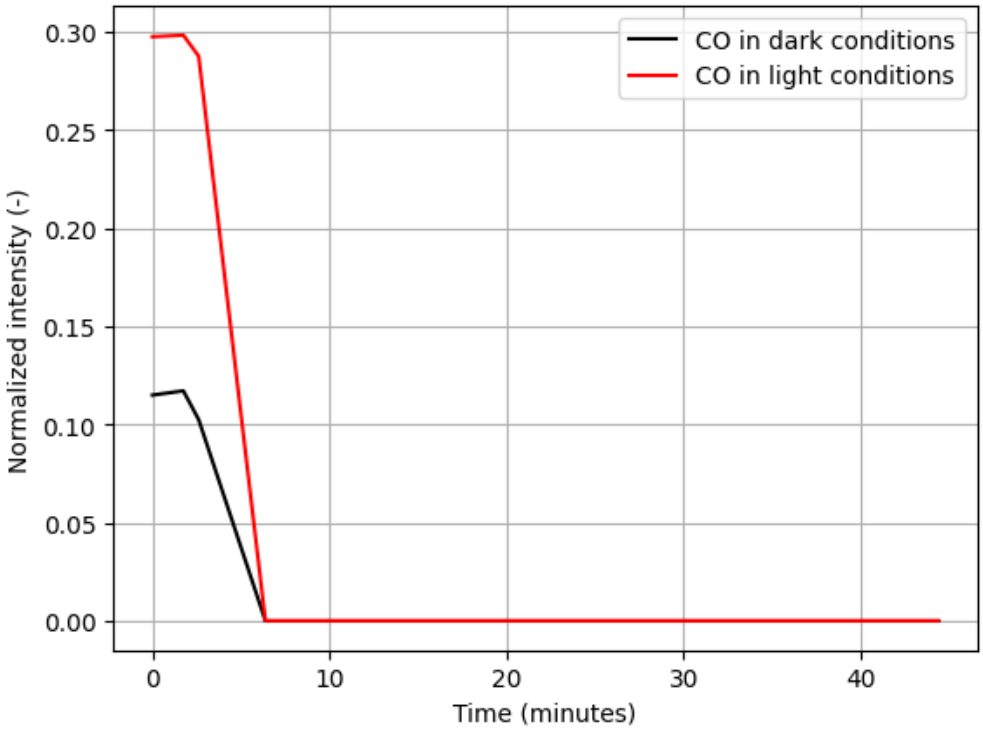

Figure 9.13. Normalized intensity of the CO peaks (at 2174 and 2112 cm^{-1}) plotted against time, to show the enhancement of the CO removal rate upon light irradiation.

10 Conclusions

In this thesis, the CO_2 hydrogenation to CO on the commercial catalyst Cu-ZnO-Al_2O_3 under visible light irradiation has been studied. The catalyst was chemically and physically characterized by XRD, SEM, N_2 physisorption and in situ UV-vis spectroscopy. The main objective was to study the improved performance and mechanism of photo-thermal catalysis. The preliminary tests were designed and carried out by varying several reaction conditions: temperature, flow rate and concentrations of the reactants, power and wavelength of the irradiated light. This was attempted in order to determine the optimum working conditions and how the different reaction conditions influenced the CO rate enhancement. Each activity test showed an increase in the CO production rate with light irradiation, with the highest light enhancement factor of 2.8 measured at T=230°C and H_2/CO_2=1. In situ DRIFTS results have confirmed how visible light leads to higher reactivity of all surface species, with increased production of gaseous CO. Subsequent tests have attempted to gain insight into the reaction mechanism of the RWGS reaction over the CZA catalyst, and if and how it is modified by light irradiation. The first main result in this sense was shown by the desorption tests, which allowed to exclude the redox mechanism as an option for the RWGS reaction mechanism. The obtained results of the rate enhancement, the decrease of the activation energy, the linear dependence of the CO rate on the light power and the different CO rate measured by varying the light wavelength suggested a reaction mechanism mediated by hot electron transfer. After being generated by the Cu LSPR effect, or possibly transferred from excited ZnO, hot carriers transiently occupy the antibonding orbitals of the CO_2 molecules, promoting their activation and subsequent bond cleavage and further reactions. Furthermore, these tests highlighted the fundamental role of blue photons, which are the most efficient in enhancing the CO rate, leading to the highest apparent quantum yield. The other evidence for the change in the reaction mechanism is based on the kinetic analysis, which showed an increase in the concentration of surface H* species, probably due to the Cu LSPR effect, which is effective in promoting the cleavage of the H-H bond. In conclusion, the photo-thermal catalytic reduction of CO_2 over CZA catalyst, has been identified as an interesting and promising technology, both in the field of environmental protection and energy recovery, through the reduction of carbon dioxide emissions, the efficient use of solar light as a renewable energy, allowing to operate at lower temperatures and to obtain higher performances, and the production of industrially relevant products. Despite the performances presented above, there is still ample room for improving catalytic efficiency in the field of photo-thermal catalysis. For photo-thermal catalysis to truly become a reliable source of solar fuels and chemicals, it must overcome several limitations [8],[44],[81],[82]:

- Although photo-thermal catalysis does not demand huge scaling considerations due to its tight linkage to traditional heterogeneous catalytic systems, its main challenge is the incorporation of light into the processes. In fact, unlike other technologies, the photo-thermal approach does not require extremely high temperatures but rather adequate photoreactors capable of harvesting and utilizing sunlight. Therefore, research and development in reactor design and configuration is required for widespread scale-up of this technology.
- Only a few works on photo-thermal catalysis have clarified the dominant pathway that governs the reaction mechanism. Further fundamental investigations in this direction are needed.
- To understand the crucial structure-property relationships, it is necessary to perform in situ spectroscopic studies of photo-thermal catalysts in action. In addition to the methods used in this work, achieving this has to be done through techniques such as X-ray absorption spectroscopy (XAS), X-ray photoelectron spectroscopy (XPS), and transient absorption spectroscopy.
- Feasible and stable photocatalysts are required for an adequate scale-up to commercial plants. However, there are still significant questions regarding the long-term stability of photo-thermal catalysts, particularly with regards to deactivation caused by water and photo-corrosion.

  In particular, the former is highly dangerous against the CZA catalyst and the latter can lead to detrimental oxidation or reduction of the semiconductor or active metal sites.

  Nowadays the investigation of the long-term stability of photocatalysts is inadequate, as most stability tests are limited to short time periods, typically less than 24 hours. Long-term photo-thermal experimentation is necessary to monitor catalyst performance over tens or hundreds of hours and to compare

deactivation rates in the dark and under illumination. In addition, repeated transient dark-light-dark operation, which mimics fluctuating solar radiation, introduces additional instability into the reaction conditions. This phenomenon can also cause a deterioration in catalytic activity. Furthermore, stability tests should be performed in conjunction with structural and chemical characterization. Indeed, the correlation between the decrease in activity and structural changes will allow the re-engineering and design of more stable and robust photocatalysts, not just (initially) highly active ones.

- Although this work mainly focuses on the catalytic performances and alteration of reaction mechanisms upon light irradiation, to truly achieve renewable CO production via photo-thermal CO_2 hydrogenation, further research relating to carbon capture technologies and renewable hydrogen generation technologies is necessary.
- Finally, it is necessary to assess the feasibility of scaling up from laboratory to pilot to industrial scale, taking into account space requirements, consistency of solar irradiation, techno-economic analysis, heat management, and energy efficiency.

Nomenclature

AQY	Apparent quantum yield
BET	Brunauer-Emmett-Teller
BJH	Barrett-Joyner-Halenda
CB	Conduction band
CCS	CO_2 capture and sequestration
CI	Chemical ionization
CID	Chemical interface damping
CNTs	Carbon nanotubes
CZA	$Cu/ZnO/Al_2O_3$
DME	Dimethyl ether
DRS	Diffuse Reflectance Spectroscopy
EI	Electron ionization
FT	Fischer-Tropsch
FT-IR	Fourier transform infrared
FWHM	Full Width at Half Maximum
GHG	Greenhouse gas
HM	High Economic Growth
HOMO	Highest occupied molecular orbital
HP	High Oil Price
HZ	High Zero-Carbon Technology Cost
ICDS	Inorganic Crystal Structure Database
LCA	Life cycle assessment
LM	Low Economic Growth
LP	Low Oil Price
LSPR	Localized surface plasmon reasonance
LUMO	Lowest unoccupied molecular orbital
LZ	Low Zero-Carbon Technology Cost
MS	Mass spectrometry
NHE	Normal hydrogen electrode
NIR	Near infrared region
NPs	Nanoparticles
PEM	Proton exchange membrane
PFR	Plug flow reactor
PMET	Plasmon-mediated electron transfer
PTR	Proton-transfer reaction
PV	Photovoltaic
QDs	Quantum dots
QMA	Quadrupole mass analyzers
QY	Quantum yield
RE	Renewable energy
RWGS	Reverse water gas shift
SB	Schottky barrier
SEM	Secondary electron emission
SMSI	Strong metal-support interaction
TOF	Time-of-flight
UHV	Ultra high vacuum
UV-vis	Ultraviolet-visible
VB	Valence band
WGS	Water gas shift
XAS	X-ray absorption spectroscopy
XPS	X-ray photoelectron spectroscopy
XRD	X-ray diffraction spectroscopy

Sitography

[S1] https://www.scimed.co.uk/education/sem-scanning-electron-microscopy/

References

[1] Bingqiao Xie, Roong Jien Wong, Tze Hao Tan, Michael Higham, Emma K Gibson, Donato Decarolis, June Callison, Kondo-Francois Aguey-Zinsou, Michael Bowker, C Richard A Catlow, et al. Synergistic ultraviolet and visible light photo-activation enables intensified low-temperature methanol synthesis over copper/zinc oxide/alumina. *Nature Communications*, 11(1):1615, 2020.

[2] Aniruddha A Upadhye, Insoo Ro, Xu Zeng, Hyung Ju Kim, Isabel Tejedor, Marc A Anderson, James A Dumesic, and George W Huber. Plasmon-enhanced reverse water gas shift reaction over oxide supported au catalysts. *Catalysis Science & Technology*, 5(5):2590–2601, 2015.

[3] International energy outlook 2023 (ieo2023). *US Energy Information Administration (EIA): Washington, DC, USA*, 2023:1–70, 2023.

[4] Antonio J Martín, Gastón O Larrazábal, and Javier Pérez-Ramírez. Towards sustainable fuels and chemicals through the electrochemical reduction of co 2: lessons from water electrolysis. *Green Chemistry*, 17(12):5114–5130, 2015.

[5] Gerhard Ertl. Reactions at surfaces: from atoms to complexity (nobel lecture). *Angewandte Chemie International Edition*, 47(19):3524–3535, 2008.

[6] Zhou-jun Wang, Hui Song, Huimin Liu, and Jinhua Ye. Coupling of solar energy and thermal energy for carbon dioxide reduction: status and prospects. *Angewandte Chemie International Edition*, 59(21):8016–8035, 2020.

[7] Severin N Habisreutinger, Lukas Schmidt-Mende, and Jacek K Stolarczyk. Photocatalytic reduction of co2 on tio2 and other semiconductors. *Angewandte Chemie International Edition*, 52(29):7372–7408, 2013.

[8] Diego Mateo, Jose Luis Cerrillo, Sara Durini, and Jorge Gascon. Fundamentals and applications of photo-thermal catalysis. *Chemical Society Reviews*, 50(3):2173–2210, 2021.

[9] Philipp Kaiser, Rajabhau Bajirao Unde, Christoph Kern, and Andreas Jess. Production of liquid hydrocarbons with co2 as carbon source based on reverse water-gas shift and fischer-tropsch synthesis. *Chemie Ingenieur Technik*, 85(4):489–499, 2013.

[10] Shin-Ichiro Fujita, Masahito Usui, and Nobutsune Takezawa. Mechanism of the reverse water gas shift reaction over cu/zno catalyst. *Journal of Catalysis*, 134(1):220–225, 1992.

[11] Hayat Khan, Aditya S Yerramilli, Adrien D'Oliveira, Terry L Alford, Daria C Boffito, and Gregory S Patience. Experimental methods in chemical engineering: X-ray diffraction spectroscopy—xrd. *The Canadian journal of chemical engineering*, 98(6):1255–1266, 2020.

[12] J Epp. X-ray diffraction (xrd) techniques for materials characterization. In *Materials characterization using nondestructive evaluation (NDE) methods*, pages 81–124. Elsevier, 2016.

[13] SA Hassanzadeh-Tabrizi. Precise calculation of crystallite size of nanomaterials: a review. *Journal of Alloys and Compounds*, page 171914, 2023.

[14] Raoof Bardestani, Gregory S Patience, and Serge Kaliaguine. Experimental methods in chemical engineering: specific surface area and pore size distribution measurements—bet, bjh, and dft. *The Canadian Journal of Chemical Engineering*, 97(11):2781–2791, 2019.

[15] Matthias Thommes, Katsumi Kaneko, Alexander V Neimark, James P Olivier, Francisco Rodriguez-Reinoso, Jean Rouquerol, and Kenneth SW Sing. Physisorption of gases, with special reference to the evaluation of surface area and pore size distribution (iupac technical report). *Pure and applied chemistry*, 87(9-10):1051–1069, 2015.

[16] Thomas E Davies, He Li, Stéphanie Bessette, Raynald Gauvin, Gregory S Patience, and Nicholas F Dummer. Experimental methods in chemical engineering: Scanning electron microscopy and x-ray ultra-microscopy—sem and xum. *The Canadian Journal of Chemical Engineering*, 100(11):3145–3159, 2022.

[17] Sarina Sarina, Esa Jaatinen, Qi Xiao, Yi Ming Huang, Philip Christopher, Jin Cai Zhao, and Huai Yong Zhu. Photon energy threshold in direct photocatalysis with metal nanoparticles: key evidence from the action spectrum of the reaction. *The Journal of Physical Chemistry Letters*, 8(11):2526–2534, 2017.

[18] Curtis D Mowry, Russell L Jarek, Jessica Kustas, Amber Celeste Telles, and Adam S Pimentel. Gas analysis by mass spectrometry. Technical report, Sandia National Lab.(SNL-NM), Albuquerque, NM (United States), 2020.

[19] Patrice Perreault, Etienne Robert, and Gregory S Patience. Experimental methods in chemical engineering: Mass spectrometry—ms. *The Canadian Journal of Chemical Engineering*, 97(5):1036–1042, 2019.

[20] Bernadette Philips-Invernizzi, Daniel Dupont, and Claude Caze. Bibliographical review for reflectance of diffusing media. *Optical Engineering*, 40(6):1082–1092, 2001.

[21] Nengwen Wang, Yuhua Yang, and Guowei Yang. Great blue-shift of luminescence of zno nanoparticle array constructed from zno quantum dots. *Nanoscale research letters*, 6:1–6, 2011.

[22] Juan J Bravo-Suárez and Priya D Srinivasan. Design characteristics of in situ and operando ultraviolet-visible and vibrational spectroscopic reaction cells for heterogeneous catalysis. *Catalysis Reviews*, 59(4):295–445, 2017.

[23] George A Olah. Beyond oil and gas: the methanol economy. *Angewandte Chemie International Edition*, 44(18):2636–2639, 2005.

[24] Maochang Liu, Guijun Chen, Boya Min, Jinwen Shi, Yubin Chen, and Qibin Liu. Photocatalytic co2 reduction. *Solar-to-Chemical Conversion: Photocatalytic and Photoelectrochemcial Processes*, pages 243–267, 2021.

[25] Akira Fujishima and Kenichi Honda. Electrochemical photolysis of water at a semiconductor electrode. *nature*, 238(5358):37–38, 1972.

[26] M Halmann. Photoelectrochemical reduction of aqueous carbon dioxide on p-type gallium phosphide in liquid junction solar cells. *Nature*, 275(5676):115–116, 1978.

[27] Tooru Inoue, Akira Fujishima, Satoshi Konishi, and Kenichi Honda. Photoelectrocatalytic reduction of carbon dioxide in aqueous suspensions of semiconductor powders. *Nature*, 277(5698):637–638, 1979.

[28] B Aurian-Blajeni, M Halmann, and Joost Manassen. Photoreduction of carbon dioxide and water into formaldehyde and methanol on semiconductor materials. *Solar Energy*, 25(2):165–170, 1980.

[29] SM Aliwi and KoF Al-Jubori. Photoreduction of co2 by metal sulphide semiconductors in presence of h2s. *Solar energy materials*, 18(3-4):223–229, 1989.

[30] Hiroshi Inoue, Tsukasa Torimoto, Takao Sakata, Hirotaro Mori, and Hiroshi Yoneyama. Effects of size quantization of zinc sulfide microcrystallites on photocatalytic reduction of carbon dioxide. *Chemistry letters*, (9):1483–1486, 1990.

[31] M Sakurai, M Terada, and T Sugimura. Reports from users of the jcrb cell bank.(1986-2005). *Proc. Natl. Acad. Sci. USA*, 84:444–448, 1987.

[32] Wan-Chen Huang, Lian-Ming Lyu, Yu-Chen Yang, and Michael H Huang. Synthesis of cu2o nanocrystals from cubic to rhombic dodecahedral structures and their comparative photocatalytic activity. *Journal of the American Chemical Society*, 134(2):1261–1267, 2012.

[33] Guillaume Baffou, Ivan Bordacchini, Andrea Baldi, and Romain Quidant. Simple experimental procedures to distinguish photothermal from hot-carrier processes in plasmonics. *Light: Science & Applications*, 9(1):108, 2020.

[34] Shaunak Mukherjee, Florian Libisch, Nicolas Large, Oara Neumann, Lisa V Brown, Jin Cheng, J Britt Lassiter, Emily A Carter, Peter Nordlander, and Naomi J Halas. Hot electrons do the impossible: plasmon-induced dissociation of h2 on au. *Nano letters*, 13(1):240–247, 2013.

[35] Phillip Christopher, Hongliang Xin, and Suljo Linic. Visible-light-enhanced catalytic oxidation reactions on plasmonic silver nanostructures. *Nature chemistry*, 3(6):467–472, 2011.

[36] Calvin Boerigter, Robert Campana, Matthew Morabito, and Suljo Linic. Evidence and implications of direct charge excitation as the dominant mechanism in plasmon-mediated photocatalysis. *Nature communications*, 7(1):10545, 2016.

[37] Calvin Boerigter, Umar Aslam, and Suljo Linic. Mechanism of charge transfer from plasmonic nanostructures to chemically attached materials. *ACS nano*, 10(6):6108–6115, 2016.

[38] Akihiro Furube, Luchao Du, Kohjiro Hara, Ryuzi Katoh, and Masanori Tachiya. Ultrafast plasmon-induced electron transfer from gold nanodots into tio2 nanoparticles. *Journal of the American Chemical Society*, 129(48):14852–14853, 2007.

[39] Thomas P White and Kylie R Catchpole. Plasmon-enhanced internal photoemission for photovoltaics: theoretical efficiency limits. *Applied Physics Letters*, 101(7), 2012.

[40] Horst Kisch. Semiconductor photocatalysis for atom-economic reactions. *Environmental Photochemistry Part III*, pages 181–220, 2015.

[41] Alexander O Govorov, Wei Zhang, Timur Skeini, Hugh Richardson, Jaebeom Lee, and Nicholas A Kotov. Gold nanoparticle ensembles as heaters and actuators: melting and collective plasmon resonances. *Nanoscale Research Letters*, 1:84–90, 2006.

[42] Shaunak Mukherjee, Linan Zhou, Amanda M Goodman, Nicolas Large, Ciceron Ayala-Orozco, Yu Zhang, Peter Nordlander, and Naomi J Halas. Hot-electron-induced dissociation of h2 on gold nanoparticles supported on sio2. *Journal of the American Chemical Society*, 136(1):64–67, 2014.

[43] Linan Zhou, Dayne F Swearer, Chao Zhang, Hossein Robatjazi, Hangqi Zhao, Luke Henderson, Liangliang Dong, Phillip Christopher, Emily A Carter, Peter Nordlander, et al. Quantifying hot carrier and thermal contributions in plasmonic photocatalysis. *Science*, 362(6410):69–72, 2018.

[44] Yufei Zhao, Wa Gao, Siwei Li, Gareth R Williams, Abdul Hanif Mahadi, and Ding Ma. Solar-versus thermal-driven catalysis for energy conversion. *Joule*, 3(4):920–937, 2019.

[45] Janos Rasko and Frigyes Solymosi. Infrared spectroscopic study of the photoinduced activation of co2 on tio2 and rh/tio2 catalysts. *The Journal of Physical Chemistry*, 98(29):7147–7152, 1994.

[46] Yolanda A Daza and John N Kuhn. Co 2 conversion by reverse water gas shift catalysis: comparison of catalysts, mechanisms and their consequences for co 2 conversion to liquid fuels. *RSC advances*, 6(55):49675–49691, 2016.

[47] L Pastor-Pérez, F Baibars, E Le Sache, Harvey Arellano-Garcia, Sai Gu, and T Ramirez Reina. Co2 valorisation via reverse water-gas shift reaction using advanced cs doped fe-cu/al2o3 catalysts. *Journal of CO2 utilization*, 21:423–428, 2017.

[48] Dharik S Mallapragada, Navneet R Singh, Vlad Curteanu, and Rakesh Agrawal. Sun-to-fuel assessment of routes for fixing co2 as liquid fuel. *Industrial & Engineering Chemistry Research*, 52(14):5136–5144, 2013.

[49] Rufino M Navarro, M Cruz Sanchez-Sanchez, M Consuelo Alvarez-Galvan, Jose Luis G Fierro, and Saeed M Al-Zaharani. Hydrogen production from renewables. *Encyclopedia of Inorganic Chemistry*, 2006.

[50] Gabriele Centi, Elsje Alessandra Quadrelli, and Siglinda Perathoner. Catalysis for co 2 conversion: a key technology for rapid introduction of renewable energy in the value chain of chemical industries. *Energy & Environmental Science*, 6(6):1711–1731, 2013.

[51] Norlida Kamarulzaman, Muhd Firdaus Kasim, and Roshidah Rusdi. Band gap narrowing and widening of zno nanostructures and doped materials. *Nanoscale research letters*, 10:1–12, 2015.

[52] Masahiro Saito and Kazuhisa Murata. Development of high performance cu/zno-based catalysts for methanol synthesis and the water-gas shift reaction. *Catalysis Surveys from Asia*, 8:285–294, 2004.

[53] Shyam Kattel, Pedro J Ramírez, Jingguang G Chen, José A Rodriguez, and Ping Liu. Active sites for co2 hydrogenation to methanol on cu/zno catalysts. *Science*, 355(6331):1296–1299, 2017.

[54] Wei Xiong, Zongfang Wu, Xuanye Chen, Jieqiong Ding, Aiai Ye, Wenhua Zhang, and Weixin Huang. Active copper structures in zno–cu interfacial catalysis: Co2 hydrogenation to methanol and reverse water–gas shift reactions. *Science China Chemistry*, pages 1–9, 2023.

[55] Felix Studt, Malte Behrens, Edward L Kunkes, Nygil Thomas, Stefan Zander, Andrey Tarasov, Julia Schumann, Elias Frei, Joel B Varley, Frank Abild-Pedersen, et al. The mechanism of co and co2 hydrogenation to methanol over cu-based catalysts. *ChemCatChem*, 7(7):1105–1111, 2015.

[56] Karl-Heinz Ernst, Charles T Campbell, and Giuliano Moretti. Kinetics of the reverse water-gas shift reaction over cu (110). *Journal of Catalysis*, 134(1):66–74, 1992.

[57] J Nakamura, JA Rodriguez, and CT Campbell. Does co2 dissociatively adsorb on cu surfaces? *Journal of Physics: Condensed Matter*, 1(SB):SB149, 1989.

[58] Ching-Shiun Chen, Wu-Hsun Cheng, and Shou-Shiun Lin. Mechanism of co formation in reverse water–gas shift reaction over cu/al 2 o 3 catalyst. *Catalysis letters*, 68:45–48, 2000.

[59] AW Hull. A new method of chemical analysis. *Journal of the American Chemical Society*, 41(8):1168–1175, 1919.

[60] Andrei A Bunaciu, Elena Gabriela UdriŞTioiu, and Hassan Y Aboul-Enein. X-ray diffraction: instrumentation and applications. *Critical reviews in analytical chemistry*, 45(4):289–299, 2015.

[61] Howard Eugene Swanson. *Standard X-ray diffraction powder patterns*, volume 25. US Department of Commerce, National Bureau of Standards, 1953.

[62] Seon-Yong Ahn, Kyoung-Jin Kim, Beom-Jun Kim, Jae-Oh Shim, Won-Jun Jang, and Hyun-Seog Roh. Unravelling the active sites and structure-activity relationship on cu–zno–al2o3 based catalysts for water-gas shift reaction. *Applied Catalysis B: Environmental*, 325:122320, 2023.

[63] M Albert Vannice and William H Joyce. *Kinetics of catalytic reactions*, volume 134. Springer, 2005.

[64] Frank S Stone and David Waller. Cu–zno and cu–zno/al 2 o 3 catalysts for the reverse water-gas shift reaction. the effect of the cu/zn ratio on precursor characteristics and on the activity of the derived catalysts. *Topics in catalysis*, 22:305–318, 2003.

[65] Stephen Brunauer, Paul Hugh Emmett, and Edward Teller. Adsorption of gases in multimolecular layers. *Journal of the American chemical society*, 60(2):309–319, 1938.

[66] EP Barrett, LG Joyner, and PP Halenda. Study of pore size distribution by capillary absorption method. *J. Am. Chem. Soc*, 73:373–380, 1951.

[67] Kenneth SW Sing. Reporting physisorption data for gas/solid systems with special reference to the determination of surface area and porosity (provisional). *Pure and applied chemistry*, 54(11):2201–2218, 1982.

[68] Hashim A Alzahrani and Juan J Bravo-Suárez. In situ raman spectroscopy study of silver particle size effects on unpromoted ag/α-al2o3 during ethylene epoxidation with molecular oxygen. *Journal of Catalysis*, 418:225–236, 2023.

[69] Charles T Campbell and Karl-Heinz Ernst. Forward and reverse water—gas shift reactions on model copper catalysts: Kinetics and elementary steps. ACS Publications, 1992.

[70] MJL Ginés, AJ Marchi, and CR Apesteguía. Kinetic study of the reverse water-gas shift reaction over cuo/zno/al2o3 catalysts. *Applied Catalysis A: General*, 154(1-2):155–171, 1997.

[71] Kristijan Lorber, Janez Zavasnik, Iztok Arčon, Matej Huš, Janvit Terzan, Blaž Likozar, and Petar Djĭnović. Co2 activation over nanoshaped ceo2 decorated with nickel for low-temperature methane dry reforming. *ACS Applied Materials & Interfaces*, 14(28):31862–31878, 2022.

[72] Pietro Morozzi, Barbara Ballarin, Sara Arcozzi, Erika Brattich, Franco Lucarelli, Silvia Nava, Pedro José Gómez-Cascales, JAG Orza, and Laura Tositti. Ultraviolet–visible diffuse reflectance spectroscopy (uv–vis drs), a rapid and non-destructive analytical tool for the identification of saharan dust events in particulate matter filters. *Atmospheric Environment*, 252:118297, 2021.

[73] Patrycja Makuła, Michał Pacia, and Wojciech Macyk. How to correctly determine the band gap energy of modified semiconductor photocatalysts based on uv–vis spectra, 2018.

[74] Ishaq Musa and Naser QAMHIEH. Study of optical energy gap and quantum confinment effects in zinc oxide nanoparticles and nanorods. 2019.

[75] Barbara Stuart. Infrared spectroscopy. *Kirk-Othmer encyclopedia of chemical technology*, 2000.

[76] Ralph Levinson. *More modern chemical techniques*. Royal Society of Chemistry, 2001.

[77] S Bailey, GF Froment, Joost-Willem Snoeck, and KC Waugh. A drifts study of the morphology and surface adsorbate composition of an operating methanol synthesis catalyst. *Catalysis letters*, 30:99–111, 1994.

[78] Sonja Kouva, Jenni Andersin, Karoliina Honkala, Juha Lehtonen, Leon Lefferts, and Jaana Kanervo. Water and carbon oxides on monoclinic zirconia: experimental and computational insights. *Physical chemistry chemical physics*, 16(38):20650–20664, 2014.

[79] Michael Bowker and KC Waugh. From surface science to catalysis: the importance of methoxy and formate species on cu single crystals and industrial catalysts. *Surface Science*, 650:93–102, 2016.

[80] Georgi N Vayssilov, Mihail Mihaylov, Petko St Petkov, Konstantin I Hadjiivanov, and Konstantin M Neyman. Reassignment of the vibrational spectra of carbonates, formates, and related surface species on ceria: a combined density functional and infrared spectroscopy investigation. *The Journal of Physical Chemistry C*, 115(47):23435–23454, 2011.

[81] Michael Ng, Vedran Jovic, Geoffrey IN Waterhouse, and John Kennedy. Recent progress in photothermal catalyst design for methanol production. *Emergent Materials*, 6(4):1097–1115, 2023.

[82] Kristijan Lorber and Petar Djinović. Accelerating photo-thermal co2 reduction to co, ch4 or methanol over metal/oxide semiconductor catalysts. *Iscience*, 25(4), 2022.